MEASUREMENT OF OPTICAL EIGENMODES OF NANOSTRUCTURES WITH RELATIVISTIC ELECTRONS

A Dissertation

Presented to the Faculty of the Graduate School

of Cornell University

in Partial Fulfillment of the Requirements for the Degree of

Doctor of Philosophy

by

Jerome Kartham Hyun

May 2009

MEASUREMENT OF OPTICAL EIGENMODES OF NANOSTRUCTURES WITH RELATIVISTIC ELECTRONS

Jerome Kartham Hyun, Ph.D.

Cornell University 2009

While structures continue to shrink in size for novel optoelectronic applications, the ability to study new optical phenomenon on the nanoscale becomes important. Efforts in this area face challenges as conventional optical techniques fail to achieve the necessary spatial resolution due to fundamental diffraction limitations. A unique and powerful solution for performing near-field optical spectroscopy with nanometer spatial resolution using relativistic electrons in a scanning transmission electron microscope (STEM) and electron energy loss spectroscopy (EELS) environment is presented. Relativistic electrons can be focused down to nanometer-sized probes, and can behave as a virtual, broad-band source of light. By taking advantage of these properties, the photonic density of states of far-ultraviolet whispering gallery modes in SiO_2 nanospheres are excited by passing an electron beam close to the sphere. In a similar manner, the waveguide modes of GaN and Ge nanowires are measured, where the nanowire is oriented perpendicular to the electron optical axis. For the Ge nanowires, a multi-mode and zero-mode system is probed. A dielectric formalism describing the energy loss of the electron due to the nanowire is developed in a relativistic framework, and shows quantitative agreement with experimental results. Calculations of nanowire shell systems consisting of a dielectric core and metallic shell are also presented, where the interaction between the surface plasmonic modes and the dielectric waveguide modes are observed. The results open

promising gateways for spatially-resolved optical observations of more complex nanostructures.

BIOGRAPHICAL SKETCH

Jerome K. Hyun was born on June 15, 1980 in Huntsville, Alabama. Half of his childhood was spent in the friendly town of Potsdam, NY, and the other half in the busy city of Seoul, Korea. For high school, he attended a private boarding school in the quiet town of Lakeville, CT. He then entered Columbia University in New York City in the fall of 1998. After receiving his B.S. in Applied Physics in the spring of 2002, he transitioned into the small town of Ithaca, NY, and pursued his interests in Physics at Cornell University. For the first two years, he worked as a teaching assistant. He briefly worked in the research groups of Prof. Carl Franck and Prof. Hasan Padamsee. In the spring of 2004, Jerome entered Prof. David Muller's electron microscopy group, where he received his M.A. in January 2006 and his Ph.D. in the spring of 2009. As a Post-doc, he will continue his scientific interests in Prof. Lincoln Lauhon's group at Northwestern University, and again transition from small town to big city by moving to Chicago.

For my parents, and in the spirit of a 4th generational tradition.

ACKNOWLEDGEMENTS

I would like to thank my advisor David Muller for accepting me into his research group, and providing generous support and guidance throughout my graduate career. I appreciate the time he regularly committed to visit our office despite his busy schedule, and his incredibly insightful discussions which helped broaden my scope of science. His tolerance of my nocturnal schedule has in many ways been a privilege. I am also grateful to him for instilling in me a deep appreciation of scientific integrity.

I also would like to acknowledge the National Science Foundation and Semiconductor Research Corporation and facilities for providing me with the necessary funding. I would also like to thank John Grazul and Mick Thomas for relaying their valuable microscopy and sample fabrication techniques. I also acknowledge Earl Kirkland and Chekesha Liddell for their support.

All members of the Muller group have been terrific colleagues. I thank the first generation of students, Lena Fitting, Peter Ercius, Judy Cha, and Huolin Xin, for their generosity, scientific companionship, and fun memories. I would like to specially thank Aycan Yurtsever for his unofficial early mentorship, and teaching me how to think more like a physicist instead of an engineer. Martin Couillard was responsible for getting me started on the current thesis topic. Matt Weyland taught me STEM tomography. And Andre Mkhoyan helped me with interpretation of EELS. I would also like to thank the new generation of students, Julia Mundy, Pensheng Huang, and Rob Hovden, for their enthusiasm and support. I would also like to acknowledge David Tagatac, Arthur Barnard and Lucas Swanson for their assistance and help in early projects.

I thank my collaborators, Vic Liu, Poorna Rajendran, Hitesh Arora, and Mark Levendorf, and wish them the best in their current projects. I also thank

Jinho Lee, Jinhwan Lee, Heonsang Kim and Moonkyung Kim for their companionship since my arrival to Cornell in 2002.

Finally, I am grateful to my committee members, Sol Gruner and Veit Elser for taking an interest in my research, and committing time for my examinations. I also thank Prof. Piet Brouwer for generously agreeing to proxy. I thank all of them including my advisor and Dr. Lisa Wickham for reading through this thesis. Their comments and corrections have helped to improve the clarity and content of this work.

TABLE OF CONTENTS

LIST OF FIGURES

CHAPTER 1

INTRODUCTION

Nanostructures typically refer to structures much less than a micron in characteristic dimensions. These structures exhibit optical, electrical and mechanical properties that depend on their size, and have invited intense interest from many fields. Simple shapes such as spheres and wires have been agressively integrated into devices that utilize their characteristic dimensionality. In particular, nanospheres have found applications in photonic crystals waveguides [3] for light guiding, and nanocomposite materials for enhanced luminescence [4]. Likewise, nanowires have found applications in a variety of optoelectronic devices such as solar cells [5, 6], sensors [7] and lasers [8, 9]. Discoveries of interesting thermoelectric and piezoelectric properties have also opened nanowires to thermal and mechanical applications. This thesis will focus on the optical properties of nanostructures.

Optical detection of characteristic modes with sufficient spatial resolution is a critical component to improving and engineering nanostructure-integrated optical devices. However, as the dimensions of these simple structures shrink to sizes less than the wavelength of light, the fundamental diffraction limit inhibits the characterization of local optical fields using conventional optical techniques. One popular method to overcome this difficulty is by using Atomic Force Microscopy (AFM) equipped with a nanoscopic optical probe [10]. Here, the probe can scan near the vicinity of the nanostructure and supply optical information. However, this method suffers from a fundamental problem intrinsic to its detection mechanism; it requires the optical probe to be large in size for it to act as an efficient antenna. At the same time, high spatial resolution requires the probe to

be small. The best spatial resolution reported is around 50 nm, but at a significant cost in signal to noise. The method also suffers from parasitic interference and sample-probe coupling effects.

The scanning transmission electron microscope (STEM) equipped with an energy-loss spectrometer offers a unique solution to optical characterization of nanostructures with superior spatial resolution. Unlike optical-probe techniques, the method is clean and suffers no parasitic interference. Using electromagnetic lenses, relativistic electrons can be focused down to atomic-size probes. Additionally, the electron can act like a virtual broad-band source of light. With the two properties combined, STEM stands as a powerful tool for near-field optical characterization of nanostructures.

This thesis explores the technique, providing optical measurements on both spheres and nanowires. In all experiments, an experimental setup involves the fast electron passing near the surface of the target. This non-penetrating electron trajectory is also referred to as an *aloof* trajectory. Chapter 2 discusses measurements of the density of states (DOS) of a whispering gallery mode (WGM) in a SiO_2 nanosphere. Within the bandgap of SiO_2, the existence of far-ultraviolet radiative modes, corresponding to whispering gallery modes, are shown. The energies of the modes are also shown to scale inversely with the dimension of the sphere. Since these results are the first direct measurements of WGMs in a single nanosphere, they hold promise for an array of nanospheres or photonic crystal applications where the photonic band-structure could also be probed using the same technique.

Chapter 3 extends the discussion to measurements of the optical eigenmodes in nanowires. Here, an analytical derivation of the relativistic electron energy

loss probability is provided. GaN and Ge nanowires are investigated independently, showing peaks indicative of transverse whispering gallery modes. An energy-loss map is compared to the optical dispersion of the wire, providing a direct correlation.

Chapter 4 discusses calculations of core-shell nanowire structures. An emphasis is put on investigating an interaction between the surface plasmons and dielectric waveguide modes in a system containing metal and dielectric components. Calculations also show that metal coatings may enhance the guiding of light.

1.1 The Fast Electron as a Virtual Photon

The concept of probing optical states using electrons instead of photons may at first seem mysterious. It can be shown that an electron travelling at relativistic velocities (i.e., v~c) can behave as a virtual photon. To first comprehend this idea, the effect of special relativity on the electric field must be explored.

Unlike mass, distance, or energy, charge is relativistically invariant. In other words, charge stays the same in any inertial frame. If the charge does not change in different inertial frames, the electric field has to change to accommodate the change in length. Purcell demonstrates through the simple usage of charged sheets and Lorentz contraction the relativistic field behavior of charges moving at a constant velocity [11].

One can imagine two square plates of charge with surface density $+\sigma$ and $-\sigma$ separated by a small distance such that the field inside can be considered uniform (Fig. 1.1). One can then consider an inertial frame that moves in a di-

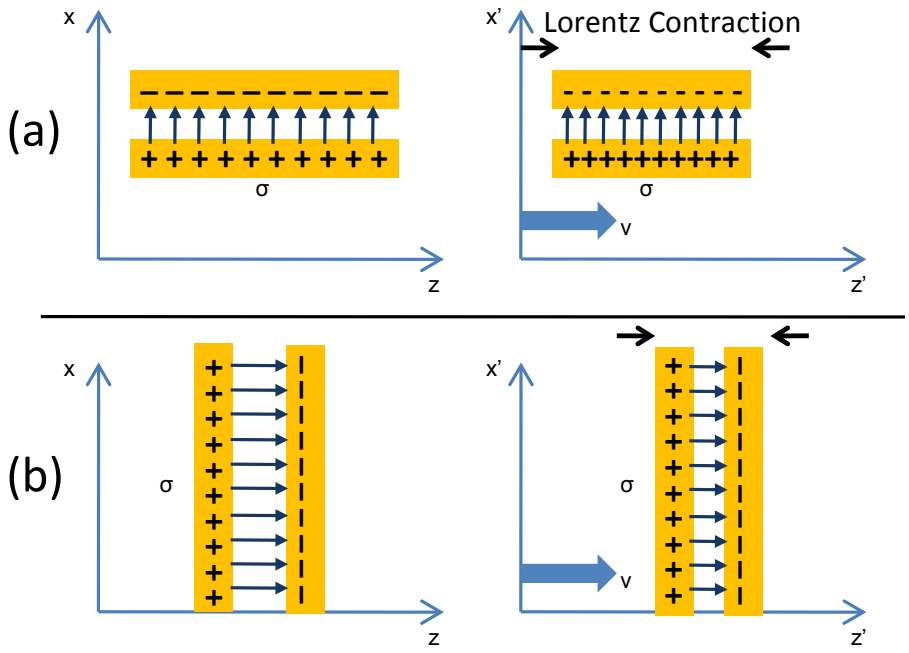

Figure 1.1: (a) For an inertial frame moving parallel to the charged plates, the Lorentz contraction causes an increase in the charge density, and consequently in the electric field by a factor γ. (b)For an inertial frame moving perpendicular to the charged plates, the field strength between the plates is not affected by the Lorentz contraction.

rection parallel to the plates, or perpendicular to the electric field between the plates (Fig. 1.1(a)). In this frame (denoted with ′), the length of the plates will undergo a Lorentz contraction. Since the charge stays the same due to invariance, the shortened set of plates results in a higher charge density by a ratio γ. As the electric field between the two plates in the stationary frame is $4\pi\sigma$, in the moving frame it will be $4\gamma\pi\sigma$. From this one can conclude,

$$E'_{\perp} = \gamma E_{\perp} \tag{1.1}$$

Likewise, one can imagine two square plates of charge set up perpendicular to the velocity of the moving frame (Fig. 1.1(b)). This also means the electric field between the plates are parallel to the velocity. Since the plates are consid-

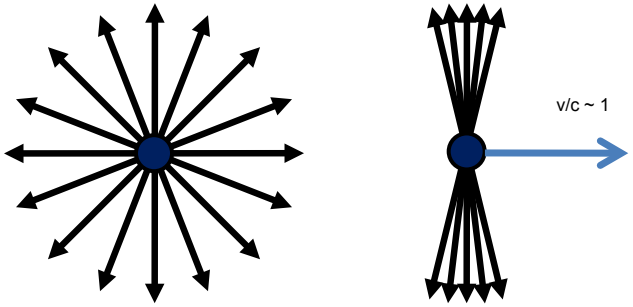

Figure 1.2: The field lines of a stationary charged particle (left). The field lines of a charged particle moving at a relativistic speed (right). Note that the field lines point outward implying a positive charge.

ered large enough that the field inside is independent of separation distance, a Lorentz contraction will not result in any change in the charge density or electric field. Therefore, for electric fields parallel to the velocity one obtains,

$$E'_{\|} = E_{\|} \tag{1.2}$$

These results are general to all charge distributions. This is because the nature of the charge distributions does not determine the electric field in different frames of reference; it is instead determined from measurements made in a particular frame of reference.

One can first consider a stationary charged particle where the field lines emanate radially outward (Fig. 1.2). The electric field components are simply,

$$\begin{aligned} E_x &= \frac{qx}{(x^2+z^2)^{3/2}} \\ E_z &= \frac{qz}{(x^2+z^2)^{3/2}}. \end{aligned} \tag{1.3}$$

Interesting effects occur at velocities which are a substantial fraction of c as the field lines start to compress in order to catch up to the speed of the electron.

The compression occurs in the direction of the velocity. An induced magnetic field appears azimuthally around the fast charge, and the transverse component of the electric field increases in intensity. When the velocity reaches the speed of light, the transverse magnetic and electric fields are compressed into a central plane perpendicular to the velocity. For a point near the fast charge, the fields appear no different than those from a plane-polarized pulse of light [12].

For relativistic speeds, one can consider a point labeled A that is a distance b away from the trajectory of the fast charge (Fig. 1.3(a)). The point A experiences a transverse and longitudinal electric field, labelled as E_x and E_z respectively. The magnetic field B_y points out of the page. The strengths of the electric field components can be found from inserting Eq. (1.3) into Eq. (1.2) and Eq. (1.1), and converting the coordinates through Lorentz transformations. The resulting electric field components describing a moving charged particle is then expressed as [11, 12]

$$\begin{aligned} E_x &= \frac{\gamma q b}{(b^2 + \gamma^2 v^2 t^2)^{3/2}} \\ E_z &= -\frac{q\gamma v t}{(b^2 + \gamma^2 v^2 t^2)^{3/2}} \end{aligned} \tag{1.4}$$

where $\beta = v/c$ and γ is the relativistic factor. The transverse electric field profile over time is a sharp peak with width characterized by $b/v\gamma$ (Fig. 1.3(b)). A Fourier transform in frequency space can be plotted on a log scale, describing a broad-band spectrum (Fig. 1.3(c)) where the cutoff is determined by Bohr's adiabatic criterion [13], $\gamma v/b$.

Figure 1.4 gives an overview of the approximate cutoff condition depending on typical impact parameters and operating voltages. It can be seen that for a 200 kV operating voltage and typical impact parameters around 1~2 nm, the field contains Fourier components beyond the extreme-ultraviolet regime ($\sim 10^{17}$ Hz), offering a truly broad-band source of light.

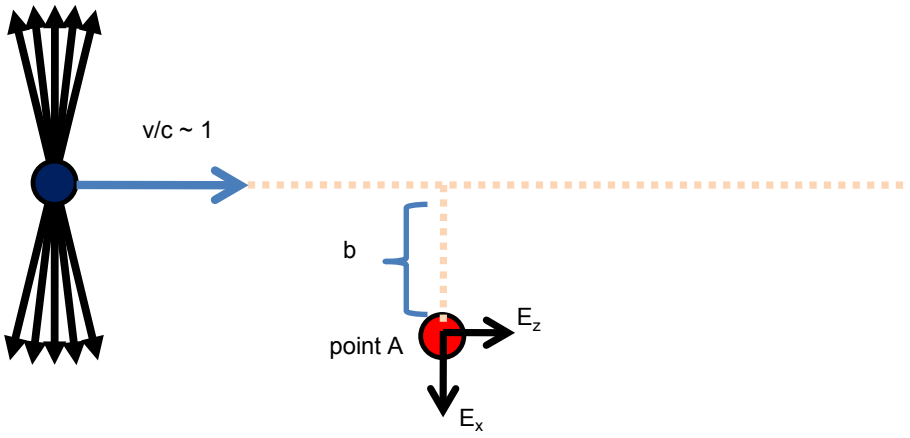

(a)

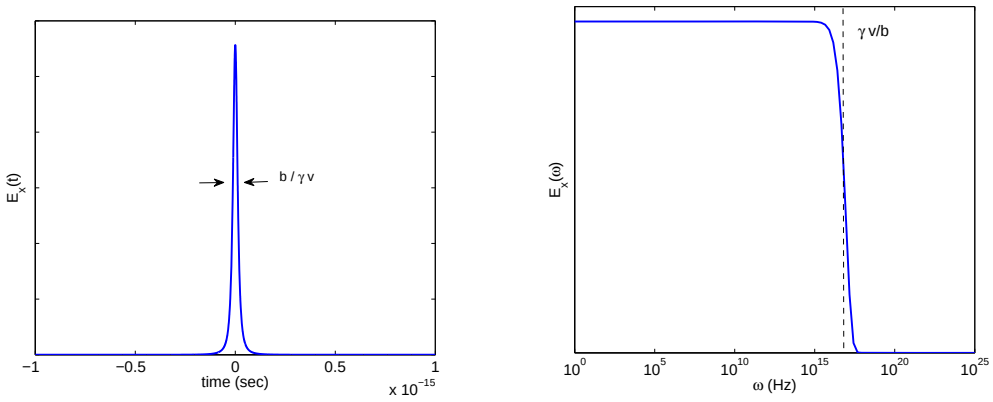

(b) (c)

Figure 1.3: (a) Point A at impact parameter b feels a strong transverse and weak longitudinal electric component due to the fast charge. The magnetic component points into the page. (b) The transverse electric field profile over time, which shows a sharp peak. (c) The Fourier transform of the transverse electric field, resulting in a broad-band spectrum.

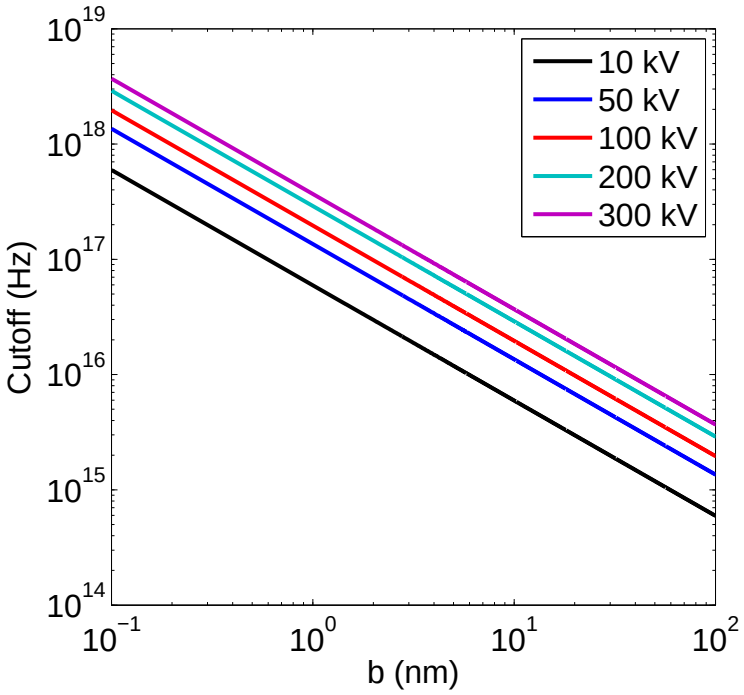

Figure 1.4: Log-log plot of the approximate cutoff condition. For typical impact parameters near 1 nm, the field from a fast electron can contain frequencies beyond the extreme-ultraviolet regime (~ 10^{17} Hz).

1.2 The Local Dielectric Approximation

Electron energy loss spectroscopy (EELS) on materials can provide different types of information depending on the energy range of interest. Energy losses due to interactions with the core electrons are relatively high in energy, and offers chemical signatures of the elemental states. Near the low-end of the energy range (typically below 50 eV), interactions with the valence electrons produce collective oscillations, also known as plasmons. Plasmon signals in this energy range offer high signal-to-noise ratios, and depend on the atomic density. The low-loss energy range, therefore, can be useful for distinguishing materials sharing slightly different chemical compositions or structural phases, by means of

energy-filtered (EF)TEM [14].

The wavelength of a collective oscillation is far larger than the interatomic spacing, allowing the material to be described by a continuum medium theory and characterized by a macroscopic dielectric function, $\epsilon(\vec{q}, \omega)$ [15]. It is important to note: when the size of the material is so small that the valence band can longer be considered as a continuum, use of the bulk dielectric function ceases to be valid. STEM/EELS experiments on silver particles demonstrated that for radii less than 4 nm, quantum effects emerge and the continuum theory fails [16]. Such length scales depend on the material properties, most notably the atomic density which is indicated by the plasmon energy. In this work, the target dimensions are well above their quantum thresholds, and therefore descriptions through the dielectric function are well-justified.

Since the dielectric function describes the polarization dependence on an external electric field, it is what connects the material to its optical properties. The local displacement vector, or the field inside a medium, can be written as

$$\vec{D}(\vec{r}, t) = \int_{-\infty}^{\infty} dt' \int_{-\infty}^{\infty} d\vec{r}' \, \epsilon(t - t', \vec{r} - \vec{r}')\vec{E}(\vec{r}', t) \tag{1.5}$$

where the dielectric constant here describes a real-space, real-time response. The Fourier transform in frequency space is

$$\vec{D}(\vec{r}, \omega) = \int_{-\infty}^{\infty} d\vec{r}' \, \epsilon(\vec{r} - \vec{r}', \omega)\vec{E}(\vec{r}', \omega). \tag{1.6}$$

For a homogeneous medium, one can assume the spatial response of the field to be local. This means that the local displacement field at $\vec{r}$ only depends on the electric field at $\vec{r}$. Considering this local approximation, one can write the dielectric function as

$$\epsilon(\vec{r} - \vec{r}', \omega) = \delta(\vec{r} - \vec{r}')\epsilon(\omega). \tag{1.7}$$

The dielectric function can then be written as

$$\vec{D}(\vec{r},\omega) = \epsilon(\omega)\vec{E}(\vec{r},\omega). \tag{1.8}$$

The local approximation implies $\epsilon(\omega)$ is independent of $\vec{q}$. The assumption is justified by the fact that for most EELS measurements, the collection angle, which is related to $\vec{q}$, is reasonably small such that variation in the dielectric function is small.

For anisotropic mediums, the dielectric function takes the form of a tensor. And for non-local optical responses, the dielectric function is calculated by the convolution relation in (1.5). The Fourier transform is a simple multiplication relation, $\underline{\vec{D}}(\vec{q},\omega) = \underline{\epsilon}(\vec{q},\omega)\,\underline{\vec{E}}(\vec{q},\omega)$.

A continuum theory permits the description of interband transitions, plasmon excitations and radiative losses from EELS [15].

There has been considerable theoretical and experimental work on optical measurements in an electron microscope environment. Studies on the coupling between small metallic particles were undertaken by Batson [17].The optical interaction between a thin film and a perpendicularly-incident fast electron were studied analytically by Ritchie and Eldridge [18]. Otto also considered a fast electron impinging from an arbitrary direction [19]. These studies were experimentally verified in aluminum films by Vincent and Silcox [20], and subsequently in graphite films by Chen and Silcox [21], where measurements were performed using angle-resolved EELS, providing maps of surface-guided modes.

Kroger described the loss of energy due to Cherenkov radiation analytically [22]. Retardation effects for an aloof (i.e., beam outside sample) electron trajec-

tory were considered by Garcia-Molina *et al.* [23]. Recently, Yurtsever observed guided Cherenkov modes in Si and Si-nanocomposite slabs which were correlated to the PDOS [24]. Garcia de Abajo also predicted the use of Cherenkov radiation for probing photonic structures [25] and proved the correspondence between EELS and the photonic density of states (PDOS) [26].

Moreover, recent developments in the stability of the electron source and monochromation have improved energy resolution and allowed detection of modes with life-times on the order of 100 meV. This has also made the infrared-visible energy range more accessible through the reduction of the zero-loss peak (ZLP) tails, generated by electrons undergoing little or no inelastic losses. Studies on Cherenkov radiation in Si-based nanocomposites [24], and delocalization in ultra-thin gate stacks [27] have directly benefited from this instrumental improvement.

1.3 Relativistic Energy Losses

Retardation plays a significant role for electron velocities in the relativistic regime and for target sizes on the order of the light wavelength. Two main classes of energy-loss mechanisms exist due to retardation and are categorized as Cherenkov or Transition radiation [12].

Cherenkov radiation is first considered. A simplistic picture of the origin of emission of light for an aloof electron is captured in Fig. 1.5. A stationary electron near a target surface induces a net polarization that points perpendicular to the surface and into the material. For an electron moving at relativistic speeds the situation is different. Because the radially symmetric field lines compress in

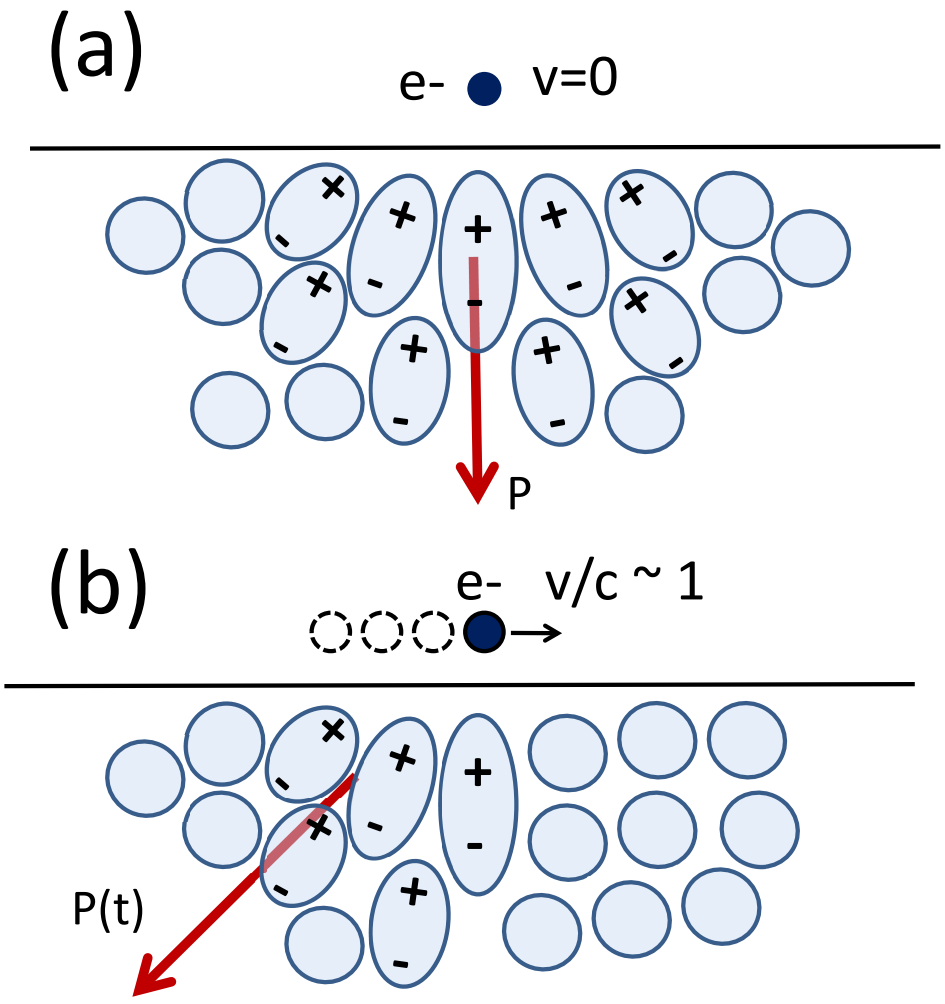

Figure 1.5: (a) A stationary electron near a target surface induces a net polarization vector directed perpendicular to the surface and into the material. (b) Due to the retarded fields of a fast electron, the molecules ahead of the electron do not feel a field. A resulting net polarization vector is time-varying and is oriented at an angle to surface.

the direction of propagation, molecules ahead of the electron do not feel a field. The net polarization vector then points at an angle to the surface and is time-varying. The rapid time variation of the polarization vector generates light. For the light to transform into a far-field response, a coherence condition must be met. When the electron is moving at speeds exceeding the speed of light in the medium, the wavefront of shock waves interfere coherently and create a coherent response that escapes into infinity [12].

Transition radiation is conventionally referred to as radiation emitted from a fast particle traversing two different mediums, resulting from the rearrangement of the field distribution. The displacement field in vacuum maintains a different intensity from the field in a target. As the electron traverses from vacuum into the target, the field distribution has to change over the interface. This change generates light. The coherence condition is met when at least one standing wave can develop inside the characteristic dimension of the structure. For this reason, structures with characteristic dimensions smaller than the wavelength fail to show effects of retardation.

Although transition radiation is often considered to be parasitic and deleterious in nature, a different interpretation shows how it can be useful, especially in identifying optical eigenmodes of structures.

CHAPTER 2

MEASURING WHISPERING GALLERY MODES OF SILICON OXIDE NANOSPHERES

2.1 An Introduction to Whispering Gallery Modes

The problem concerning the interaction between light and a single sphere was first solved by Mie over a century ago [28]. Appropriately, the optical eigenmodes were called Mie modes, also known as whispering gallery modes (WGMs). The term whispering gallery mode was coined by Rayleigh who observed the large resonance of whispers at the St. Paul cathedral dome in London (Fig. 2.1), and explained the observation as the formation of an acoustic standing wave within the dome.

An intuitive picture of a photonic WGM can be understood in terms of Snell's law. Fig. 2.2 illustrates two separate mediums where the top medium has a lower index of refraction than the bottom medium. When light enters from the bottom medium and hits the interface, refraction and reflection occur according to Snell's law. The angle of refraction is always larger than the angle of incidence due to the smaller index of refraction in the top medium (Fig. 2.2(a)). Therefore, an increase in the angle of incidence up to a certain critical angle ($\theta_i > \theta_c$) can result in the disappearance of any propagating refracted wave and 100% reflection of the incident wave (Fig. 2.2(b)). This phenomenon is known as total internal reflection. In the same spirit, light inside a dielectric sphere carrying a higher index of refraction than its surrounding medium may experience a continuous series of total internal reflections at the surface, ultimately forming a standing wave around the circumference of the sphere (Fig. 2.3). In reality, the dielectric

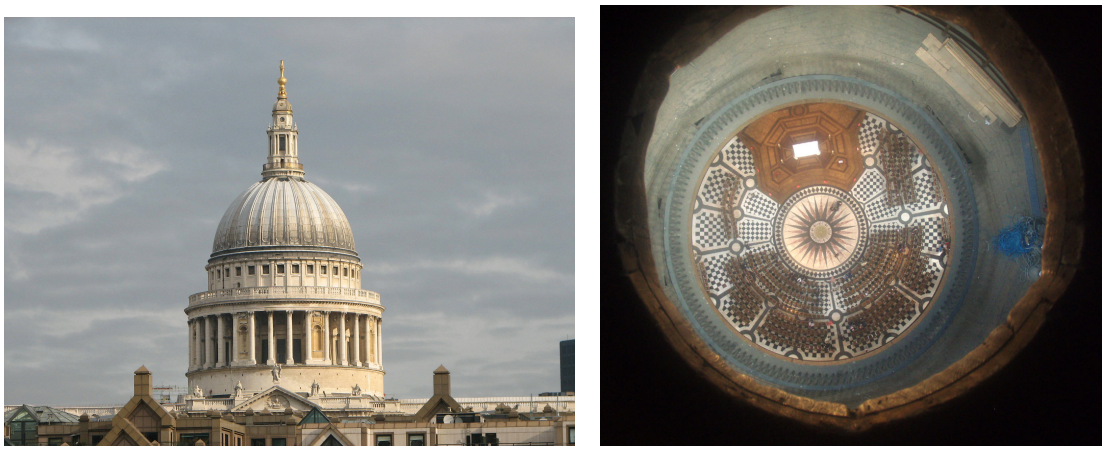

(a) (b)

Figure 2.1: (a) St. Paul's cathedral located in London. (b) One of the domes inside the cathedral. In such structures, acoustic waves can form standing waves around the wall, and can result in the resonance of whispers. Hence the term whispering gallery.

sphere cannot trap the light indefinitely, and leaks light through imperfections and absorption resulting in a transient photonic bound state.

The ability for dielectric spheres to trap and enhance light through whispering gallery modes (WGMs) has enabled applications such as strong-coupling cavity quantum electrodynamics (QED) [29, 30], bio-sensors [31], high-energy charged-particle accelerators [32] and photonic crystal wave guides [3]. Classical electromagnetism identifies WGMs as the delocalized response of the sphere to incoming light generated by retardation effects, where the size of the sphere and the dielectric constant set the characteristic widths and frequencies of the radiative modes [33]. WGM studies have generally focused on microspheres where Q factors greater than 10^6 may be obtained [29, 34]. While dielectric spheres smaller than a micron may not support strong WGMs in the visible and infrared regime, they nonetheless play crucial roles in photonic crystal applications.

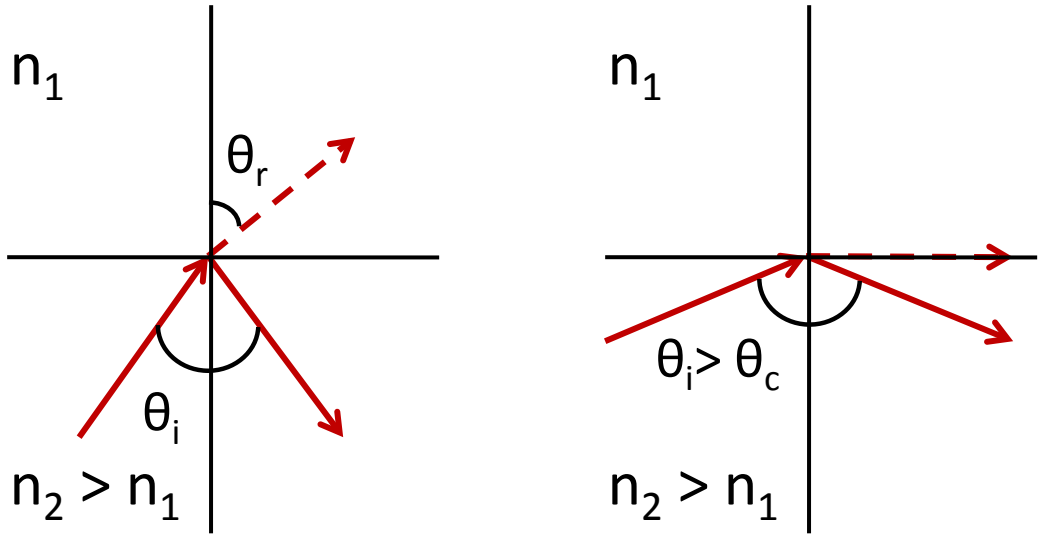

Figure 2.2: Illustration of Snell's law for two mediums sharing separate index of refractions. The top medium has a lower index of refraction than the bottom medium. (a) Light incident from the bottom medium experiences reflection and refraction at the interface according to Snell's law (b) When the angle of incidence, θ_i for the incident light exceeds a critical angle θ_c, refraction disappears and all light is reflected back.

The energy loss mechanism for the relativistic electron passing near the surface of the sphere is similar in nature to transition radiation, where the field before the sphere and the field penetrating inside the sphere have different spatial and temporal distributions. The readjustment of fields inside and outside the sphere causes the generation of light. For this light to propagate into the far-field a coherence condition must also be met. This condition is satisfied when at least one standing wave of the radiation can be formed around the circumference of the sphere (i.e., $ka > 1$).

The energy loss experienced by a relativistic fast electron near a sphere has recently been addressed by Garcia de Abajo through a multipole formalism in

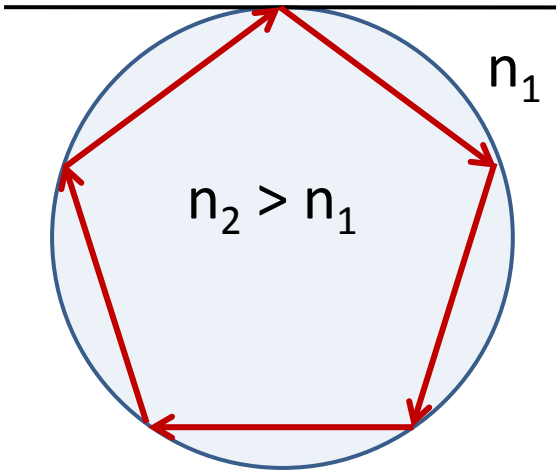

Figure 2.3: A simple geometrical interpretation of a whispering gallery mode inside a dielectric sphere. If the dielectric sphere has a higher index of refraction than its surrounding medium, light inside the sphere can experience continuous total internal reflections and result in a 'trapped' standing wave.

the local dielectric response approximation [35]. As the radiative modes are peaked within the bandgap where there is negligible absorption (i.e. $\mathrm{Im}(-1/\epsilon) \sim 0$ so no bulk loss mechanism is expected classically), it is easy to mistake the experimental radiative peaks as instead being indications of defect or surface states. Consideration of relativistic effects is therefore essential for a proper analysis.

2.1.1 A Quantum Mechanical Analogy

It is instructive to draw an analogy between light trapped in a dielectric sphere and the electron bound state in quantum mechanics. The analogy has been explored both by Ohtaka *et al.* [36] and Joannopoulos *et al.* [3], and is summarized

in this section. One starts with results from Maxwell's equations for the curl of the curl of the electric field,

$$\vec{\nabla} \times (\vec{\nabla} \times \vec{E}(\vec{r})) - \frac{\omega^2}{c^2} \epsilon(\vec{r}) \vec{E}(\vec{r}) = 0 \tag{2.1}$$

Eq. (2.1) can be rearranged using

$$\vec{\nabla} \times (\vec{\nabla} \times \vec{E}) = \vec{\nabla}(\vec{\nabla} \cdot \vec{E}) - \nabla^2 \vec{E}, \tag{2.2}$$

and by adding to both sides of the equation $(\omega^2/c^2)\vec{E}(\vec{r})$, one obtains

$$-\nabla^2 \vec{E}(\vec{r}) - \frac{\omega^2}{c^2}(\epsilon(\vec{r}) - 1)\vec{E}(\vec{r}) + \vec{\nabla}(\vec{\nabla} \cdot \vec{E}(\vec{r})) = \frac{\omega^2}{c^2}\vec{E}(\vec{r}). \tag{2.3}$$

Comparing this to the Schrödinger equation,

$$-\frac{\hbar^2}{2m}\nabla^2 \Psi(\vec{r}) + V(\vec{r})\Psi(\vec{r}) = E\Psi(\vec{r}) \tag{2.4}$$

The comparison between Eq. (2.3) and Eq. (2.4) shows that there exists subtle similarities. With the exception of the term $\vec{\nabla}(\vec{\nabla} \cdot \vec{E}(\vec{r}))$, Eq. (2.3) and Eq. (2.4) show a term-by-term correspondence. The presence of the term $\vec{\nabla}(\vec{\nabla} \cdot \vec{E}(\vec{r}))$ indicates that the equivalence is not complete. However, in the case of no charge or a uniform charge distribution, this term can be neglected. One can then draw an analogy between the potential term in the Schrödinger equation and the term, $-(\omega^2/c^2)(\epsilon(\vec{r}) - 1)$, in Eq. (2.3). This suggests that for $\epsilon > 1$, the dielectric sphere acts as an attractive potential for photons.

2.2 Excitation of Far-Ultraviolet Whispering Gallery Modes with Fast Electrons

2.2.1 Energy Loss for Fast Electrons near a Nanosphere

A 200 keV FEI tecnai F20-ST field-emission-gun STEM equipped with an electron monochromator was used. The convergence and collection semi-angles were 8 and 30 mrad respectively. Using the monochromator, the EELS energy spread was narrowed to 110 meV while the spatial resolution was around 4 nm. It is possible to improve the spatial resolution at the expense of reduced signal, but that was not needed for this work. Samples were prepared by dispersing SiO_2 spheres (Bang's Laboratory Inc.) in distilled water, and dropping them onto grids supporting films that consist of ultra-thin regions of carbon surrounded by relatively thicker carbon supports (Ted Pella Inc) (Fig. 2.4). The grids were then dried at room temperature. To minimize hydrocarbon buildup under the beam, the samples were placed in an Argon-ion plasma cleaner for 5 secs, a duration short enough to preserve the carbon supports.

The dielectric constant of SiO_2 was obtained from Palik [37] and is described in Fig. 2.5. The optical bandgap onset is around 9 eV, below which the imaginary component is negligible. For this reason, no bulk energy loss is predicted classically in this regime (i.e., $\mathrm{Im}(1/\epsilon) \sim 0$). The first interband transition is identified by the highest peak in the imaginary component at 10.5 eV. The classical energy loss spectra for an electron passing 5 nm away from the surface of a 276 nm and 162 nm size sphere are shown in Figure 4. The resemblance to the imaginary component of the dielectric function is clear for both sizes.

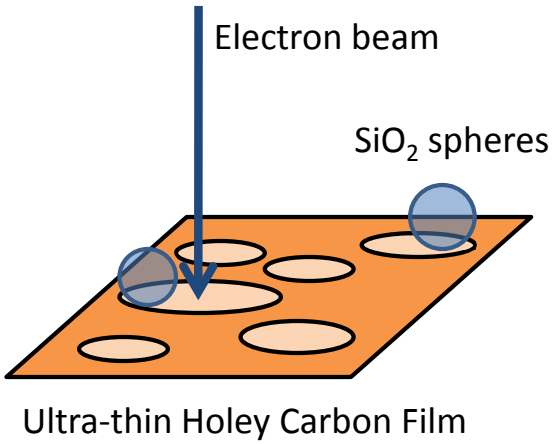

Figure 2.4: The experimental setup. SiO_2 spheres were deposited on ultrathin holey carbon film. Only the spheres located inside the ultra-thin carbon holes were investigated. The width of the electron beam was around 4 nm.

Fig. 2.6(a) and Fig. 2.6(b) show the energy loss spectra for an electron beam in vacuum passing ~5 nm away from the surface of a 276 nm and 162 nm size sphere, respectively, and the associated annular dark field (ADF) images. Spheres within the ultra-thin carbon regions were found close to, or in contact with, the boundaries where the film is thicker as seen in the ADF images. Therefore EELS measurements were not taken at positions close to the carbon/sphere interface in order to minimize contribution from the carbon background. The theoretical spectra were calculated using the multipole formalism of Garcia de Abajo [35, 38], where partial waves up to l=13 were summed for convergence. Below the ~9 eV band edge of SiO_2, where the dielectric function classically provides no loss features, the 276 nm sphere instead shows a rich set of peaks that agree well with the relativistic local dielectric theory. In general, decreasing the sphere size results in the scaling of eigenfrequencies to higher energies for a con-

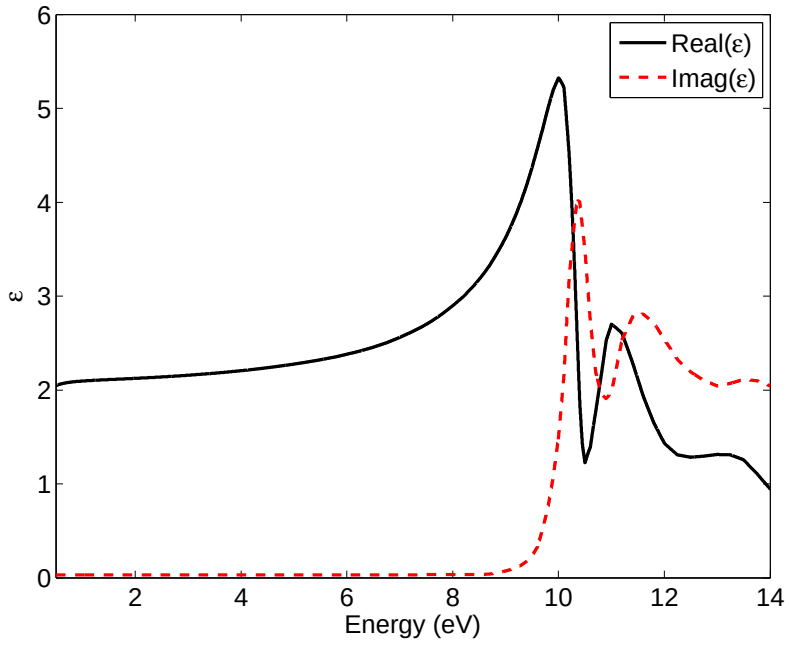

Figure 2.5: The dielectric function for SiO_2 in the energy range of 0.5 to 14 eV. A wide bandgap is observed below 9 eV. In this energy range, the imaginary component is negligible which signifies minimal absorption and good optical transmissivity.

stant real dielectric function. However for the case of a realistic semiconductor with an energy-dependent dielectric function, the modes above the band edge are absorbed by the sphere and only the lower order modes within the bandgap survive. This accounts for the reduction in number of modes in the smaller (162 nm) sphere as shown in Fig. 2.6(b).

Positioning the electron beam close to or on the spheres for more than 10 secs resulted in an increasingly bright spot at the location of the probe. This behavior is a well-known contamination problem, indicative of free hydrocarbons attracted to the charged electron beam. The hydrocarbons could originate from the spherical surface or the substrate. For simplicity, these hydrocarbons are modelled as 2nm layer of amorphous carbon surrounding the SiO_2 sphere.

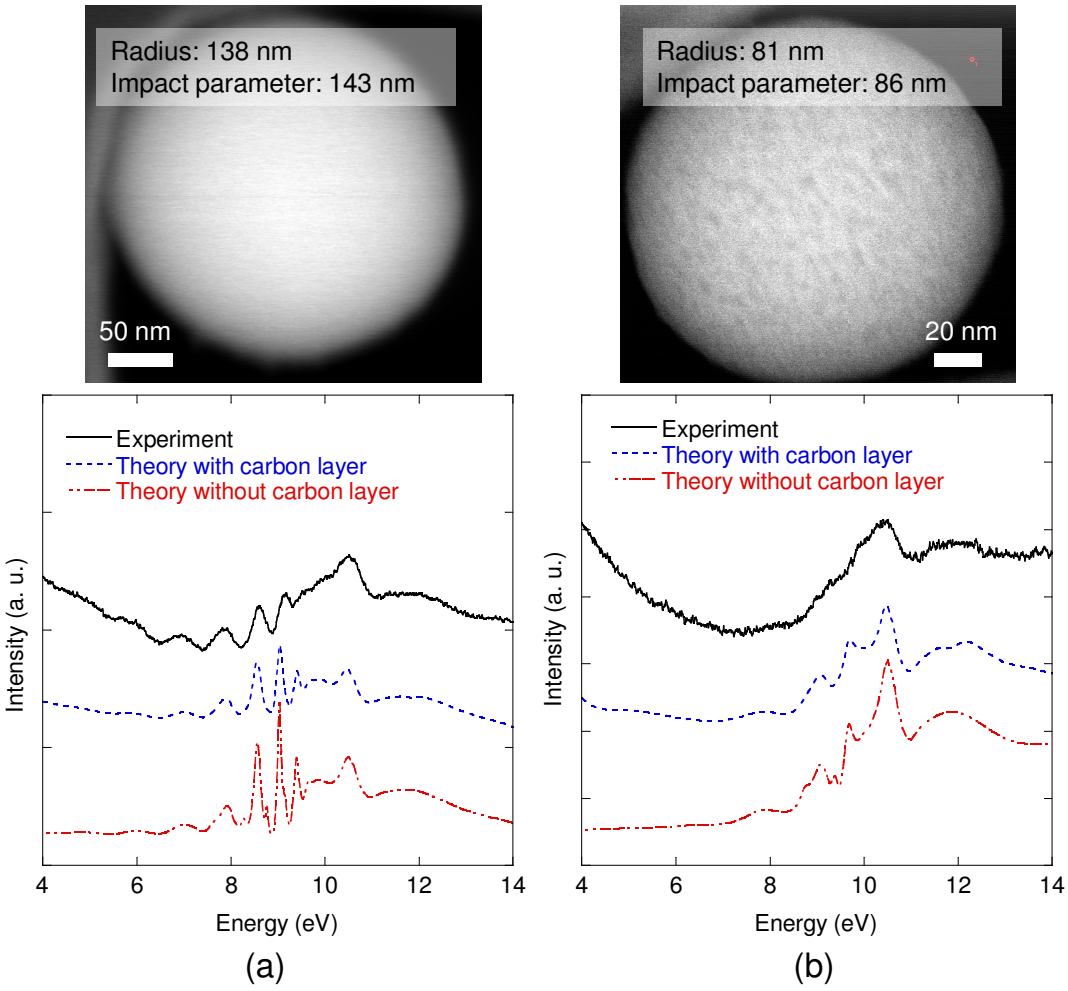

Figure 2.6: ADF images of a (a) 276 nm and (b) 162 nm silica sphere, their associated monochromated electron energy loss spectra, and calculated loss spectra (see Ref. 22 and 23) with and without a 2 nm thick amorphous carbon coating. For the loss spectra calculated with a 2 nm thick amorphous carbon coating, the silica sphere size is (a) 272 nm and (b) 158 nm. In all cases, the electron beam travels in vacuum 5 nm away from the outermost circumference.

Here, the thickness was used as a fitting parameter to give to best match to the experimental data. The dotted blue curves in Fig. 2.6(a) and Fig. 2.6(b) are the calculated loss spectra for a 272 nm and 158 nm silica sphere, respectively, coated with a 2 nm layer of amorphous carbon and excited by an electron traveling in vacuum at an impact parameter 5 nm away from the coating. The suppressed peak intensity and the broadened peak width indicate the absorption of radiation by the carbon coating, and show improved agreement with the experiment over the uncoated sphere model. In the absence of the carbon, the loss peaks below ~9 eV originate from the coupling of the incoming field of the electron to multipole WGM resonances, where the enhanced radiation inside the sphere leaks out into vacuum at a rate determined by the width of the loss peak. The Q factors for each resonance can be roughly estimated from Q= $E_0/\delta E$ where E_0 is the resonance energy and δE is the width of the peak. The contribution of the 110 meV energy resolution can be deconvolved through quadrature. A value of roughly Q ~ 24 for the resonance near 9 eV can be estimated.

For comparison, the classical electron energy loss probability for a 162 nm SiO_2 sphere is shown in Fig. 2.7. The same parameters used to generate the theory in Fig. 2.6(a) were used. The relativistic curve exhibits a higher intensity throughout the energy range. The classical treatment [39] does not take into account retardation, and therefore cannot predict the peaks under the bandgap.

2.2.2 The Electric-type Photonic Density of States

The transverse magnetic (TM) and transverse electric (TE) polarization of the field is analogous to the spin degree of freedom in the electronic bound state pic-

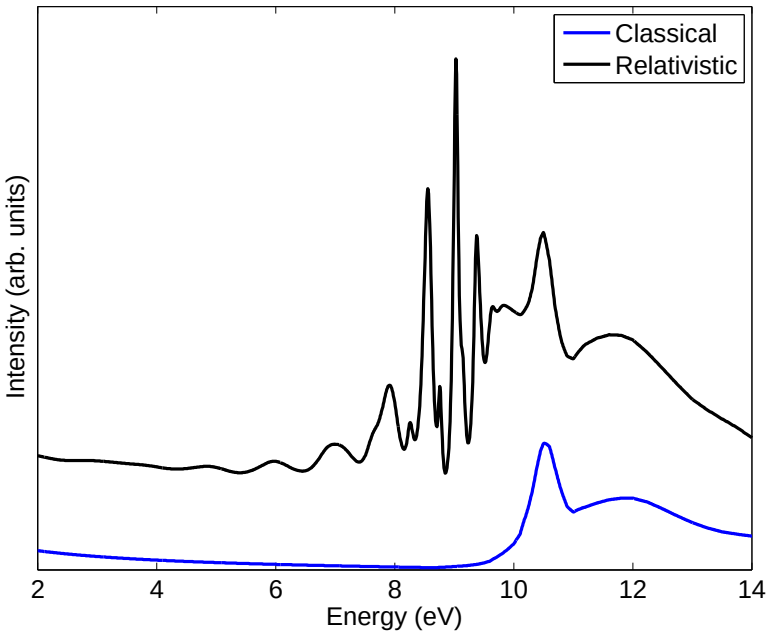

Figure 2.7: Comparison between the classical and relativistic electron energy loss probability calculated for a 276 nm diameter sphere. Both curves share the same reference, 0 (i.e., the curves have not been shifted with respect to each other in intensity). The impact parameter is 5 nm away from the surface. The energy of the electron is 200 kV.

ture [36] despite the subtle distinction that different polarizations share separate eigenenergies. Fig. 2.8 decomposes the theoretical loss spectrum for a 276 nm SiO_2 sphere into contributions from the TM and TE modes excited by a 200 keV electron. As the TM mode does not support a radial magnetic field component, one also refers to the mode as electric-type. Likewise, the TE mode does not support a radial electric field component, and is referred to as magnetic-type. The strength of the TE field largely depends on the magnetic field of the fast electron which is less than the electric field by a factor of v/c [12]. Therefore, the TE field can only become comparable to the TM field at ultra-relativistic speeds (i.e. $v \sim c$) [35]. For typical STEM operating voltages (i.e. $v/c = 0.5 \sim 0.7$),

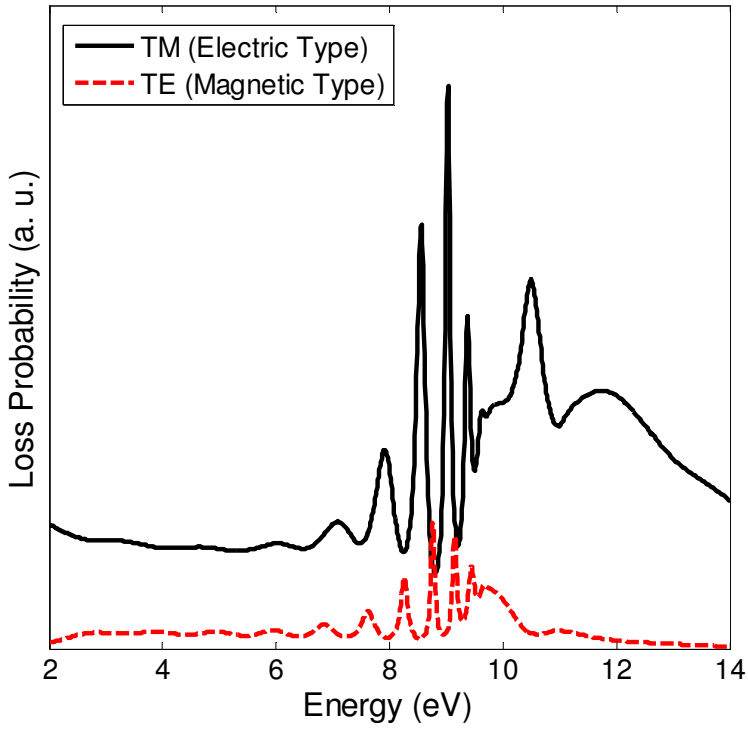

Figure 2.8: Contributions from TE (magnetic-type) and TM (electric-type) modes to the energy loss for the 276 nm silica sphere grazed by an electron traveling in vacuum 5 nm away from the circumference. The TM mode is the dominant contribution to the total energy loss.

the energy loss spectrum mostly reflects the contribution from the TM modes. This is especially true for the case of a system supporting an additional layer of thin absorbing material where the spectral features of the TE modes are easily damped out, as observable in Fig. 2.8. Consequently, as the DOS of the WGMs is dependent on the electric and magnetic scattering phase shifts [40], the total loss spectrum largely reflects features of the DOS profile of the electric-type WGMs.

Fig. 2.9 shows the contribution of each TM partial wave to the total TM loss probability shown in Fig. 2.8. Partial waves up to l=10 are considered. In a strict

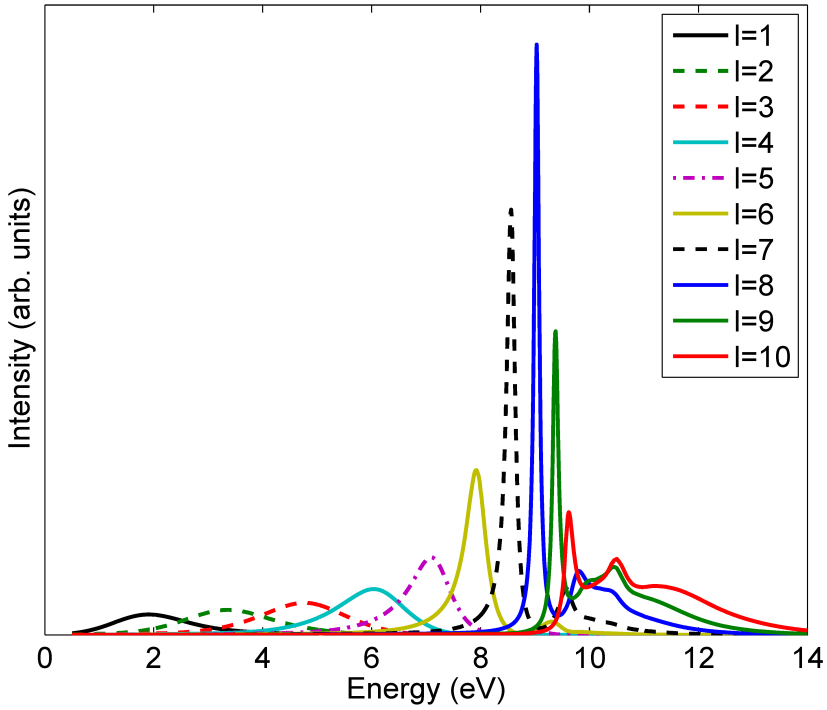

Figure 2.9: The contribution of individual TM partial waves, up to l=10, to the total loss probability. The peak energies increase while the peak widths decrease for increasing l.

sense, it is the sum of the partial waves divided by the energy that results in the TM profile in Fig. 2.8. In the energy range of consideration, each l describes a single peak. The peak energy increases while the width of the peak decreases for increasing l.

An intuitive picture of this behavior can be found from consideration of an effective potential [36]. One can take the potential-like term from Eq. (2.3) and add to it a centrifugal potential, $l(l+1)/r^2$ to construct an effective spherical potential:

$$V_{\text{eff}}(r) = -\frac{\omega^2}{c^2}(\epsilon(r) - 1) + \frac{l(l+1)}{r^2} \tag{2.5}$$

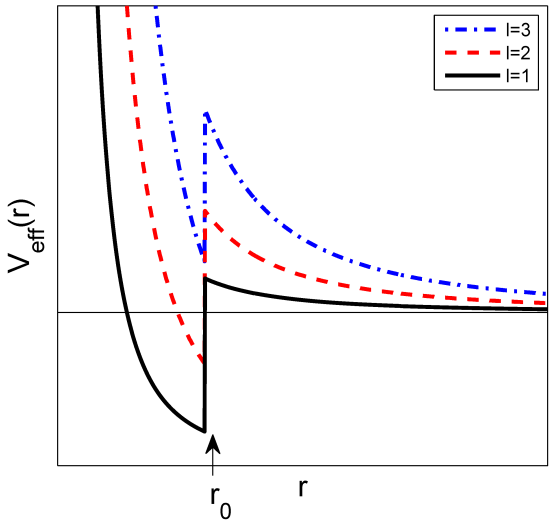

Figure 2.10: The effective potential model constructed from a ϵ-related term and a centrifugal potential (See Eq. (2.5)). Higher l lead to higher energy states and improved confinement.

One can consider a step function for the dielectric function,

$$\epsilon(r) = \begin{cases} \epsilon & \text{if } r < r_0 \\ 1 & \text{if } r > r_0 \end{cases} \tag{2.6}$$

Here, $\epsilon > 1$ in order to act as an attractive potential and r_0 is the radius of the sphere. Fig. 2.10 illustrates the behavior of V_{eff} for different l. It is clear that a higher l value leads to a rise in the minimum energy. This corresponds to higher possible energy states. Because the energies of a photonic 'bound' state are positive, higher l also corresponds to higher barrier height for a given energy. This also indicates that the confinement of the photon is stronger, leading to higher lifetimes and sharper EELS peak widths.

2.2.3 The Internal Field Distribution

Fig. 2.11 maps the internal $|H|$ field distribution of the TM polarization, composed of the sum of l=13 partial waves, at different characteristic energies for a 276 nm SiO2 sphere, viewed at different azimuthal slices (ϕ = 0, 45, and 90 deg). The field distribution is calculated within the central cross-section of a sphere whose radius extends to the impact parameter (b = 143 nm). The calculation of the internal field is outlined in Appendix A. From the boundary conditions, the transverse H field is continuous across the sphere-vacuum interface. The electron travels in vacuum in the x-z (ϕ = 0 deg) plane, parallel to the z axis, and 5 nm away from the surface of the sphere. For electric type WGM resonances at 8.556 eV and 9.028 eV, where the dielectric constant is effectively real, the intensity is largely concentrated in a series of anti-nodes inside the sphere along the circumference in the x-z plane. The two resonances are distinguished by the appearance of two additional anti-nodes in the intensity map of the 9.028 eV image. In the y-z slice (ϕ = 90 deg), intensity is focused near the top of the sphere, where the field of the electron impacts first during its trajectory and couples more efficiently. At 9.38 eV, a rising imaginary component of the dielectric constant reduces the contrast between the nodes and anti-nodes, suggesting partial absorption of field by the sphere. In addition, the asymmetry introduced by the off-axis electron path is enhanced. Above the optical gap onset at 10.5 eV, radiation is absorbed by the first interband transition, and the sphere fails to show any field confinement.

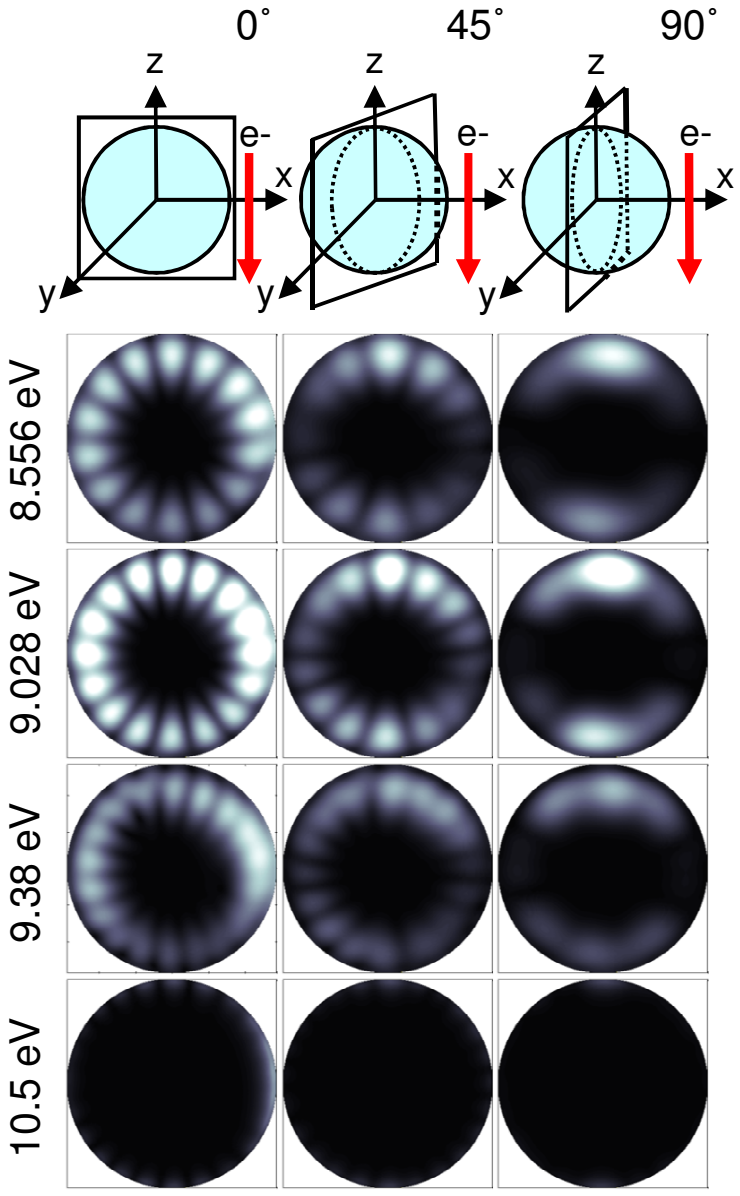

Figure 2.11: Azimuthal slices (ϕ= 0, 45, and 90 deg) showing the intensity map inside the 276 nm silica sphere. The images describe the TM |H| field at energies corresponding to characteristic peaks in the loss spectrum. The electron travels parallel to the z axis, 5 nm away from the surface of the sphere, and in the x-z (ϕ=0 deg) plane.

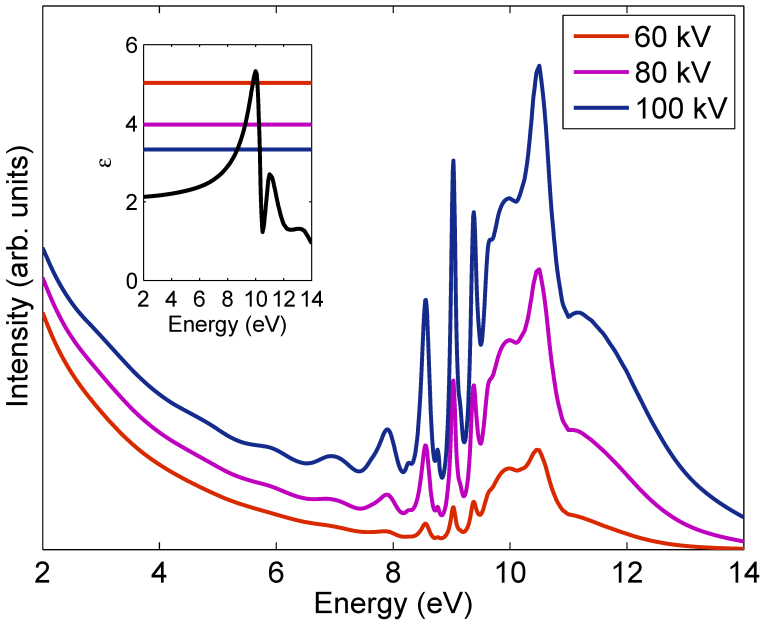

Figure 2.12: Electron energy loss probabilities for a 276 nm SiO_2 sphere at energies of 60, 80 and 100 kV. Impact parameter is 5 nm away from the surface. Inset describes the real part of the dielectric function for SiO_2 and the energy-dependent cutoff values,ϵ_{cf}, above which the Cherenkov condition is satisfied.

2.2.4 The Effect of Cherenkov Radiation

The excitations giving rise to the peaks in Fig. 2.6 are claimed to be most dominantly from transition radiation. This can be confirmed by qualitatively assessing the contribution of Cherenkov radiation to the peaks. Cherenkov radiation is emitted when the velocity of the electron is greater than the speed of light in the medium (i.e., $v > c/n$). This also translate to the condition, $\epsilon > \epsilon_{cf}$, where $\epsilon_{cf} = (c/v)^2$. Fig. 2.12 illustrates the energy loss probabilities for different electron energies at 60, 80 and 100 kV. Again the target is a 276 nm diameter SiO_2 sphere, and the electron beam is 5 nm away from the surface. The inset describes the corresponding ϵ_{cf} for 60, 80 and 100 kV, and real part of the dielectric function for SiO_2. The dielectric function above these values enables the emission

of Cherenkov radiation. The 80 kV beam corresponds to a ϵ_{cf} value of roughy 4. Therefore, between 9 and 10.25 eV, Cherenkov radiation is emitted. However, the corresponding energy loss probability shows peaks apparent below 9 eV, where the Cherenkov condition is not satisfied. Even at 60 kV, where the Cherenkov condition is satisfied only over a narrow energy range, peaks can be observed throughout the optical bandgap. This is a clear sign that Cherenkov radiation cannot account for the peaks.

CHAPTER 3

MEASURING THE OPTICAL EIGENMODES OF NANOWIRES

3.1 Introduction: Nanowires probed by EELS

Single nanowires have been demonstrated as building blocks for optoelectronic devices [41] including sensors [7] and nano-lasers [9, 42], while core-shell nanowire systems have shown promise as functional solar-cells [5, 6] and optical antennas [43]. Improvements in nanowire-device performance rely heavily on understanding the optical properties. When conventional optical techniques encounter diffraction limitations, scanning transmission electron microscopy offers an alternative approach to probing the nanoscale optical properties.

There have been numerous studies linking EELS to nanowires in the classical (non-relativistic) framework. Energy-loss probabilities for non-penetrating electrons normally incident near solid and hollow nanowires were theoretically investigated by Bertsch *et al.* [44] The formalism was extended by Zabala *et al.* to include penetrating trajectories [45]. Nanowires with anisotropic dielectric functions were also considered by Taverna *et al.* [46]. In the limit of slow electron velocities or small wire-diameters, the classical treatment should suffice for the description of energy-loss probabilities. However, it is also questionable whether a dielectric-continuum approach is even valid in the limit of small sizes, as quantum mechanical corrections may be necessary [46, 16]. For larger diameters where the valence band behaves as a continuum, a dielectric formalism is well-justified. For diameters exceeding the mode wave-length ($a > \lambda$), and with relativistic electron velocities, retardation effects arise, introducing the need for a relativistic treatment. This requirement is further strengthened from

a practical standpoint as optoelectronic devices typically employ nanowires of diameters greater than 50 nm to match the optical wavelength.

Relativistic formalisms for spheres [35], semi-infinite solids [18], stratified layers [47] and nanowires probed along the direction of the cylindrical axis [48, 49] have been previously addressed. Experimental evidence for whispering gallery modes in silica nanospheres probed by aloof electrons were shown in an earlier work [50]. However, to the author's knowledge, there has not yet been a relativistic study of solid or core-shell nanowires probed with aloof electrons. The Boundary element method (BEM) developed by de Abajo and Howie permits the calculation of energy-loss probabilities of various geometries using spatial discretization [51, 52]. An analytical derivation dedicated to the particular system of interest, however, benefits from the direct generation of a loss-dispersion map, especially useful for correlating spectroscopic features to the optical eigenmodes.

In this work, the field of the electron is expanded in vector cylindrical harmonics, and an analytical expression of the relativistic energy-loss probability for a fast electron normally incident near an infinite wire is derived. Experimental results on single GaN and Ge nanowires are compared to calculations, and excellent agreement is found. For the Ge nanowires, two diameters representing a zero-mode and multi-mode waveguide are studied.

3.2 Relativistic EELS for Solid and Core-shell Nanowires

The system consists of an infinite wire of inner radius a and outer radius c extending along the y-axis. The wire is positioned in vacuum (i.e. $\epsilon = 1$), and the

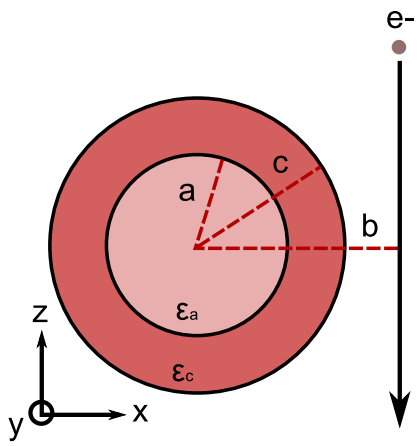

Figure 3.1: (Color online) Geometry of the experiment. The core-shell nanowire extends along the y-axis, and consists of an inner core of radius a, described by the dielectric function ϵ_a while the outer shell extends to radius c, described by ϵ_c. The aloof electron travels parallel to the z-axis and passes closest to the wire at a distance b from the center of the wire.

core and shell are characterized by frequency dependent dielectric functions, ϵ_a and ϵ_c respectively. The wire is considered to be non-magnetic (i.e. $\mu = 1$). An electron travels in vacuum at relativistic speeds, v parallel to the z-axis, and impinges near the surface of the wire. The nearest distance from the center of the wire to the path of the electron is along the x-axis and is described by the impact parameter, b.

The external field associated with the fast electron as it traverses near the wire is first expanded in terms of vector cylindrical harmonics. The interaction between this field and the wire is expressed as a scattering problem where the scattering matrix is determined from solutions to the boundary conditions. The energy-loss probability is then calculated from the work done on the electron as it experiences a retarding force from the scattered field.

3.2.1 Vector harmonics and scalar functions

To expand the electric field in terms of cylindrical harmonics, one can define the operator $\vec{S} = -i\hat{y} \times \vec{\nabla}$. This is analogous to $\vec{L} = -i\vec{r} \times \vec{\nabla}$ used as the angular momentum operator to generate spherical harmonics [35]. $\vec{S}$ in polar or cartesian coordinates takes the following forms:

$$\vec{S} = \frac{1}{i}\left(-\frac{\hat{r}}{r}\frac{\partial}{\partial\phi} + \hat{\phi}\frac{\partial}{\partial r}\right) \tag{3.1}$$

or,

$$\vec{S} = \frac{1}{i}\left(\hat{x}\frac{\partial}{\partial z} - \hat{z}\frac{\partial}{\partial x}\right). \tag{3.2}$$

Using this operator, the external electric and magnetic fields can be expressed as,

$$\vec{E}^{\alpha} = \vec{S}\Psi^{\alpha}_{\perp} - \tfrac{i}{k}\vec{\nabla} \times \vec{S}\Psi^{\alpha}_{\parallel} \tag{3.3}$$

$$\vec{H}^{\alpha} = -\tfrac{i}{k}\vec{\nabla} \times \vec{S}\Psi^{\alpha}_{\perp} - \vec{S}\Psi^{\alpha}_{\parallel} \tag{3.4}$$

where $k = \omega/c$ and the superscript α refers to the external or scattered fields, respectively labelled 'ext' or 'sct'. From Eq. (3.3),

$$\Psi^{\alpha}_{\perp} = \frac{\vec{S} \cdot \vec{E}^{\alpha}}{\vec{S} \cdot \vec{S}} \tag{3.5}$$

describes the scalar function associated with the electric field component polarized perpendicular to the cylindrical axis, and

$$\Psi^{\alpha}_{\parallel} = \frac{i}{k}\frac{(\vec{S} \times \vec{\nabla}) \cdot \vec{E}^{\alpha}}{\vec{S} \cdot \vec{S}} \tag{3.6}$$

describes the scalar function associated with the electric field component polarized parallel to the cylindrical axis. For the field inside the wire, however,

Maxwell's equations require the vector expressions to take a subtly different form involving the dielectric constant, ϵ_a, as

$$\vec{E}^{\text{int}} = \vec{S}\Psi_{\perp}^{\text{int}} - \frac{i}{\sqrt{\epsilon_a}k}\vec{\nabla} \times \vec{S}\Psi_{\parallel}^{\text{int}} \tag{3.7}$$

$$\vec{H}^{\text{int}} = -\frac{i}{k}\vec{\nabla} \times \vec{S}\Psi_{\perp}^{\text{int}} - \sqrt{\epsilon_a}\vec{S}\Psi_{\parallel}^{\text{int}}. \tag{3.8}$$

3.2.2 External field of the fast electron

One can describe the electric field of the moving electron as [35, 12]

$$\vec{E}^{\text{ext}}(\vec{x}) = \left(\vec{\nabla} - \frac{ik\vec{v}}{c}\right)\Phi^{\text{ext}} \tag{3.9}$$

where

$$\Phi^{\text{ext}}(\vec{x}, \omega) = \int dt\, e^{\pm iwt} G(\vec{x}, \vec{x_t}) \tag{3.10}$$

and $G(\vec{x}, \vec{x_t})$ is the Green's function for the wave equation ($(\nabla^2 + k^2)G = 0$),

$$G(\vec{x}, \vec{x_t}) = \frac{e^{ik|\vec{x}-(b,0,vt)|}}{|\vec{x} - (b, 0, vt)|} \tag{3.11}$$

The Green's function can be expanded in terms of cylindrical harmonics as

$$G(\vec{x}, \vec{x_t}) = \frac{i}{2}\sum_m e^{im(\phi-\phi_t)} \int_{-\infty}^{\infty} dg\, e^{ig(y-y_t)} H_m^{(1)}(ur_t) J_m(ur) \tag{3.12}$$

where g is the axial propagation constant, $u = \sqrt{k^2 - g^2}$, and $r < r_t$. $H_m^{(1)}(ur_t)$ is a bessel function of the third kind defined by, $H_m^{(1)}(x) = J_m(x) + iN_m(x)$. Substituting the cylindrical harmonics expansion of the spherical wave Eq. (3.12) into Eq. (3.10), one finds

$$\Phi^{\text{ext}}(\vec{x}, \omega) = \frac{i}{2}\sum_m e^{im\phi} \int_{-\infty}^{\infty} dg\, e^{igy} J_m(ur) \Psi_{gm}(\vec{x_0}) \tag{3.13}$$

where

$$\Psi_{gm}(\vec{x_0}) = \int dt\, e^{iwt} e^{-im\phi_t} e^{-igy_t} H_m^{(1)}(ur_t). \tag{3.14}$$

It is $\Psi_{gm}(\vec{x_0})$ which will describe the expansion coefficients of the moving electron's field. In order to find $\Psi_{gm}(\vec{x_0})$, one can rewrite Eq. (3.13) as

$$\Psi_{gm}(\vec{x_0}) = -\frac{2i}{(2\pi)^2 J_m(ur)} \Phi_{gm}^{\text{ext}}(r, \omega) \tag{3.15}$$

where

$$\Phi_{gm}^{\text{ext}}(r, \omega) = \int_0^{2\pi} \int_{-\infty}^{\infty} d\phi\, dy\, e^{-im\phi} e^{-igy} \Phi^{\text{ext}}(\vec{x}, \omega) \tag{3.16}$$

In short, $\Phi_{gm}^{\text{ext}}(r, \omega)$ is the cylindrical representation of $\Phi^{\text{ext}}(\vec{x}, \omega)$, and one returns to Eq. (3.10) to convert the potential into its cylindrical expansion. One can start from [12]

$$\Phi^{\text{ext}}(\vec{k}, \omega) = \frac{2\delta(\omega - \vec{k} \cdot \vec{v})}{k^2 - \frac{\omega^2}{c^2}} \tag{3.17}$$

which is the spatial Fourier transform of the potential. Taking the spatial Fourier transform of Eq. (3.16) in terms of the electron's initial coordinates when $\vec{x}(t = 0) = (b, y_0, z_0)$, one obtains

$$\Phi^{\text{ext}}(\vec{x}, \omega) = \frac{e^{i\omega(z - z_0)/v}}{\pi v} \int dk_x\, dg\, \frac{e^{ik_x(x-b)} e^{ig(y-y_0)}}{k_x^2 + g^2 + (\omega/v\gamma)^2} \tag{3.18}$$

Here, γ is the relativistic factor. The k_x integral is simply

$$\int \frac{e^{ik_x(x-b)}}{k_x^2 + \lambda^2}\, dk_x = \frac{\pi e^{-|x-b|\lambda}}{\lambda} \tag{3.19}$$

where $\lambda^2 = g^2 + (\frac{\omega}{v\gamma})^2$. Then in the cylindrical (m,g,r) representation, Eq. (3.18) becomes

$$\Phi_{gm}^{\text{ext}}(r, \omega) = \frac{2\pi e^{-i\omega z_0/v} e^{-igy_0}}{v} \int_0^{2\pi} d\phi\, e^{-im\phi} e^{i\omega z/v} \frac{e^{-|x-b|\lambda}}{\lambda} \tag{3.20}$$

$|x - b|$ can be rewritten as $(b - x)$ since the region of interest is where $r < b$. With $x = r\cos\phi$ and $z = r\sin\phi$, Eq. (3.20) becomes

$$\Phi_{gm}^{\text{ext}}(r, \omega) = \frac{2\pi e^{-i\omega z_0/v} e^{-igy_0}}{v} \frac{e^{-b\lambda}}{\lambda} \int_0^{2\pi} d\phi\, e^{-im\phi} e^{i\omega r \sin(\phi)/v} e^{r\cos(\phi)\lambda} \tag{3.21}$$

The form of the integral has been solved by Bertsch *et al*.[44] without the relativistic factor. Including the relativistic factor, the integral in Eq. (3.21) is expressed as

$$\int_0^{2\pi} d\phi\, e^{-im\phi} e^{i\omega r \sin(\phi)/v} e^{r\cos(\phi)\lambda} = 2\pi \left(\frac{\lambda + \omega/v}{\sqrt{g^2 - k^2}} \right)^m I_m(r\sqrt{g^2 - k^2}) \tag{3.22}$$

where I_m is the modified Bessel function of the first kind. Combining Eq. (3.21) and Eq. (3.22) and inserting this into Eq. (3.15), one can write $\Psi_{gm}(\vec{x_0})$ as

$$\Psi_{gm}(\vec{x_0}) = \frac{-2i}{v} \frac{e^{-i\frac{\omega}{v}z_0} e^{-igy_0} e^{-b\lambda}}{\lambda} \left(\frac{\lambda + \omega/v}{\sqrt{g^2 - k^2}} \right)^m \frac{I_m(r\sqrt{g^2 - k^2})}{J_m(ur)} \tag{3.23}$$

However, since $\Psi_{gm}(\vec{x_0})$ needs to be independent of r, one can take the limit of I_m and J_m as $r \to 0$. $\Psi_{gm}(\vec{x_0})$ then is expressed as

$$\Psi_{gm}(\vec{x_0}) = \frac{-2i}{v} \frac{e^{-i\frac{\omega}{v}z_0} e^{-igy_0} e^{-b\lambda}}{\lambda} \left(\frac{\lambda + \omega/v}{u} \right)^m \tag{3.24}$$

3.2.3 The Expansion Coefficients

Here, the derivation of $\Psi_\perp^{ext}$ is outlined. One can start with the numerator of Eq. (3.5).

$$\vec{S} \cdot \vec{E}^{ext} = \vec{S} \cdot \left(\vec{\nabla} - \frac{ik\vec{v}}{c} \right) \Phi^{ext}(\vec{x}, \omega) \tag{3.25}$$

One sees that $\vec{S} \cdot \vec{\nabla} = 0$, and as the electron travels along the z axis, $\vec{v} = v\hat{z}$, one obtains with Eq. (3.2),

$$\vec{S} \cdot \vec{E}^{\text{ext}} = \frac{kv}{c} \frac{\partial \Phi^{\text{ext}}(\vec{x}, \omega)}{\partial x} \tag{3.26}$$

The difficulty with the partial derivative in the Cartesian basis on cylindrical harmonics can be overcome by realizing a trick employing the Green's function [35]. One can observe from Eq. (3.11) that the partial derivative of the Green's function with respect to the present position is the negative of the partial derivative with respect to the initial position, (ie., $\partial/\partial x = -\partial/\partial x_0$). $\Phi^{\text{ext}}(\vec{x}, \omega)$ involves

$\Psi_{gm}(\vec{x_0})$) where the initial position, (b, y_0, z_0), is conveniently expressed in Cartesian coordinates. One can now write

$$\vec{S} \cdot \vec{E}^{\text{ext}} = -\frac{ikv}{2c} \sum_m e^{im\phi} \int dg\, e^{igy} J_m(ur) \frac{\partial \Psi_{gm}(\vec{x_0})}{\partial b} \tag{3.27}$$

The denominator of Eq. (3.5), $\vec{S} \cdot \vec{S}$, can be obtained working in the cylindrical basis using Eq. (3.1) and employing the recursive Bessel function identities. One then obtains $\vec{S} \cdot \vec{S} => -u^2$. $\Psi_{\perp}^{\text{ext}}$ can now be expressed as

$$\Psi_{\perp}^{\text{ext}} = \frac{i}{2} \sum_m e^{im\phi} \int dg\, e^{igy} J_m(ur) \Psi_{gm\perp}^{\text{ext}} \tag{3.28}$$

where the expansion coefficient $\Psi_{gm\perp}^{\text{ext}}$ is

$$\Psi_{gm\perp}^{\text{ext}} = -\frac{kv}{c\, u^2} \frac{\partial \Psi_{gm}(\vec{x_0})}{\partial b} \tag{3.29}$$

The parallel polarization can be found in a similar manner. One can first simplify the numerator of Eq. (3.6) from

$$\frac{i}{k}(\vec{S} \times \vec{\nabla}) \cdot \vec{E} = \frac{i}{k}(\vec{S} \times \vec{\nabla}) \cdot \left(\vec{\nabla} - \frac{ik\vec{v}}{c}\right) \Phi^{\text{ext}}(\vec{x}, \omega) \tag{3.30}$$

to

$$\frac{i}{k}(\vec{S} \times \vec{\nabla}) \cdot \vec{E} = -\frac{iv}{c} \frac{\partial}{\partial z} \frac{\partial}{\partial y} \Phi^{\text{ext}}(\vec{x}, \omega) \tag{3.31}$$

by realizing that $(\vec{S} \times \vec{\nabla}) \cdot \vec{\nabla} = 0$. Again one can use the trick above for relating the partial derivative of the Green's function with respect to the current position to the initial position. Applying $\vec{S} \cdot \vec{S} => -u^2$ in the denominator of Eq. (3.6) one obtains for the parallel basis,

$$\Psi_{\parallel}^{\text{ext}} = \frac{i}{2} \sum_m e^{im\phi} \int dg\, e^{igy} J_m(ur) \Psi_{gm\parallel}^{\text{ext}} \tag{3.32}$$

where the expansion coefficient $\Psi_{gm\parallel}^{\text{ext}}$ is

$$\Psi_{gm\parallel}^{\text{ext}} = \frac{iv}{c\, u^2} \frac{\partial}{\partial z_0} \frac{\partial}{\partial y_0} \Psi_{gm}(\vec{x_0}) \tag{3.33}$$

3.2.4 Scattering matrix

The case of a solid wire (i.e. $\epsilon_c = 1$) is first considered. The forms for $\Psi_{\perp}^{\text{sct}}$ and $\Psi_{\parallel}^{\text{sct}}$, describing the scattered fields, can be found by choosing the well-behaved Bessel function at $r \to \infty$. One finds that

$$\Psi_l^{\text{sct}} = \frac{i}{2} \sum_m e^{im\phi_t} \int dg\, e^{igy_t} H_m^{(1)}(ur_t) \Psi_{gm\,l}^{\text{sct}} \tag{3.34}$$

where l indicates the polarization ($\perp$ or $\parallel$). For the internal fields, one finds $\Psi_l^{\text{int}} \sim J_m(u_a r)$ where $u_a = \sqrt{\epsilon_a k^2 - g^2}$ is necessary to satisfy the wave equation inside the dielectric, $(\nabla^2 + \epsilon_a k^2)\Psi^{\text{int}} = 0$. The scattered field is of most interest since it is this field that will interact with the electron and force the loss in its energy. One can write the scattered field expansion coefficients as

$$\begin{pmatrix} \Psi_{gm\perp}^{\text{sct}} \\ \Psi_{gm\parallel}^{\text{sct}} \end{pmatrix} = \begin{pmatrix} a_{m\perp} & a_{m\parallel} \\ b_{m\perp} & b_{m\parallel} \end{pmatrix} \begin{pmatrix} \Psi_{gm\perp}^{\text{ext}} \\ \Psi_{gm\parallel}^{\text{ext}} \end{pmatrix} \tag{3.35}$$

The scattering matrix can be found by imposing the appropriate Maxwell boundary conditions, which require that the tangential components of the electric and magnetic fields be continuous at the boundary of the wire. Or,

$$(\vec{E}^{\text{ext}} + \vec{E}^{\text{sct}} - \vec{E}^{\text{int}})_{r=a} \times \hat{r} = 0 \tag{3.36}$$

$$(\vec{H}^{\text{ext}} + \vec{H}^{\text{sct}} - \vec{H}^{\text{int}})_{r=a} \times \hat{r} = 0 \tag{3.37}$$

With some algebra, one obtains

$$a_{m\perp} = \frac{DC - FA}{FB - EC} \tag{3.38}$$

$$a_{m\parallel} = \frac{DB - EA}{FB - EC} \frac{\Psi_{gm\perp}^{ext}}{\Psi_{gm\parallel}^{ext}} \tag{3.39}$$

$$b_{m\perp} = \frac{GH - FC}{FB - EH} \frac{\Psi_{gm\parallel}^{ext}}{\Psi_{gm\perp}^{ext}} \tag{3.40}$$

$$b_{m\parallel} = \frac{GB - EC}{FB - EH} \tag{3.41}$$

where

$$
\begin{aligned}
A &= ika(u_a^2 u J'_m(ua)J_m(u_a a) - u_a u^2 J'_m(u_a a)J_m(ua)) \\
B &= ika(u_a^2 u J_m(u_a a)H'^{(1)}_m(ua) - u_a u^2 J'_m(u_a a)H^{(1)}_m(ua)) \\
C &= mgJ_m(u_a a)H^{(1)}_m(ua)(u^2 - u_a^2) \\
D &= mgJ_m(u_a a)J_m(ua)(u_a^2 - u^2) \\
E &= mgJ_m(u_a a)H^{(1)}_m(ua)(u_a^2 - u^2) \\
F &= ika(u_a^2 u J_m(u_a a)H'^{(1)}_m(ua) - \epsilon_a u_a u^2 J'_m(u_a a)H^{(1)}_m(ua) \\
G &= ika(\epsilon_a u_a u^2 J'_m(u_a a)J_m(ua) - u_a^2 u J_m(u_a a)J'_m(ua) \\
H &= mgJ_m(u_a a)H^{(1)}_m(ua)(u^2 - u_a^2)
\end{aligned}
$$

For the core-shell nanowire, the Bessel function inside the scalar function describing the shell region ($a < r < c$) is a linear combination of $J_m(u_c r)$ and $Y_m(u_c r)$ where $u_c = \sqrt{\epsilon_c k^2 - g^2}$. Again the boundary conditions for the electric and magnetic fields are satisfied, and extensive algebra generates an analytical solution for the scattering matrix elements (See Appendix C).

3.2.5 Energy loss

The energy loss experienced by an electron due to the induced field can be written as

$$E^{\text{loss}} = \int_0^\infty \omega \, d\omega \, \Gamma^{\text{loss}}(\omega) \tag{3.42}$$

where

$$\Gamma^{\text{loss}}(\omega) = \frac{1}{\pi\omega} \int dt \, Re\left\{e^{i\omega t}\vec{v} \cdot \vec{E}^{sct}(\vec{r_t}, \omega))\right\} \tag{3.43}$$

represents the energy-loss probability. Inserting Eq. (3.3) for the scattered electric field, one finds

$$\Gamma^{\text{loss}}(\omega) = \frac{1}{\pi\omega}\int dt\, Re\left\{e^{-i\omega t}\left(\vec{v}\cdot\vec{S}\Psi_{\perp}^{sct} - \frac{i}{k}\vec{v}\cdot(\vec{\nabla}\times\vec{S})\Psi_{\parallel}^{sct}\right)\right\} \tag{3.44}$$

From Eq. (3.34) and Eq. (3.35) one obtains

$$\Psi_{\perp}^{\text{sct}} = \frac{i}{2}\sum_m e^{im\phi_t}\int dg\, e^{igy_t}H_m(ur_t)(a_{m\perp}\Psi_{gm\perp}^{\text{ext}} + a_{m\parallel}\Psi_{gm\parallel}^{ext}) \tag{3.45}$$

$$\Psi_{\parallel}^{\text{sct}} = \frac{i}{2}\sum_m e^{im\phi_t}\int dg\, e^{igy_t}H_m(ur_t)(b_{m\perp}\Psi_{gm\perp}^{\text{ext}} + b_{m\parallel}\Psi_{gm\parallel}^{ext}) \tag{3.46}$$

which one inserts into Eq. (3.44). Using the results from Eq. (3.14),Eq. (3.29), and Eq. (3.33), one can then express the energy loss in its final form,

$$\Gamma^{\text{loss}}(\omega) = \int dg\, S(g,\omega) \tag{3.47}$$

where

$$S(g,\omega) = \frac{1}{\pi}\sum_m Re\left\{\left(\frac{\beta^2\lambda^2}{2u^2}a_{m\perp} + \frac{i\beta g\lambda}{2u^2}a_{m\parallel} - \frac{i\beta g\lambda}{2u^2}b_{m\perp} - \frac{g^2}{2u^2}b_{m\parallel}\right)|\Psi_{gm}(\vec{x_0})|^2\right\} \tag{3.48}$$

and

$$|\Psi_{gm}(\vec{x_0})|^2 = \frac{4}{v^2}\frac{e^{-2b\lambda}}{\lambda^2}\left(\frac{\lambda+\omega/v}{u}\right)^{2m} \tag{3.49}$$

and $\beta = v/c$. It is instructive to see the energy-loss probability Γ^{loss} at the classical limit (i.e. c$\rightarrow\infty$), in which case $\beta\rightarrow 0$. The only term that survives from Eq. (3.48) is the fourth term. Likewise $u = u_a = ig$, which follows from $k\rightarrow 0$, and the bessel functions take the form of modified bessel functions as follows:

$$J_m(ua) \rightarrow i^m I_m(ga)$$

$$J'_m(ua) \rightarrow i^{m-1} I'_m(ga)$$

$$H_m(ua) \rightarrow \frac{2}{\pi} i^{-(m+1)} K_m(ga)$$

$$H'_m(ua) \rightarrow \frac{2}{\pi} i^{-(m+2)} K'_m(ga)$$

Using these identities, Eq. (3.41) can be rewritten as

$$b_{m\|} = (-1)^m \frac{i\pi}{2} \frac{\epsilon_a I'_m(ga) I_m(ga) - I'_m(ga) I_m(ga)}{I_m(ga) K'_m(ga) - \epsilon_a I'_m(ga) K_m(ga)} \tag{3.50}$$

The energy loss in the classical limit is then expressed as

$$\begin{aligned} \Gamma^{\text{loss}}(\omega) = \frac{1}{v^2} \sum_m Re \Bigg\{ \int dg \frac{i(\epsilon_a I'_m(ga) I_m(ga) - I'_m(ga) I_m(ga))}{I_m(ga) K'_m(ga) - \epsilon_a I'_m(ga) K_m(ga)} \\ \times \frac{\exp(-2b\sqrt{g^2 + (w/v)^2})}{g^2 + (w/v)^2} \left(\frac{\sqrt{g^2 + (w/v)^2} + w/v}{g} \right)^{2m} \Bigg\} \end{aligned} \tag{3.51}$$

which is equivalent to the Bertsch formalism [44] provided it undergoes a conversion to atomic units (i.e. $e = \hbar = 1$).

3.3 Waveguide Modes of GaN Nanowires

3.3.1 Experiment and Theory

Gallium nitride (GaN) is an attractive material for optoelectronics [53, 54] because its wide bandgap enables light emission in the ultraviolet-blue frequency range, and its high-index contrast with air results in strong mode-confinement. Single GaN nanowires have also been demonstrated as lasers [9], and have shown low lasing thresholds [55]. Fig. 3.2 shows the dielectric function for GaN in the energy range of 0.5 to 10 eV. The values were obtained from previously parameterized results [56]. The optical absorption coefficent of the material is very low below 3 eV. In this range, good optical transmissivity and no classical electron energy losses are predicted. Near the bandgap, at 3.5 eV, the imaginary

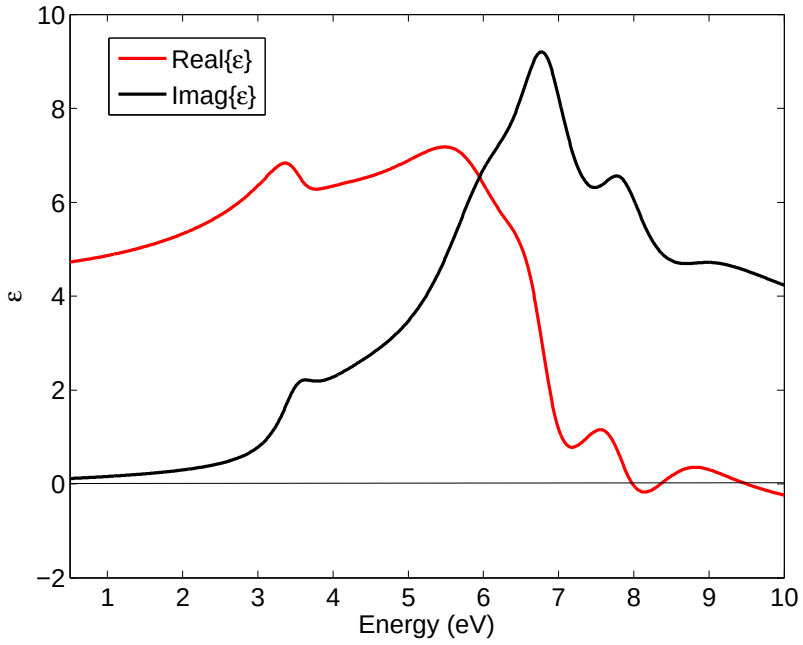

Figure 3.2: The dielectric function for GaN in the energy range of 0.5 to 10 eV. The imaginary component becomes negligible below 3 eV, near the optical bandgap onset.

component of the dielectric function rises rapidly, leading to strong absorption of light and a classical loss mechanism for swift electrons in the medium.

For this work, experiments were performed by I. Arslan and R. Erni on the Lawrence Livermore FEI Tecnai operated at 200 kV with an energy resolution of 300 meV and a spatial resolution of 1 nm. Single crystalline nanowires with hexagonal cross-sections were synthesized following a previously reported method [57](Fig. 3.3(a)). The lengths typically range between 3 to 5 μm, and the diameters range between 350 to 500 nm. The nanowires were then dispersed onto perforated silicon nitride films. To minimize any background signal, nanowires suspended across the holes in the films were investigated. The probe-sample orientation involved the electron beam normally incident to the cylindrical axis of the nanowire, but at a non-penetrating trajectory where the

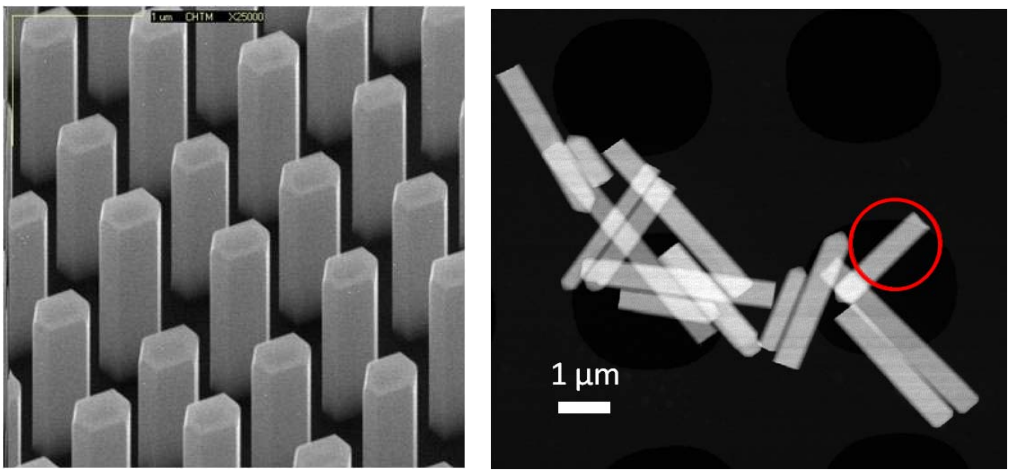

(a) (b)

Figure 3.3: (a) As grown hexagonal GaN nanowires. (b) HAADF-STEM image of GaN nanowires dispersed on SiN_x perforated TEM grid.

probe was placed at an impact parameter of 1 to 2 nm away from the surface of the nanowire (Fig. 3.3(b)). When the probe was placed too close to the nanowire, a small fraction of the probe profile would penetrate the rod and lose energy to bulk plasmon excitations. When the probe was kept outside the sample, the bulk plasmon signal was lost and only surface plasmon and radiative losses would be detected.

Modeling the hexagonal nanowire by a circular cylinder of equal cross-sectional area is a good approximation in the energy range of interest (see Fig. 3.4). Calculations were performed using the MIT photonic bands package [58], which relies on spatial discretization of the electromagnetic waves. The guided modes of the two geometries show close equivalence, especially near lower energies, with the eigenvalues of the equal area cylinder as a variational lower bound for the hexagonal cylinder and the eigenvalues of the inscribed cylinder as an upper bound [59].

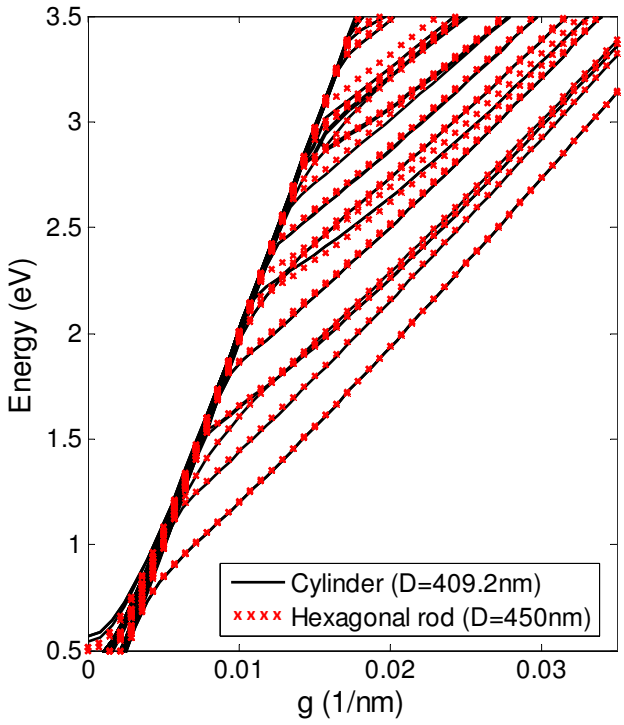

Figure 3.4: The waveguide modes of hexagonal nanowires and cylindrical nanowires with equal cross-sectional area. In the energy range of interest, the agreement between the two types of modes is good. Due to the size of the supercell, the artifacts are apparent below 0.6 eV.

The field of the fast electron was expanded into a set of vector cylindrical harmonics. Appropriate boundary conditions at the dielectric interface were solved for the 2×2 scattering matrix elements, from which the hybrid (HE_{mn}, EH_{mn}) and cylindrically symmetric transverse magnetic, transverse electric (TM_{0n}, TE_{0n}) modes can be generated. Here, the m describes the angular symmetry, and the n refers to the radial number. The hybrid modes refer to modes that support both electric and magnetic fields in the axial direction. The output is a dispersion map of electron energy loss probability S(g,E) described in Eq. (3.48) as a function of energy loss E and momentum transfer g. The eigenmodes of the system are apparent as strong energy loss peaks in the energy-versus-momentum dis-

persion map (Fig. 3.6). The momentum, corresponding to the axial propagation constant, g, is proportional to the probe-electron scattering angle. Integrating S(g,E) over all angles inside the collection aperture, then, yields the loss probability corresponding to the observable EELS profile.

3.3.2 The Electron Energy Loss Function

The particular nanowire investigated is indicated with the circle in Fig. 3.3(b), where the diameter, d, is 450 nm. Fig. 3.5 shows the EEL spectrum for an electron beam passing near the edge of the nanowire. A set of peaks are identified below the bandgap onset (3.5 eV) near 1.95, 2.4, 2.8 and 3.18 eV, respectively. The dotted blue curve represents the retarded calculation for a cylinder with equal cross-sectional area (d = 409.2 nm). To account for the tail from the incident, unscattered beam, a background model composed of a convolution between a Lorentzian and Gaussian was added to the calculation and fitted to the experiment by the least mean squares method. The resulting comparison between calculation and experiment shows good agreement, as the theory accounts for the four prominent peaks observed in the experiment.

To gain insight into the origin of the peaks, calculated energy-versus-momentum maps are presented in Fig. 3.6. Fig. 3.6(a) displays the waveguide modes numerically calculated using the MIT photonic-bands software [58] for a cylinder of equal cross-sectional area, and employing a frequency-independent, real dielectric constant, $\epsilon = 5.29$, characteristic of the bandgap of GaN. Given the high index contrast with vacuum and the large diameter, it is not surprising that a large number of guided modes are supported throughout the energy range of

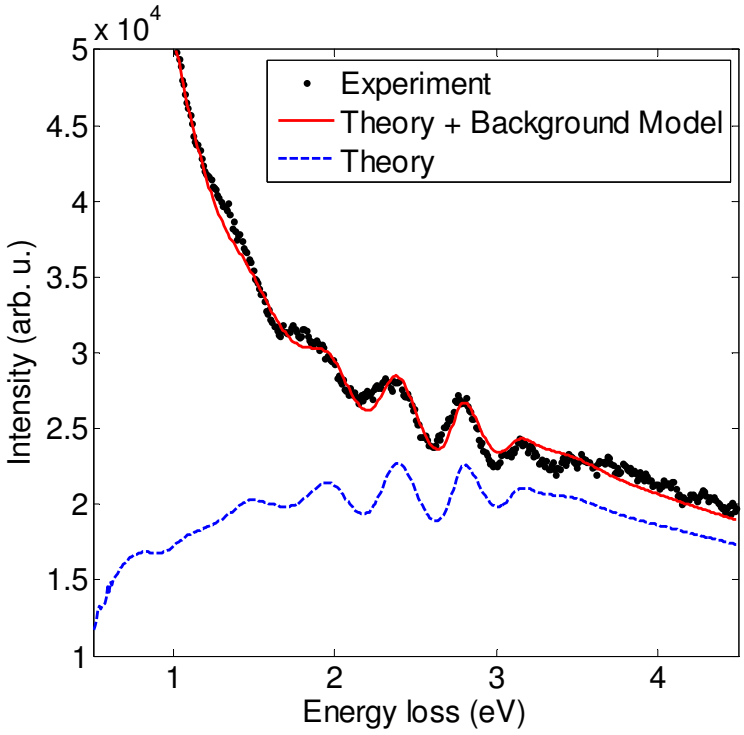

Figure 3.5: Experimental EELS recorded outside a 450 nm GaN nanowire, and theory for an equal cross-sectional area cylinder. Background tail was modeled as a convolution between a Lorentzian and Gaussian.

interest. The EEL dispersion map for the same system is analytically calculated and shown in Fig. 3.6(b). It is clear that the propagating waveguide modes observable in Fig. 3.6(a) are identically traced out by the field of the fast electron. Higher intensity signal within the light-line is generated from the coupling of the incident electron to the evanescent states of the nanowire. In particular, EH_{mn} hybrid waveguide modes (waveguide modes with a dominant axial electric field component) outside the light-line are shown to cross into inside the light-line, identifiable by a discontinuous transition from modes shown by blue to white intensity. Because these modes inside the light-line are evanescent in nature, energy is leaked at a rate determined by their finite life time. The EEL

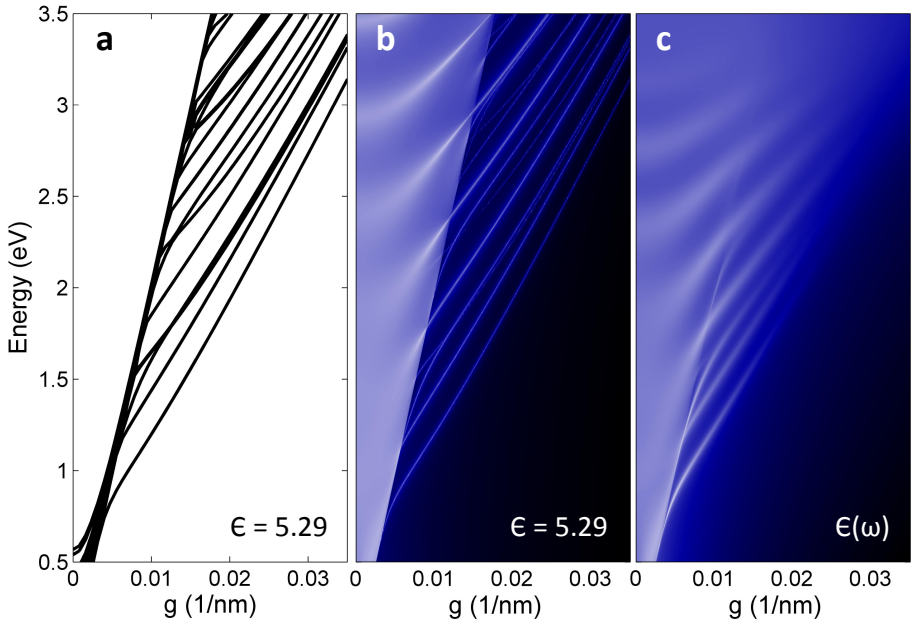

Figure 3.6: (a) Waveguide modes calculated using MIT photonic bands package using ϵ=5.29, a dielectric constant characteristic of the bandgap of GaN. (b) Calculations of waveguide modes traced out by a 200 keV fast electron near a nanowire of ϵ=5.29. (c) Calculations of waveguide modes traced out by a 200 keV fast electron near a nanowire carrying a frequency-dependent real and imaginary dielectric function, $\epsilon(\omega)$ for GaN.

dispersion map for the actual frequency-dependent dielectric constant of GaN is shown in Fig. 3.6(c). The non-trivial imaginary component and the energy dependence of the dielectric constant impact the dispersion map in several ways. The first observation is that the cutoff is no longer as well defined as in the case for a purely real dielectric constant. Instead, modes outside the "light-line" are seen to spread into inside the "light-line" in a smooth transition. This obscures the ability to characterize the modes as purely propagating or purely evanescent. However, for modes near g=0, where the light carries little or no axial propagating momentum, light is transiently bound to the cross-sectional edges of the nanowire, and takes the form of transverse whispering gallery modes.

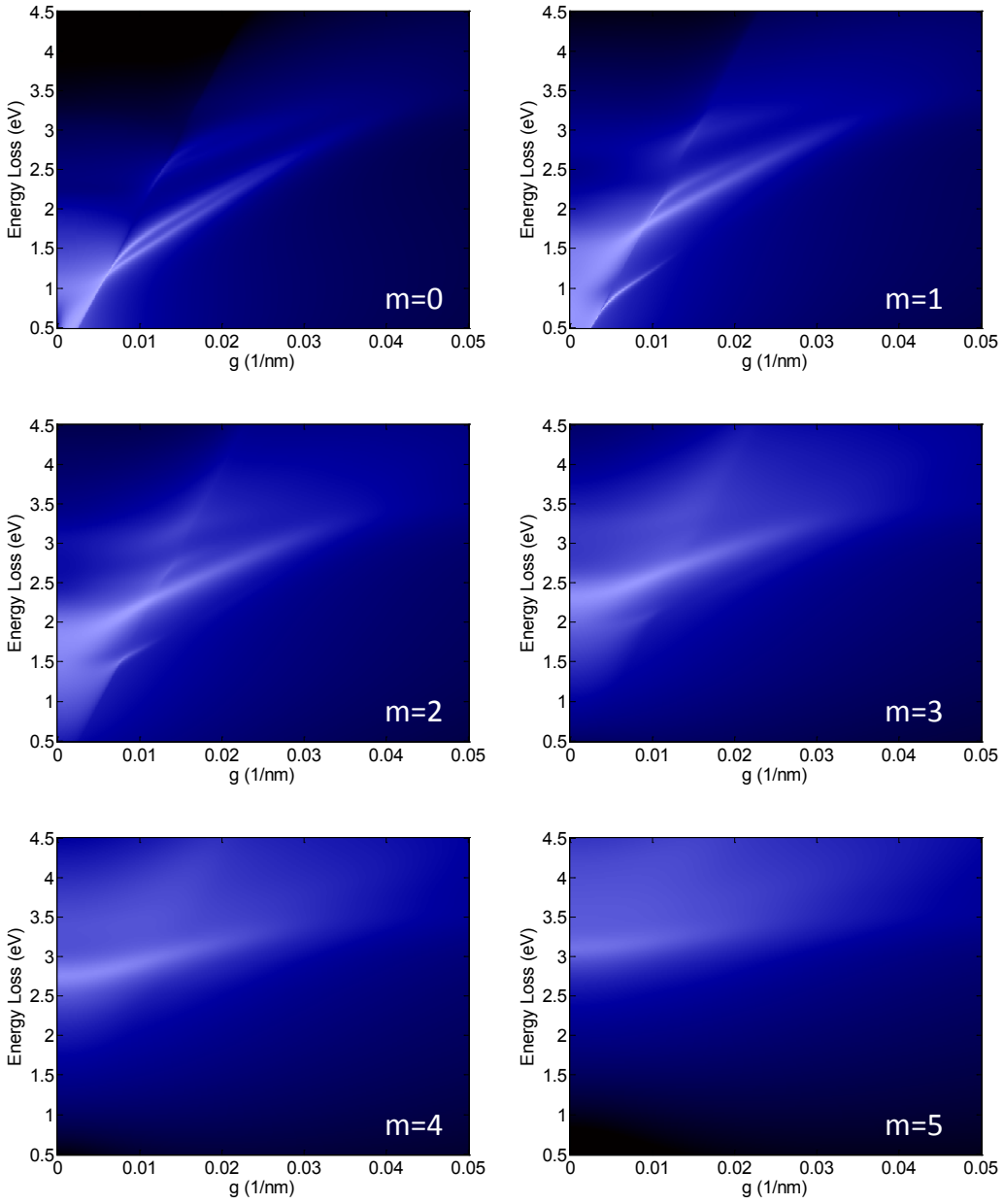

Figure 3.7: Dispersion from each azimuthal number, m, for a 409.2 nm cylindrical GaN nanowire.

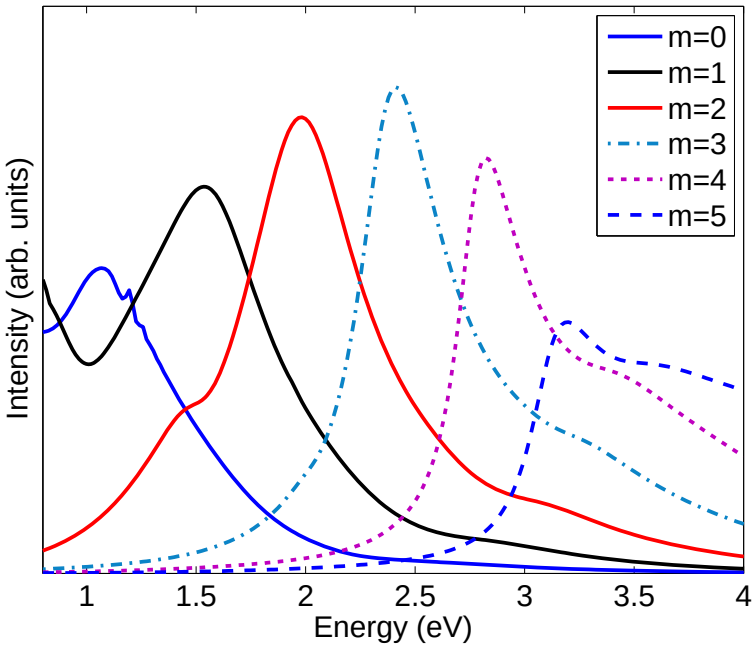

Figure 3.8: Contribution from each azimuthal number, m, to the energy-loss probabilities for an electron passing near a 409.2 nm cylindrical GaN nanowire.

Fig. 3.7 describes the dispersion of the energy loss for each azimuthal number, m. For m=0, the TE_{01} and TM_{01} modes are clearly visible with the TE_{01} mode being the lower energy mode. The TE_{02} and TM_{02} modes are also visible at higher energies with less intensity. For m=1, the HE_{11}, the EH_{11} and HE_{12} modes appear at increasing energies. For higher m's, the sharpness and intensity of the peaks deteriorates. From the m=2 map, the HE_{21}, EH_{21} and HE_{22} modes can be resolved, with the EH_{21} mode appearing the most strong in intensity. The EH_{21} also is shown to extend into the light cone. This trend continues for the m=3 map where the EH_{31} accounts for most of the energy loss. For m=4 and m=5, the HE modes are entirely damped, and intensity is dominant inside the light-cone.

Most of the intensity contributing to the peaks in Fig. 3.5 can be seen to orig-

inate from the EH_{mn} modes bordering on and extending into the "light-line". Fig. 3.8 shows the contribution of each m to the energy-loss probability. The four prominent peaks in Fig. 3.5 (at 1.95, 2.4, 2.8 and 3.18 eV) are shown to originate from the m=2,3,4, and 5 modes.

The increased imaginary component of the dielectric function at higher energies damps the modes both for increasing energy and momentum, clear signatures of attenuation. This also confines the scattering angles to a narrow spectrum. For the experiment, convergence was achieved for the range, $g < 0.035$ (1/nm). This corresponds to a scattering angle range under 87.5 μrad. The number of discernable waveguide modes has also decreased, with only few low order modes remaining. In particular, the three lowest-energy modes in Fig. 3.6(c) (identified as the HE_{11}, TM_{01} and TE_{01} modes) can be clearly resolved. At smaller diameters (120 nm), the HE_{11} mode has been reported to possibly participate in guiding the ultraviolet-blue wavelength (3.31 eV) [9, 60]. For the hexagonal diameter in consideration (d=450 nm), the HE_{11} mode is scaled down in energy and higher-order waveguide modes dominate at the ultraviolet-blue wavelength. These modes are resolvable in Fig. 3.6(c), albeit weakly due to the strong attenuation.

3.3.3 Discussion on the Formation Length

The energy loss mechanism responsible for the dispersion maps can be interpreted as similar in nature to transition radiation. Cherenkov radiation plays only a minor role for the diameters under consideration, as the characteristic dispersion maps can be obtained for electron velocities that do not satisfy the

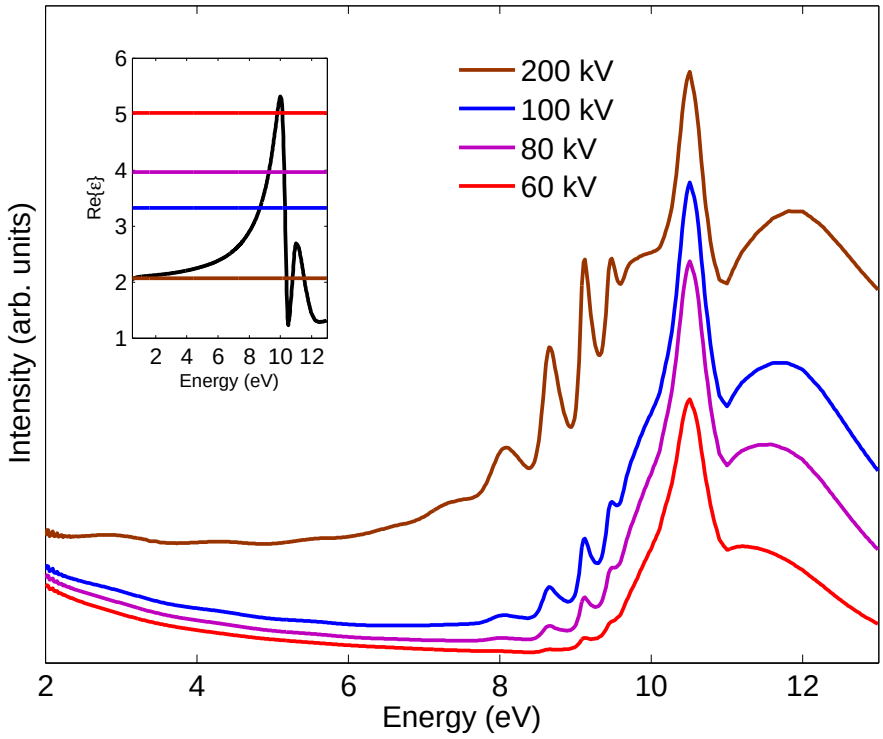

Figure 3.9: Energy loss probabilities at different beam voltages for a 260 nm diameter SiO_2 nanowire. The inset describes the real part of the dielectric function, and the corresponding cutoff conditions for Cherenkov radiation emission.

Cherenkov condition (i.e. $v > c/\mathrm{Re}\{\epsilon\}$). Fig. 3.9 shows the energy-loss probabilities for a 260 nm-diameter SiO_2 nanowire. The impact parameter is 1 nm away from the surface. The inset shows the real part of the dielectric function and the ϵ_{cf} for different electron voltages (see section 3.2.4). Although the peaks for lower beam energies are less pronounced than in the case of a SiO_2 nanosphere (Fig. 2.12), peaks are still resolved at conditions not satisfying the Cherenkov condition. For the 80 kV beam, Cherenkov radiation is emitted above ~9.3 eV. However peaks are resolved below this energy at 9.1 eV and 8.65 eV. At 60 kV, the peaks are poorly resolved. However, the dispersion map of the energy-loss at this beam energy demonstrates that the waveguide modes are in fact excited,

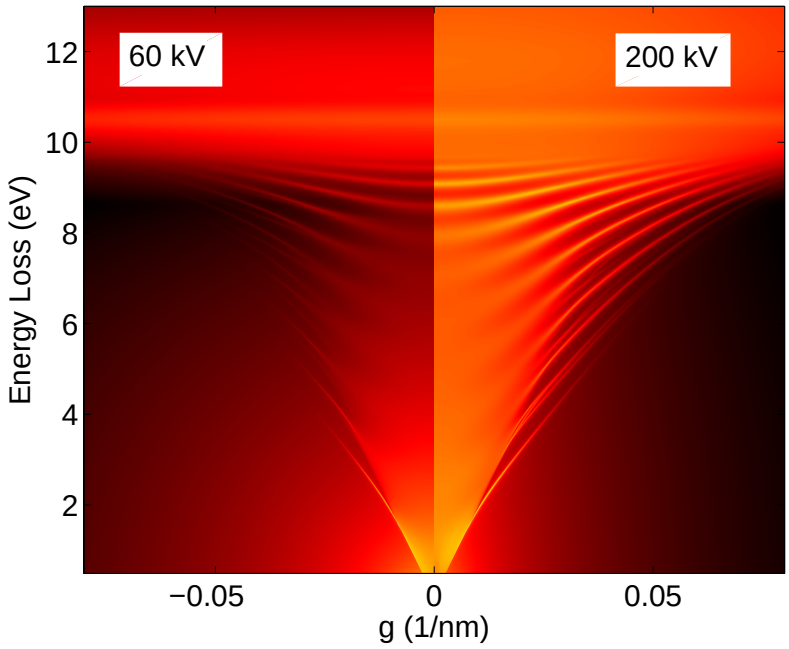

Figure 3.10: Dispersion maps of a 260 nm diameter SiO_2 sphere at 60 kV (left) and 200 kV (right). Cherenkov radiation does not account for the energy-losses at 60 kV as the Cherenkov condition is not satisfied.

albeit weakly (Fig. 3.10).

Transition radiation occurs for a fast electron traversing two separate mediums. Because the initial and final field distributions in each medium are different, the fields must rearrange as the particle traverses the boundary, and in the abrupt rearrangement radiation can be generated [12]. The formation time for a coherent radiative wave to fully develop must be at least one period. The formation length over which the wave develops defines the characteristic thickness at which the radiation can interfere coherently to yield a far-field response. For non-penetrating electron trajectories the electron itself remains in vacuum and does not cross into a different medium. However, the retarded fields of the electron experience an abrupt change in their distribution as they cross from vac-

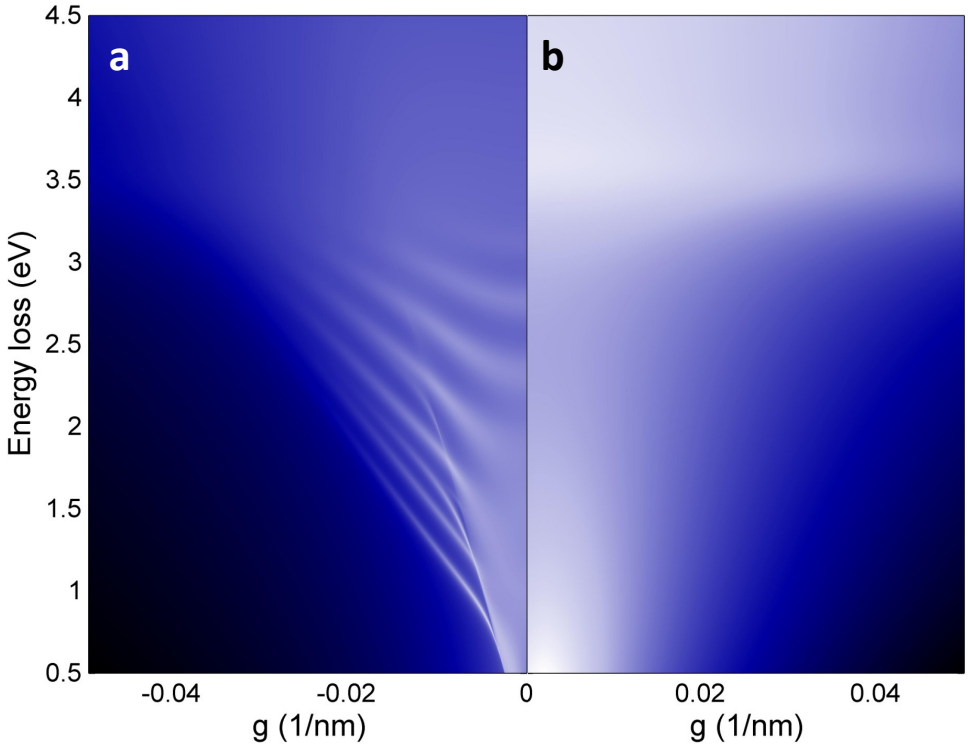

Figure 3.11: The dispersion map for the electron energy loss calculated for a 200 keV electron passing near a 409.2 nm diameter GaN cylinder. Comparison of (a) The full relativistic calculation and (b) the non-relativistic calculation (intensity scaled up by a factor of 10), shows the absence of energy loss to photonic states in the non-relativistic case.

uum into the dielectric material, and this change again produces radiation. The inherently near-field behavior can transition into far-field radiation when the coherence conditions determined by the geometry and characteristic size of the nanowire are satisfied. For diameters less than the formation length, the coherence condition becomes increasingly difficult to satisfy. The longer wavelength radiative modes become suppressed and the retarded calculation approaches that of the classical formalism where relativistic effects are neglected and no radiative modes are predicted. Likewise, calculations for diameters on the order

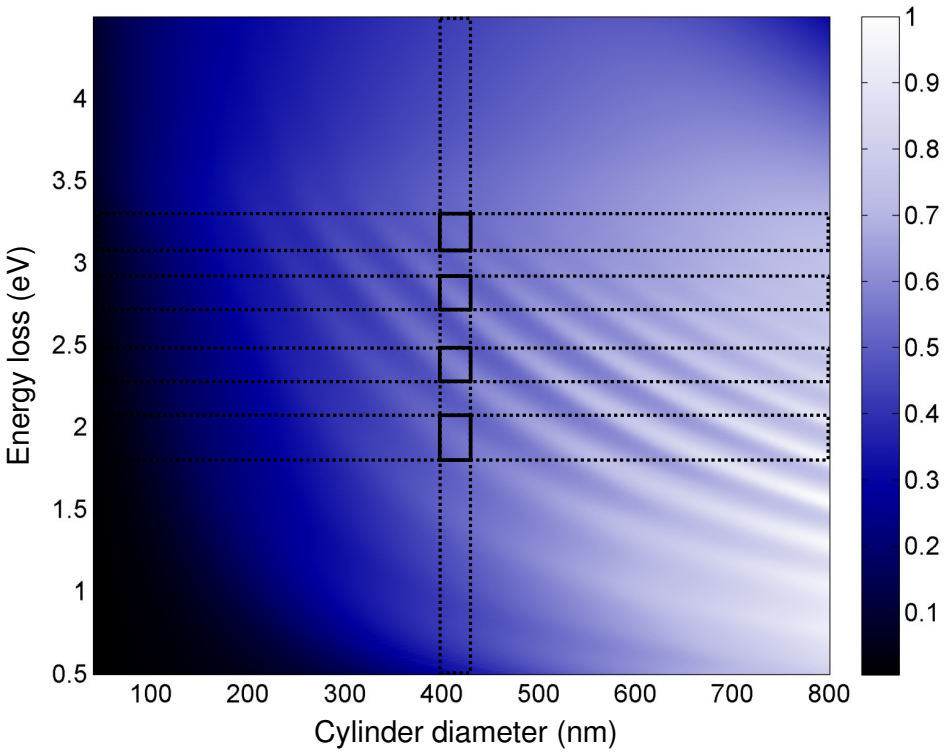

Figure 3.12: Energy loss probabilities as a function of cylinder diameter. The horizontal boxes indicate the four prominent peaks from the EELS experiment on the 450 nm diameter GaN nanowire (converted to the diameter of a equal cross-sectional area cylinder).

of the light-emission modes show a clear departure from the classical formalism (Fig. 3.11).

Fig. 3.12 shows the EEL map for different diameters in the range from 50 to 800 nm. At larger diameters the number of peaks increases and the contrast improves. The peak-to-peak distances energies scale roughly inversely with diameter within the region of negligible inelastic interactions (i.e. below the bandgap where $\mathrm{Im}\{-1/\epsilon\} \sim 0$). Peaks at smaller diameters are poorly defined, and below 100 nm no peaks are resolved. As the HE_{11} does not have a cutoff and each

peak in the map originates from intensity due to EH_{mn} modes crossing the cut-off into the light-cone, the map provides a upper limit for diameters for which single-mode (HE_{11}) behavior can dominate (namely, the dark region below d $\sim$ 100 nm). The number and position of the peaks in the energy loss spectrum provides an independent check on the diameter of the GaN nanowire. Measurements of the width of the nanowire by elastic-scattering contrast from STEM images contain a 3-4% uncertainty in the scan calibration, typically associated with the re-alignment of electron optics in order to operate in the monochromated mode of the microscope. Fig. 3.12 shows the bounds on the size of the nanowire given by both EELS and elastic STEM imaging.

The natural modes of the rod can extend throughout the sample showing nodes, antinodes and an evanescent decay into the surrounding free space. The spatial resolution of EELS to excite natural modes from the near-field excitation by the swift electron can be estimated from Bohr's adiabatic criterion for the delocalization length (i.e., $b_{\max} \sim v/\omega$) [13, 61], and describes the spatial extent of the electron's "reach" for efficient energy transfer to the sample. The excitation of transverse whispering gallery modes and propagating waveguide modes by a fast electron near the nanowire implies that energy transferred from the electron can then couple throughout the structure, provided the coherence condition set by the formation length is met. The result is a very high resolution map of the spatial variation of photonic density of states of the rod.

3.4 Waveguide Modes of Germanium Nanowires

3.4.1 Experiment and Theory

Samples were prepared for nanowire growth by depositing gold nanoparticles using a process previously reported by Woodruff *et al.* [62]. Silicon substrates were briefly etched in dilute HF (< 2%) in order to remove the native oxide. One part dilute HF was then added to nine parts of 200 nm gold nanoparticle solution (Ted Pella) and the resultant mixture was then placed onto the substrate. After being blown dry under N_2 samples were immediately transferred to a tube reactor chemical vapor deposition system and heated to growth temperature under argon flow. Growths were performed for 12 minutes at 320 C and a constant pressure of 200 Torr. Germane (1.46% in hydrogen) was used as the source gas and was further diluted in hydrogen in order to maintain a partial pressure of 2.34 Torr. Samples were subsequently annealed under 30 Torr of hydrogen at the growth temperature for 10 minutes and then cooled under vacuum. Figure 3.13(a) shows the as-grown nanowires on a silicon wafer. The nanowires were sonicated in methanol (MeOH), and dispersed onto a SiN_x TEM grid containing an array of 50 μm-size perforated holes (Ted Pella Inc) (see Fig. 3.13(b)). Annular dark field (ADF) imaging and EELS measurements of the nanowires was performed on a 200 kV FEI Tecnai F20-ST STEM equipped with a Gatan imaging filter 865-ER. The convergence and collection semi-angle were 8 mrad and 12.5 mrad, respectively. The size of the focused probe was around 2 nm. The electrons were filtered through a Wien-filter monochromator, enabling an enhancement in the energy resolution, measured at 130 meV. Long acquisition times for high signal-to-noise ratios were preferable. However, fluctuations

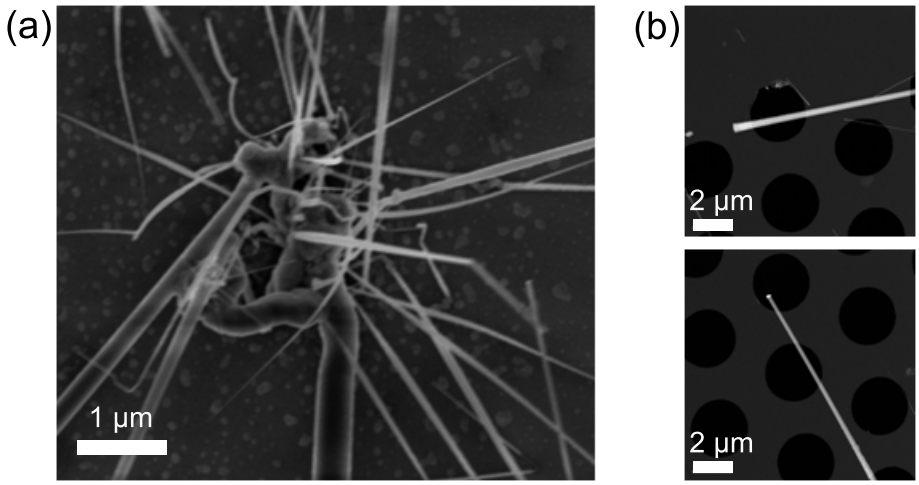

Figure 3.13: (a) SEM image of Ge wires grown on a Si substrate. (b) High angle annular dark field STEM images of individual Ge nanowires dispersed on perforated SiN_x films.

in the high tension voltage could be as large as 100 meV. Therefore, in order to minimize the degradation of energy resolution due to the instabilities, a series of spectra including the full ZLP were acquired at short acquisition times (0.1 sec) after which the spectra were aligned through cross-correlations and summed. This method generates sufficient statistics for analysis and allows for the identification of the peak energies with respect to the ZLP.

Ge nanowires suspended across holes in the grid were investigated, where the probe was stationed ~3 nm away from the surface of the nanowire and sufficiently distanced from the edge of the SiN_x perforated support.

The mono-crystallinity of the Ge nanowires restrict their cross-sectional geometries to hexagons or octagons instead of a circle. As in the case for the GaN nanowires, the eigenmodes of the equal-area cylinder set a variational lower bound for the hexagonal cylinder while the eigenmodes of the inscribed cylinder set an upper bound [59].

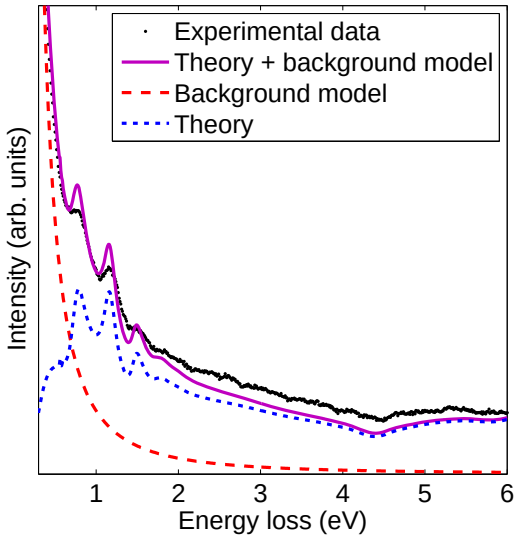

Figure 3.14: Experimental and simulated EELS for a 286 nm-diameter nanowire. A fitted background model (dashed curve) is added to the theory (short dashed curve) resulting in the solid curve which agrees well with the experiment (dotted curve).

In order to account for the tail of the ZLP, a background model consisting of a convolution between a Lorentzian and Gaussian was added to the theory and fitted to the original data through the least-mean-squared method. Figure 3.14 shows the original data for a 286 nm diameter nanowire, and the fitted theory including the background model.

The frequency-dependent Ge dielectric function was extracted from Philipp and Taft [63]. The function is characterized by a vanishing imaginary component and a large, real component below 2 eV (see Fig. 3.15), indicating minimal absorption and good transmissivity. Near 2 eV, the imaginary component rises rapidly, and at 4.44 eV a peak value corresponding to an interband transition is reached.

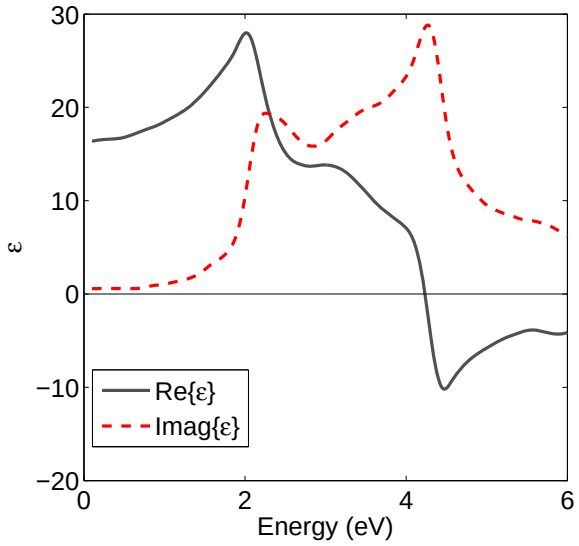

Figure 3.15: Real and imaginary components of the dielectric function for Ge. The imaginary component decreases to zero below 2 eV indicating negligible optical absorption in this regime.

3.4.2 The Electron Energy Loss

Figure 3.16 shows background-subtracted EELS from nanowires of 286 and 47 nm diameters, and the corresponding calculations. The electron trajectory for all cases is set to be 3 nm away from the surface. Good agreement between experimental data and dielectric theory is demonstrated. The spectrum from the 286 nm-diameter wire shows three prominent peaks below 2 eV, located at 0.7, 1.16 and 1.5 eV. Discrepancy in the peak sharpness between calculation and experiment may be attributed to surface roughness or interface states. In both cases, finite absorption results in a slight damping of the peaks. Above 4.44 eV, a edge onset is observable for both theory and experiment, indicative of energy loss to the interband transition. For the 47 nm-diameter wire, the spectrum consists of less intensity relative to the 286-nm diameter wire, and shows an absence of peaks below 2 eV.

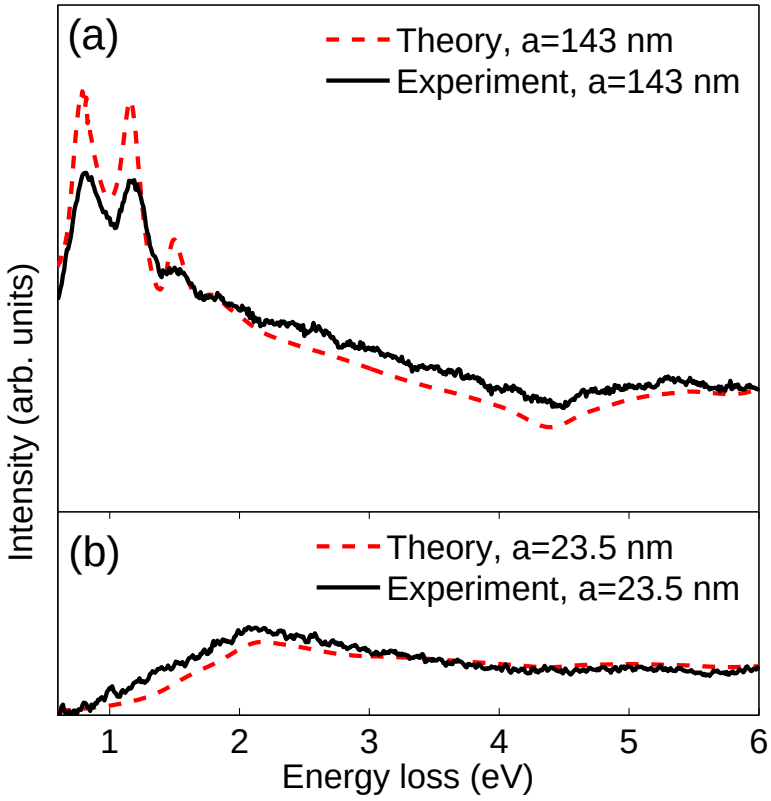

Figure 3.16: Background subtracted EEL for 143 and 23.5 nm-radius (or 286 and 47 nm-diameter) wires and the corresponding theory. The fitted background model is subtracted from the raw spectrum. (a) The first three theoretical peaks (dashed curve) in the 286 nm-diameter wire are resolved by experiment (solid curve). (b) The absence of the peaks are shown for the 47 nm-diameter wire for both theory (dashed curve) and experiment (solid curve).

Figure 3.17 provides insight into the origin of the spectra by displaying the dispersion map of the energy loss, described by $S(g,\omega)$ in Eq. (3.48). Intensity is plotted on a log scale. The interpretation is similar to the case for the GaN nanowires. For the 286 nm-diameter wire, the map traces out the optical waveguide modes, characterized by the cylindrically symmetric modes (TM_{0n} and TE_{0n}) and hybrid (HE_{mn},EH_{mn}) modes. All modes have cutoffs except for the HE_{11} mode. Intensity within and outside the light-cone is observed, show-

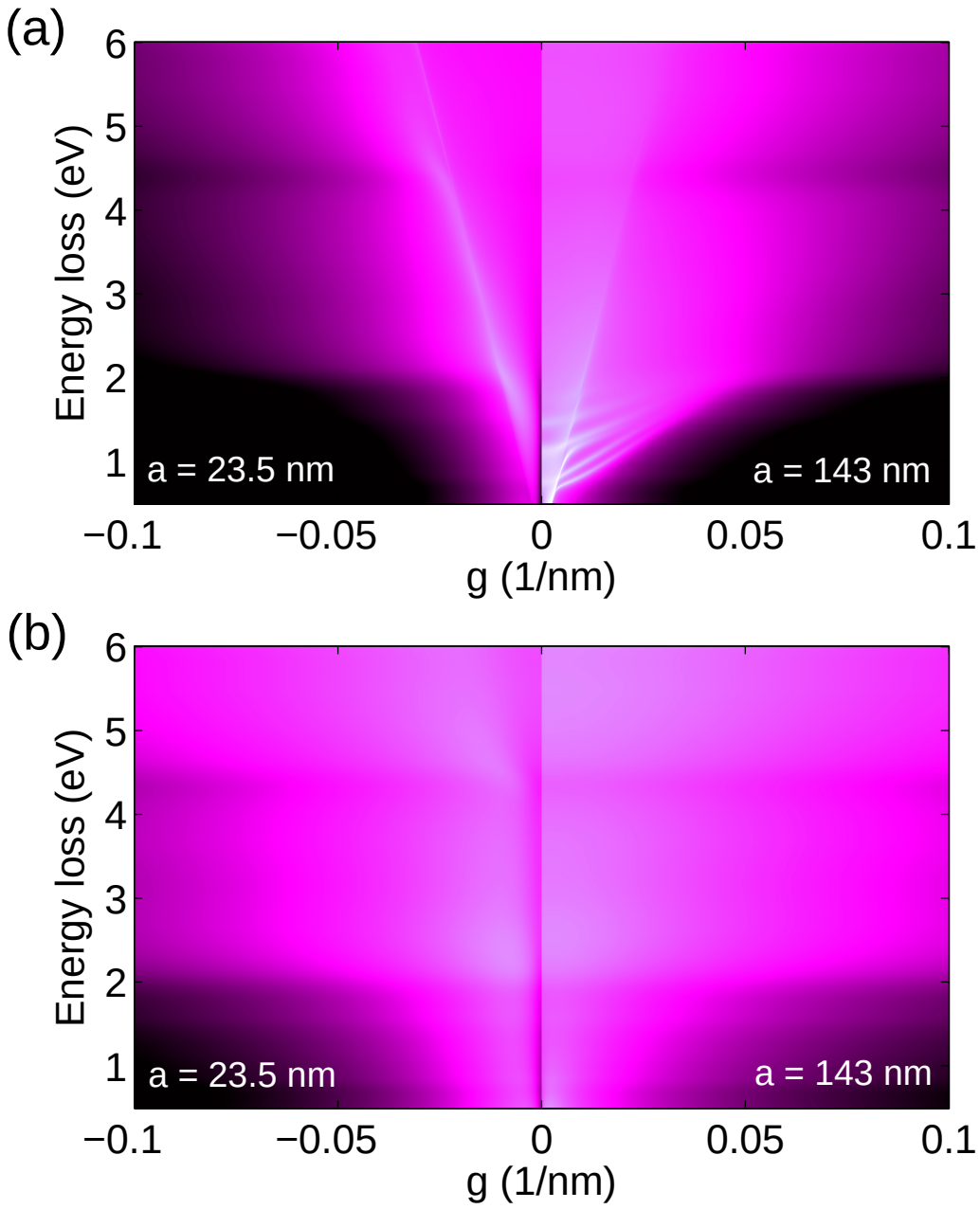

Figure 3.17: (a) Loss-dispersion map generated from $S(g,\omega)$ for 23.5 and 143 nm-radius (or 47 and 286 nm-diameter) wires. (b) The corresponding classical loss-dispersion map. Intensity is multiplied by ten for similar contrast. The impact parameter in all cases is 3 nm away from the surface.

ing that the field of the electron couples both to the evanescent and propagating modes. In particular, near g=0 all terms in Eq. (3.48) vanish except for the first term involving $a_{m\perp}$. In such a case, the modes carry little or no axial momentum and are closely related to the transverse whispering gallery modes whose field distribution is concentrated towards the outer rim of the nanowire. These modes gain momentum by crossing over the light-line where they transition into the form of longitudinal propagating modes. The non-zero imaginary dielectric component results in a smooth transition of modes crossing the light-line. Above 2 eV and for higher momentum values, the modes are dampened also because of the increased imaginary dielectric component.

For the 47 nm-diameter, the nanowire does not support multiple modes. The nanowire acts as a zero-mode waveguide as the lowest order HE_{11} mode is scaled to higher energies where damping is severe. Weak intensity inside the light-cone shows that radiative effects are less pronounced than for the 286 nm-diameter wire. This can be explained in terms of the formation criterion, where the formation time for coherent radiation to develop must be at least one period. Likewise, the formation length would depend on the characteristic length scale of the target. In the case of the nanowire, the diameter sets the formation criterion. A standing wave in the bandgap is increasingly difficult to form as the diameter of the wire shrinks, inhibiting radiative losses in the light-cone.

For comparison with the relativistic cases the classical loss maps for both diameters are shown in Figure 3.17(b). The intensity was scaled up by a factor of 10 for comparable contrast with Figure 3.17(a). The classical loss-dispersion maps for both diameters are similar, but both are strikingly different compared to the relativistic case in Figure 3.17(a). Even for the 47 nm diameter-wire which

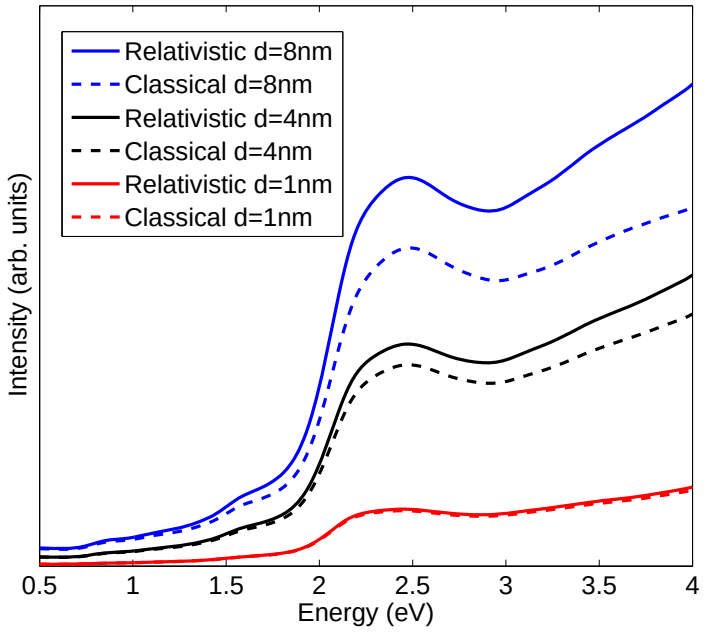

(a)

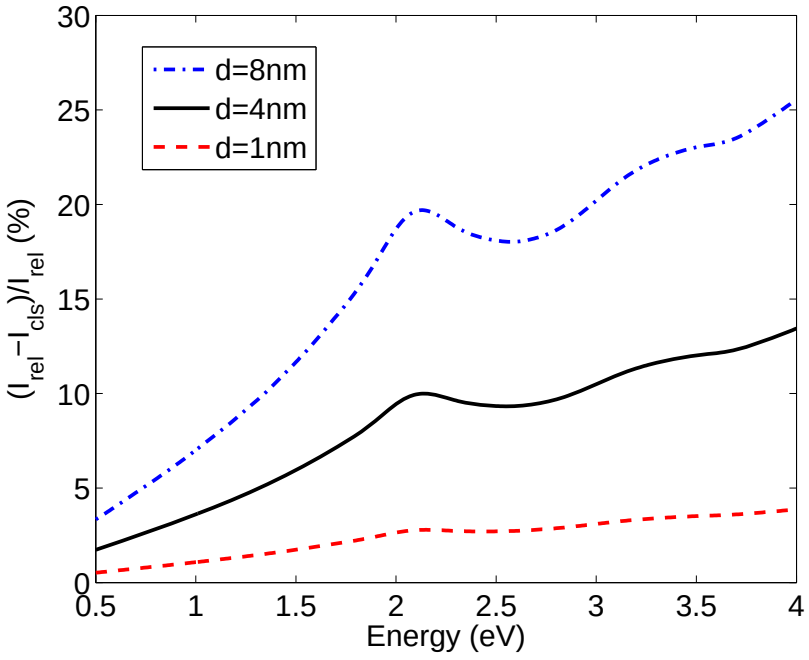

(b)

Figure 3.18: (a) Comparison between relativistic (solid curves) and classical (dashed lines) energy loss probabilities for 1 nm, 4nm and 8nm Ge nanowires. The beam voltage is 200 kV. (b) The percent change between relativistic and classical loss probabilities.

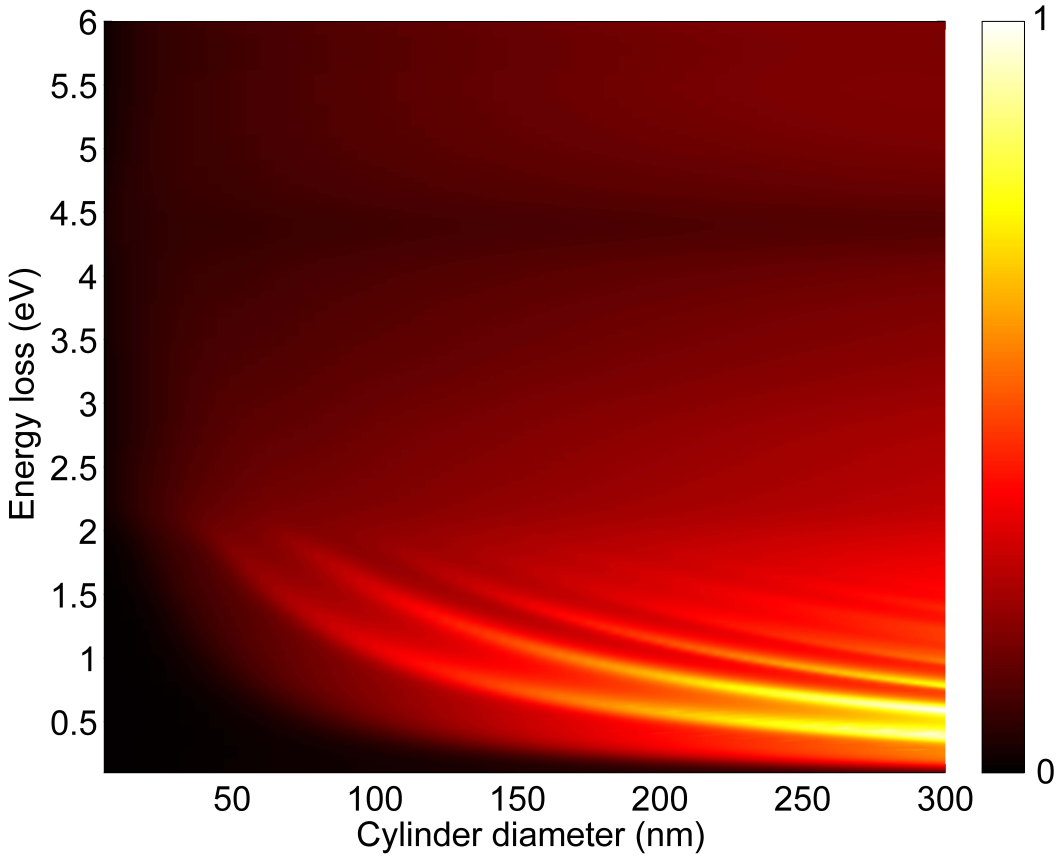

Figure 3.19: The energy-loss probability integrated over g as a function of diameter. Larger diameters are shown to support a higher density of peaks with improved definition. The increase in intensity above 4.44 eV is indicative of absorption due to the Ge interband transition. The intensities are normalized.

does not support any modes, the classical map fails to describe any of the characteristic features. Calculations show that for the Ge dielectric function, the classical formalism coincides with the relativistic formalism for diameters less than ~1 nm (Fig. 3.18(a)). A large scattering angle range was used for proper convergence ($0 < g < 0.7\text{nm}^{-1}$) for both formalisms. For slightly larger diameters, although the classical formalism reflects the features of the relativistic formalism, the intensities are different. In the energy range of interest, the relativistic pro-

file shows a higher probability than the classical. For example a 4 nm-diameter Ge wire exhibits a ~10% difference in its first peak intensity (Fig. 3.18(b)). This difference also increases for higher energies. In the size range where both formalisms coincide, caution is necessary in the use of a continuum medium theory as proper consideration of quantum mechanical effects may be necessary.

Figure 3.19 describes the relativistic energy-loss probability integrated over g for nanowire diameters up to 600 nm. For increasing diameter, a higher density of peaks are supported with enhanced sharpness below 2 eV. Peaks are no longer resolved below diameters of ~100 nm. Consequently, any single-mode (HE_{11}) or zero-mode behavior would have to arise for nanowires of diameters less than this size, since the single-mode itself does not contribute to the peak intensity when integrated over momentum, g.

CHAPTER 4

COUPLING EFFECTS IN NANOWIRE METALLODIELECTRIC CORE-SHELL SYSTEMS

Many interesting optoelectronic devices incorporating nanowires often use core-shell structures. For example, radial heterostructures are necessary for efficient charge injection into nanowire lasers. Solar-cells use radial pn-junctions to generate photocurrent [64]. Here, this section focuses on core-shell metallodielectric nanowires which have gained substantial attention due to their interesting optical properties. The formalism is an extension of the solid nanowire case, and therefore can apply to any dielectric function, whether it be metallic or semiconducting. Metallodielectric systems offer the intriguing ability to tune the surface plasmon resonance [65]. This has allowed the system to be applied to a range of biological and photonic devices [66]. A simple intuitive picture explaining the dipolar surface plasmon resonances due to the interaction of the inner and outer shell surfaces was developed by Prodan *et al.* [1] in the dipole limit. The evolution of optical fields inside larger diameters were also studied by Penninkhof *et al.* [67].

Core-shell metallodielectric nanowires are particularly relevant to photon scanning tunneling microscopy (PSTM), where a metal coated tip collects light close to the sample [68, 69]. Improved detection of fields can be achieved by understanding the dependence of diameter on the coupling between the surface plasmon polaritons and the dielectric propagating modes. Furthermore, due to their dispersion characteristics, surface plasmons are able to squeeze light into dimensions less than the diffraction limit [70, 71], allowing nanoscale lasers to undergo further miniaturization [72]. The qualitative behavior of the dipolar

plasmon resonances, the effect of different dielectric cores, and the interaction between the dielectric waveguide mode and surface plasmon are demonstrated from electron energy loss.

4.1 The Hybridization Model

A simple and intuitive model for surface plasmon behavior in shell structures can be thought of in terms of hybridization picture proposed by Prodan *et al.* [1]. The model was developed in the dipole limit where the size of the target is small compared to light wavelength, and therefore retardation is neglected. Nonetheless the model provides qualitative understanding and general predictions for the behavior of surface plasmons. The dipolar surface plasmonic modes that arise from a shell structure can be understood in terms of the hybridization between a cavity plasmon and a solid plasmon. Fig. 4.1 illustrates this idea for spheres, but is general to other geometries. The interaction results in the creation of two energy states corresponding to different charge polarizations across the shell structure. The higher energy state results from an antisymmetric charge polarization distribution, while the lower energy state results from a symmetric charge distribution. Because the cavity plasmon carries a higher energy than the sphere plasmon, the antisymmetric mode involves a larger contribution from the cavity plasmon. Likewise, the symmetric mode involves a larger contribution from the sphere plasmon.

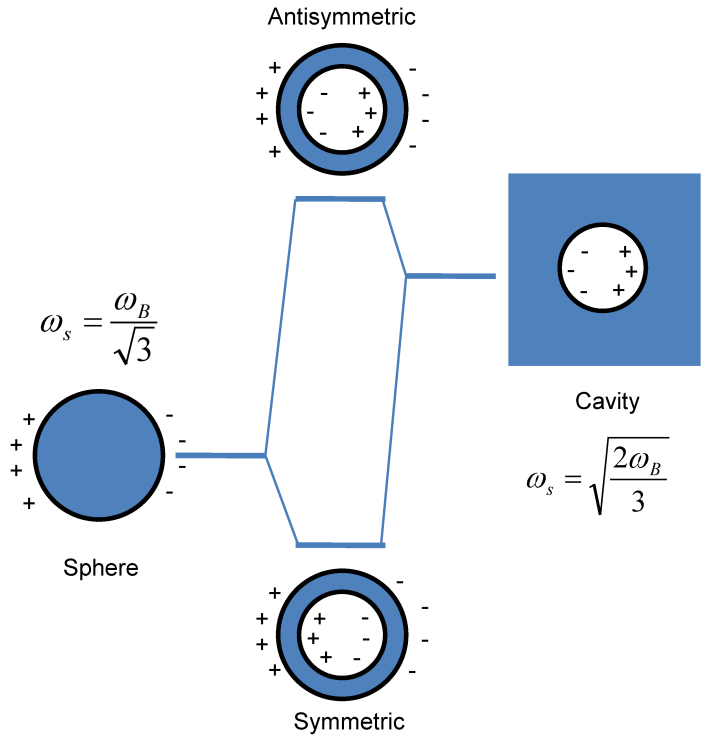

Figure 4.1: A hybridization model for a metallic sphere in the dipole limit (l=1). The coupling between the sphere mode and the cavity mode creates an antisymmetric and symmetric mode. Reproduced from Ref. [1].

4.2 Coupling of Surface Plasmons to Propagating Modes

The case where the electron again travels perpendicular to the cylindrical axis and passes close to the outer surface of the shell is considered. The difference between the loss-dispersion for a solid and shell wire composed of Au is first analyzed. Both wires share outer diameters of 140 nm, and for the shell case, an inner diameter of 130 nm is considered. The fast electron trajectory passes 1 nm away from the outer surface. A realistic dielectric function for Au, was interpolated from results by Johnson and Christy [2]. In the energy range of consideration (1<E<3.5 eV) this dielectric function differs from a simple Drude

model in that the imaginary component does not asymptotically approach zero, but instead rises to a finite value above ~2 eV, resulting in absorption losses. The solid nanowire exhibits surface plasmon modes described by the m=0 mode and a faintly visible m=1 mode. Here, the m=1 mode is severely damped by the non-zero imaginary component of the dielectric function For the Au shell, a drastic difference is observed in the dispersion of the surface plasmon modes. The field of the fast electron excites both inner and outer surface plasmon modes which, at sufficient thicknesses, are allowed to interact to generate a splitting of each mode into two branches. The dispersion map for the shell shows three clear modes below 2 eV which originate from the symmetric branches of the m=0, m=1, and m=2 modes. The antisymmetric branches would be supported at energies higher than 2 eV, but are damped out by the absorption losses in that region. Relative to the solid nanowire, the shell nanowire also supports more loss intensity inside the light-cone, where the symmetric branches of the m=1 and m=2 modes contribute predominantly.

Figure 4.2(b) shows the electron energy-loss probabilities for different shell thicknesses. In each case, the outer diameter is fixed at 140 nm while the inner diameter is varied. Starting from the solid nanowire, the single peak near 2.5 eV increases in intensity, and splits into two peaks with wider energy separations as the shell grows thinner. In addition, the maximum intensity is red-shifted. There exists the possibility of interpreting the two peaks as the result of anti-symmetric and symmetric modes at first glance, but from Figure 4.2(a), it is understood that they originate from the lower-energy (or symmetric) branches of the m=1 and m=2 modes. It is interesting to note a sharp transition at the light-line for the symmetric m=1 mode. As the shell thickness increases, the field of the fast electron is increasingly shielded from the inner surface, while

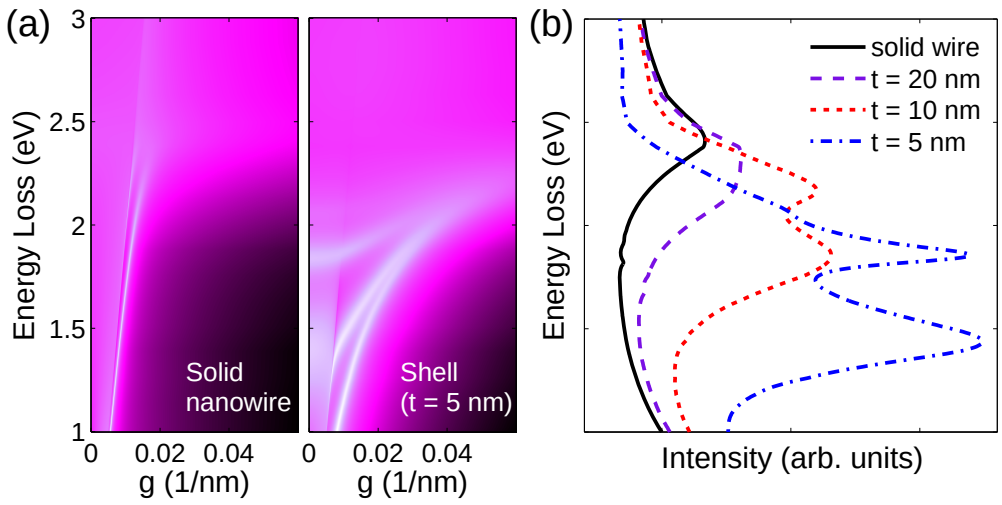

Figure 4.2: (a) loss-dispersion map for a solid 140 nm-diameter Au nanowire and for a Au shell consisting of an inner and outer diameter of 130 and 140 nm, respectively. The first three modes are due to the lower-energy (or symmetric) branches of the surface plasmonic modes. (b) EELS for different shell thicknesses with the outer-diameter fixed at 140 nm. The splitting of the peak originates from the m=1 and m=2 symmetric modes. Intensity is enhanced for thinner shells as the electron field couples more efficiently to the inner shell.

the coupling strength weakens due to the increased separation between inner and outer surfaces. An enhanced loss intensity for thin shells results from the ability of the electron to efficiently excite the inner and outer surfaces, and the stronger coupling between the two surfaces.

The influence of a dielectric core is illustrated in Figure 4.3. Here, two different dielectrics, which exhibit a wide optical bandgap so that loss interference due to absorption can be avoided, are used. SiO_2 and GaN both provide negligible imaginary dielectric components in the energy range of interest. The inner diameter of the shell is 160 nm, the outer diameter is 200 nm, and the fast electron travels 1 nm away from the outer surface. For a shell consisting of vacuum, no apparent splitting is observable from the loss profile. Similar to the t=20 nm

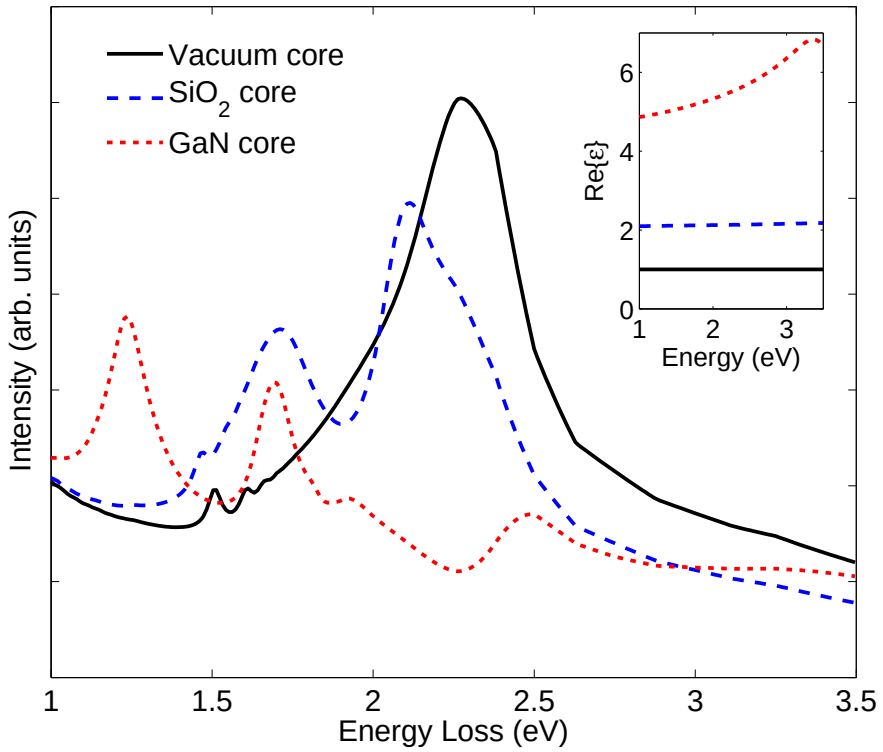

Figure 4.3: EELS for a Au shell consisting of an inner and outer diameter of 160 and 200 nm, respectively. Different dielectric cores result in the shifting and splitting of energies depending on their dielectric constant. The inset shows only the real part of the dielectric constants for SiO_2 and GaN as the imaginary component is small in the energy range of consideration ($1 < E < 3.5eV$).

case in Figure 4.2, the shell thickness effectively shields the penetrating electric field from exciting the inner surface plasmons. However, for a shell of the same thickness, inclusion of a dielectric core alters the behavior of the loss profile drastically through the introduction of energy shifts and splitting of peaks. The splitting of the surface plasmons modes for a shell can be qualitatively interpreted as the result of a hybridization between surface plasmons of a solid cylinder in vacuum and a cylindrical cavity in an infinite metallic medium. When a dielectric with a high index fills the cavity, less energy is required to excite the

plasmons on its surface [73]. This red-shift of the cavity surface plasmon energy causes an overall lowering of the hybridized mode energies of the core-shell system. From Bohr's adiabatic criterion (b$\sim v/\omega$), which estimates the impact parameter required to couple to an excitation, ω, the lowering of energies allows the same impact parameter to excite the surface plasmon more efficiently. The inset in Figure 4.3 describes the real part of the dielectric function for vacuum, SiO_2 and GaN cores, respectively. For higher values of the real dielectric constant, the general collection of peaks are shifted to lower energies. Figure 4.4 illustrates this behavior more clearly through the loss-dispersion map, where the lower-order modes are increasingly pushed down in energy for dielectrics carrying a higher index. For the GaN core, the symmetric-branches of the m=0, m=1 and m=2 modes can be resolved. The antisymmetric branch of the m=0 mode is faintly visible near 2.5 eV, and shows a dispersion characteristics near the light-line.

As a simple illustration, a Drude model for Au is considered, where above 2 eV, the imaginary component of the dielectric function asymptotically approaches zero. A 160 nm-diameter GaN core surrounded by a 5 nm thick shell of Au whose dielectric function can be described by [67] is considered.

$$\epsilon_{\mathrm{Au}}(\omega) = \epsilon_{\mathrm{d}} - \frac{\omega_p^2}{\omega^2 + i\,\omega\gamma_d} \tag{4.1}$$

where ϵ_{d}=9.54, ω_p=8.5566 eV and the damping factor γ_d=0.0823 eV. A comparison of the dielectric function between the Drude model and the experimental (from Ref.[2]) is shown in Fig. 4.5. For the most part, the Drude model follows the experimental results, but above 2 eV the imaginary components fails to describe the rise in absorption.

The impact parameter is 1 nm away from the surface of the outer shell. Only

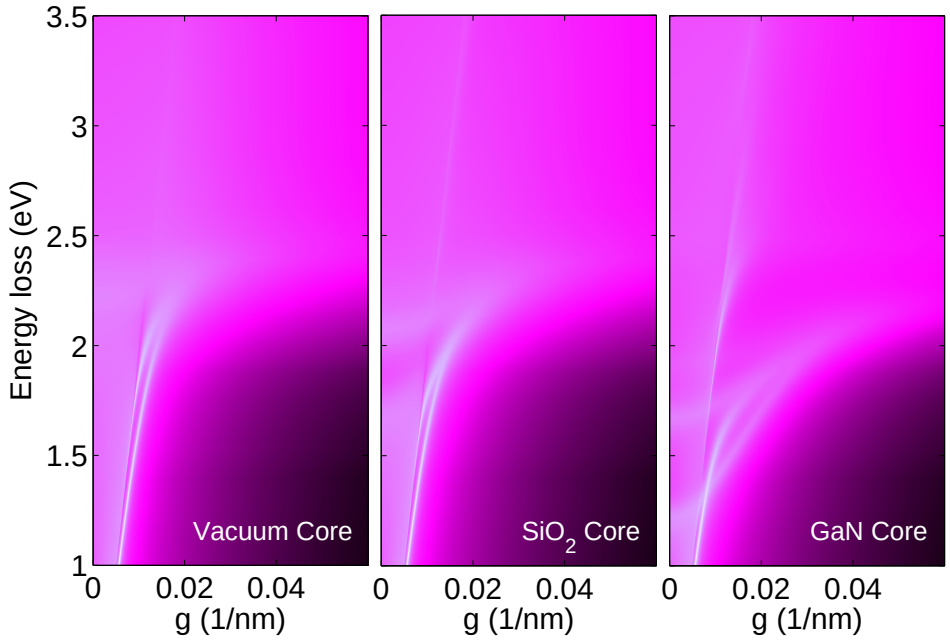

Figure 4.4: The loss-dispersion map for the same system considered in Figure (4.3). The gradual red-shift of the antisymmetric modes occurs for higher dielectric constants.

the m=1 modes of the system are considered for simplicity. Figure 4.6 shows the m=1 loss-dispersion for a GaN core, a Drude-model Au shell, and the combined core-shell system. The impact parameter for the solid core is 6 nm away from its surface. For the case of a Au shell with a vacuum core, the loss-dispersion map shows the splitting of the m=1 mode into its symmetric and antisymmetric branches, where the antisymmetric branch was previously damped out using a realistic dielectric function for Au. Because the symmetric mode is largely influenced by the sphere-like state, which couples more efficiently to the incoming field than the cavity-like state, the symmetric mode appears with a higher loss intensity than the antisymmetric mode. The introduction of the GaN dielectric shows the interesting coupling between the HE_{11} mode and the antisymmetric

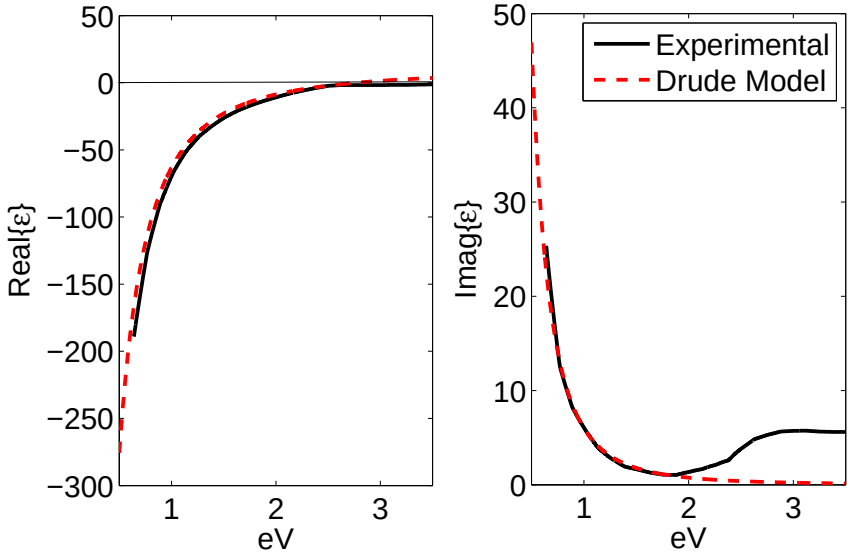

Figure 4.5: Comparison of the Au dielectric function between the Drude model from Eq. (4.1) and experimental results from Ref. [2]. The Drude model follows the experiment for both real and imaginary components below 2 eV.

m=1 mode, where the HE_{11} mode intersects and converges into the antisymmetric m=1 mode. This suggests that the HE_{11} mode transforms into a surface-guided mode traveling along the interface between the core and shell. The interaction enhances the intensity of the hybrid mode, and implies enhanced optical wave-guiding properties.

4.3 Summary

The general surface plasmonic behavior in metallodielectric core-shell nanowires has been explored in the context of EELS. The fast electron is able to detect the splitting of each of the m^{th} order surface plasmon polaritons into its symmetric and anti-symmetric branches. The shell thickness determines the

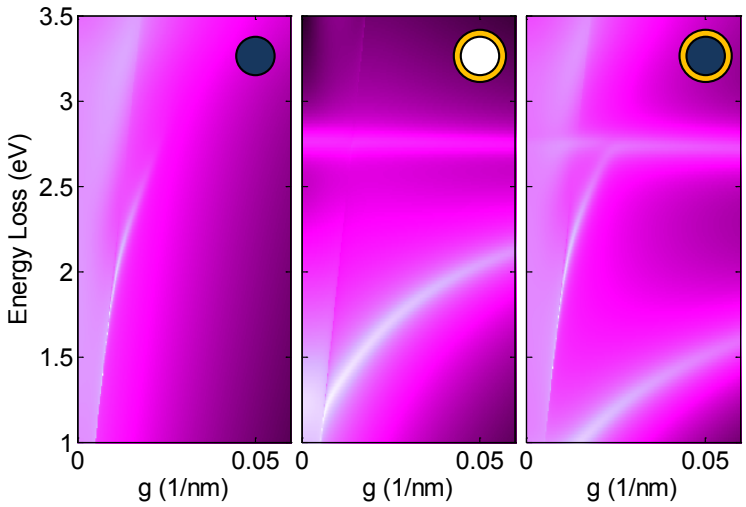

Figure 4.6: Loss-dispersion map for a GaN core, a Drude-model Au shell, and the combined system. Only the m=1 mode is considered for illustration purposes. The core diameter is 160 nm and the outer shell diameter is 170 nm. The impact parameter in all cases is 1 nm away from the outer shell (or 6 nm away from the core). The HE_{11} mode apparent in the isolated GaN core converges to the anti-symmetric mode from the Drude-model Au shell.

splitting energy between each dipolar mode. The thinner shell enhances the coupling between the inner and outer surface charges, and therefore results in a higher splitting of energy. This can be observed in EELS for Au as the symmetric modes are shifted to lower energies.

An introduction of a dielectric core reduces the energies of the symmetric surface plasmon polariton branches. A simple explanation can be provided by considering the origin of surface plasmons. Surface plasmons are a set of collective oscillations of free charges on the metal surface. In order for the oscillations to occur, a restoring force resulting from the charge distribution is necessary. Insertion of a dielectric core modifies the free charges on the surface. This oc-

curs because the dielectric near the surface becomes polarized oppositely to the charges on the metal surface. This offsets the total charge at the interface, and results in an effective reduction in the restoring force and energy. Calculations using GaN and SiO_2 cores have demonstrated this general trend.

Finally, the convergence of the dielectric waveguide modes into the antisymmetric plasmon polariton mode has been predicted in EELS for a GaN core and drude-model Au shell. The HE_{11} mode for a GaN nanowire with no shell would normally damp out at higher momentum. However, with a drude model Au shell, the HE_{11} mode intersects the m=1 antisymmetric plasmon polariton mode, and result in a stronger mode throughout the momentum range.

Such detection of surface plasmonic behavior in metallodielectric core-shell systems with nanometer resolution suggests that STEM/EELS can provide insight unparalleled by any optical technique. In particular, STEM/EELS has the potential to provide in one shot, the entire eigenmodes of the composite system. This ability suggests exciting solutions for the growing field of plasmonic systems.

CHAPTER 5

CONCLUSIONS

5.1 Summary

Here a powerful technique for correlating optical modes to the geometry of nanostructures with nanometer-size resolution has been demonstrated. While the drive for investigating smaller structures requires efficient and simple methods for characterization, the relativistic electron shows clear advantages. Nanoscale optical properties, elusive to conventional optical techniques, were probed with fast electrons for geometries constituting the basic building blocks of more complicated systems. In particular, the WGMs of silica nanospheres, which may have applications in photonic crystals and nanoscale optical resonators were detected. Furthermore, similarities between the photonic bound state and the electronic bound state in quantum mechanics were explored in the context of dielectric spheres. The internal fields inside the excited nanosphere showed the characteristic field distribution similar to those observed in microspheres. The role of retardation in these experiments was essential since the characteristic optical modes cannot be explained in the classical picture. Of the two relativistic loss mechanisms, Cherenkov and transition radiation, transition radiation was found to dominate the loss mechanism in the aloof experiments. Coherent radiation can develop through the formation of a standing wave in the characteristic dimensions of the structure. Calculations showed that this radiation can occur even if the electron travels slower than the speed of light in the material. In short, even when the Cherenkov condition is not met, peaks resulting from transition radiation can form.

Nanowires composed of different materials and sizes were also examined. The aloof electron passing near the surface of a wire oriented perpendicular to the beam was demonstrated to couple to the optical eigenmodes, or the waveguide modes, and result in electron energy losses characteristic to the optical modes. An analytical model using a dielectric theory was constructed and extended from the existing classical treatment into the relativistic framework. The dielectric function and the diameter of the wire are the two key parameters that determine the positions and widths of the peaks, similar to the case for nanospheres. This parameter space was explored for GaN and Ge nanowires. Excellent agreement to the experimental data was obtained for all cases. A multi-mode and zero-mode Ge waveguide could also be distinguished from EELS

The formalism for solid nanowires was extended to core-shell nanowires as the core-shell structure is becoming an increasingly important component in nanoscale optoelectronic devices. Metallodielectric systems were considered for their particular relevance to the growing interest in plasmonics. Again using the relativistic electron, coupling between the core and shell were detected. The effects of different shell thicknesses and dielectric cores were also observed.

In conclusion, the ability to probe optical phenomenon with a nanometer-size probe has been demonstrated. As structures continue to shrink into the nanoscale, the relativistic electron shows a particularly powerful potential for being the method of choice.

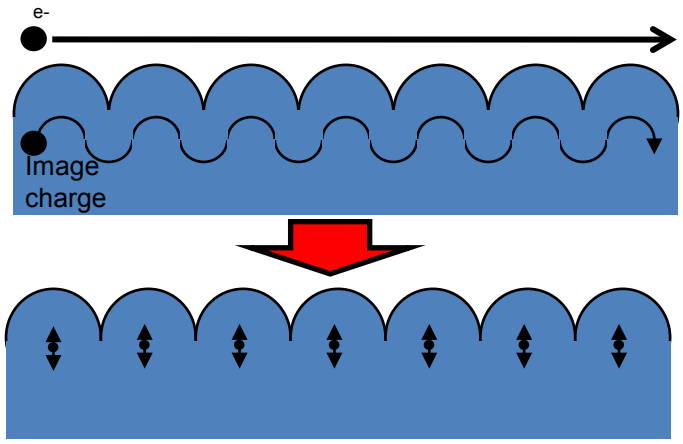

Figure 5.1: A simple illustration that shows the origin of Smith-Purcell radiation. An electron travels near the surface of a photonic crystal. In an attempt to follow the electron, the image charge oscillates according the periodicity of the crystal. The oscillations can be thought of a charge oscillations in the crystal which interact to form a coherent response.

5.2 Future Directions (Smith-Purcell Radiation)

Measuring the photonic structure of various geometries is by no means limited to spheres and nanowires. This section demonstrates some possibilities for probing the photonic modes of more complex systems such as photonic crystals. Photonic crystals can be constructed by assembling a set of nanospheres into an ordered array. The relativistic electron can travel parallel to the surface of the photonic crystals, and in the process probe the photonic band structure. A crude picture of this interaction between electron and crystal can be thought of in terms of the electron inducing an image charge in the crystal (Fig. 5.1).

The image charge will try to keep pace with the electron while maintaining a certain distance away from the electron. Because the surface is structured peri-

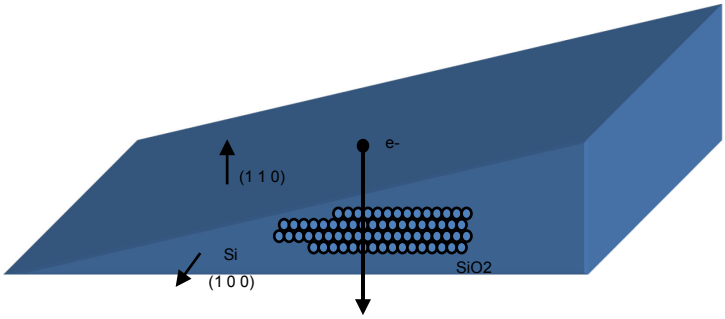

(a)

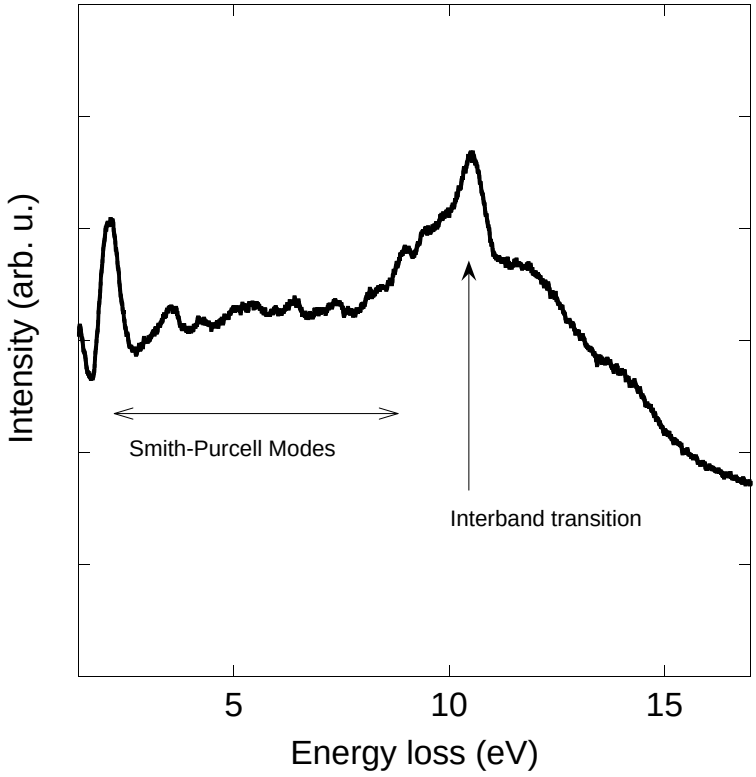

(b)

Figure 5.2: (a) The system used to excite Smith-Purcell radiation. A hexagonal lattice of 280nm-diameter SiO_2 nanospheres were self-assembled onto the (100) surface of a Si wafer. The wafer was then polished from the (100) side into a wedge. The electron passes parallel to the surface of the crystals. (b) The observed EELS spectrum from 200 kV electrons. Below the 10.5 eV interband transition peaks different from the case of a single sphere are apparent.

odically, the image charge will also experience a periodic change in its trajectory. In the small-sphere limit, the oscillation of the image charge can be thought of as a set of individual dipoles. The interaction of these dipoles results in a coherent response called Smith-Purcell radiation [74].

Garcia de Abajo has explored the formalism for the emission of Smith-Purcell radiation in such systems [75]. The basic idea is that the aloof electron can transfer momentum and energy into the photonic bands, thereby providing a signature of the photonic band structure in EELS. This allows the electron to gain access to regions in the band structure that are typically forbidden to external light.

Preliminary data that shows modes representative of Smith-Purcell radiation below the optical gap onset of SiO_2. Silica spheres of 280 nm diameter were self-assembled into a hexagonal lattice onto the (100) surface of a Si wafer. The Si wafer was then polished into a wedge (Fig. 5.2(a)). At the tip of the wedge, the Si diffraction pattern was obtained and used to align the electron optics parallel to the (110) direction. This also ensures that the beam is parallel to the surface of the crystal. Figure 5.2(b) shows an EEL spectrum drastically different from the single sphere case. The interband transition at 10.5 eV can be identified. Below the optical bandgap, a rich set of peaks are resolved. In particular, an intense peak around 2 eV is identified. To understand the origin of the peaks, an in-depth study of the coupling of photonic band-structure to the electron is necessary.

APPENDIX A

INTERNAL FIELD INSIDE A SPHERE INDUCED BY AN EXTERNAL ELECTRON

In order to calculate the internal field induced in a sphere by an external electron beam, one first needs to find the matrix elements for the internal field. One can follow the approach of Garcia de Abajo and express the electromagnetic field in terms of multipoles. Garcia de Abajo conveniently calculates the expansion coefficients for the field of a fast external electron [35]. The fields can be expressed in terms of their transverse magnetic (TM) and transverse electric (TE) components.

$$\begin{aligned} \vec{E} &= \vec{E}^{\mathrm{TM}} + \vec{E}^{\mathrm{TE}} \\ \vec{H} &= \vec{H}^{\mathrm{TM}} + \vec{H}^{\mathrm{TE}} \end{aligned} \tag{A.1}$$

Here, the components can be expressed in terms of scalar functions:

$$\begin{aligned} \vec{E}^{\mathrm{TM}} &= -\frac{i}{k}\vec{\nabla} \times \vec{L}\Psi^{\mathrm{TM}} \\ \vec{E}^{\mathrm{TE}} &= \vec{L}\Psi^{\mathrm{TE}} \\ \vec{H}^{\mathrm{TM}} &= -\vec{L}\Psi^{\mathrm{TM}} \\ \vec{H}^{\mathrm{TE}} &= -\frac{i}{k}\vec{\nabla} \times \vec{L}\Psi^{\mathrm{TE}} \end{aligned} \tag{A.2}$$

where $\vec{L} = -i\vec{r} \times \nabla$ is the orbital angular-momentum operator. The scalar functions for generating the external field is written as

$$\begin{aligned} \Psi^{\mathrm{TE,ext}}(\vec{r}) &= \sum_{l=1} \sum_{m=-1}^{m=1} i^l j_l(kr) Y_{lm}(\Omega_r) \Psi_{lm}^{\mathrm{TE,ext}} \\ \Psi^{\mathrm{TM,ext}}(\vec{r}) &= \sum_{l=1} \sum_{m=-1}^{m=1} i^l j_l(kr) Y_{lm}(\Omega_r) \Psi_{lm}^{\mathrm{TM,ext}}. \end{aligned} \tag{A.3}$$

And for the scattered field,

$$\begin{aligned} \Psi^{\mathrm{TE,sct}}(\vec{r}) &= \sum_{l=1} \sum_{m=-1}^{m=1} i^l h_l^{(+)}(kr) Y_{lm}(\Omega_r) \Psi_{lm}^{\mathrm{TE,sct}} \\ \Psi^{\mathrm{TM,sct}}(\vec{r}) &= \sum_{l=1} \sum_{m=-1}^{m=1} i^l h_l^{(+)}(kr) Y_{lm}(\Omega_r) \Psi_{lm}^{\mathrm{TM,sct}}. \end{aligned} \tag{A.4}$$

where $h_l^{(+)}(x) = ih_l(x)$. For the internal field, it is

$$\begin{aligned}\Psi^{\mathrm{TE,int}}(\vec{r}) &= \sum_{l=1}\sum_{m=-1}^{m=1} i^l j_l(\sqrt{\epsilon}kr)Y_{lm}(\Omega_r)\Psi_{lm}^{\mathrm{TE,int}} \\ \Psi^{\mathrm{TM,int}}(\vec{r}) &= \sum_{l=1}\sum_{m=-1}^{m=1} i^l j_l(\sqrt{\epsilon}kr)Y_{lm}(\Omega_r)\Psi_{lm}^{\mathrm{TM,int}}.\end{aligned} \tag{A.5}$$

This comes from the requirement, $(\nabla^2 + k^2\epsilon)\Psi = 0$ for the field inside the sphere. The internal and scattered scalar fields are related to the external field by

$$\begin{aligned}\Psi^{\mathrm{TE,int}} &= s_l^{\mathrm{TE}}\Psi^{\mathrm{TE,ext}} \\ \Psi^{\mathrm{TM,int}} &= s_l^{\mathrm{TM}}\Psi^{\mathrm{TM,ext}}\end{aligned} \tag{A.6}$$

and

$$\begin{aligned}\Psi^{\mathrm{TE,sct}} &= t_l^{\mathrm{TE}}\Psi^{\mathrm{TE,ext}} \\ \Psi^{\mathrm{TM,sct}} &= t_l^{\mathrm{TM}}\Psi^{\mathrm{TM,ext}},\end{aligned} \tag{A.7}$$

respectively. The coefficients $\Psi^{\mathrm{TE,ext}}$ and $\Psi^{\mathrm{TM,ext}}$ can be found from [35]. Since there is no intermixing between the TM and TE scalar functions for the spherically symmetric system, the scattering matrix and internal-field matrix are both diagonal. This also signifies no m dependence in the matrix elements. To find the matrix elements, one can solve the boundary conditions. The conditions can be simplified to requiring that $\Psi^{\mathrm{TE}}, \epsilon\Psi^{\mathrm{TM}}, \delta\Psi^{\mathrm{TE}}/\delta r$ and $(1 + r\delta/\delta r)\Psi^{\mathrm{TM}}$ be continuous at the surface [35, 76]. The scattering matrix elements were calculated by de Abajo [35]

$$\begin{aligned}t_l^{\mathrm{TM}} &= -i\frac{j_l(\rho_0)[\rho_1 j_l(\rho_1)]' - \epsilon[\rho_0 j_l(\rho_0)]' j_l(\rho_1)}{\epsilon[\rho_0 h_l^{(+)}(\rho_1)]' j_l(\rho_1) - h_l^{(+)}(\rho)[\rho_1 j_l(\rho_1)]'} \\ t_l^{\mathrm{TE}} &= -i\frac{j_l(\rho_0)[\rho_1 j_l(\rho_1)]' - [\rho_0 j_l(\rho_0)]' j_l(\rho_1)}{[\rho_0 h_l^{(+)}(\rho_0)]' j_l(\rho_1) - h_l^{(+)}(\rho_0)[\rho_1 j_l(\rho_1)]'}\end{aligned} \tag{A.8}$$

One can calculate the internal matrix elements in a similar manner.

$$\begin{aligned}s_l^{\mathrm{TM}} &= \frac{\epsilon(j_l(\rho_0)[\rho_0 h_l^{(+)}(\rho_0)]' - h_l^{(+)}(\rho_0)[\rho_0 j_l(\rho_0)]')}{\epsilon[\rho_0 h_l^{(+)}(\rho_1)]' j_l(\rho_1) - h_l^{(+)}(\rho)[\rho_1 j_l(\rho_1)]'} \\ s_l^{\mathrm{TE}} &= \frac{j_l(\rho_0)[\rho_0 h_l^{(+)}(\rho_0)]' - h_l^{(+)}(\rho_0)[\rho_1 j_l(\rho_1)]'}{[\rho_0 h_l^{(+)}(\rho_0)]' j_l(\rho_1) - h_l^{(+)}(\rho_0)[\rho_1 j_l(\rho_1)]'}\end{aligned} \tag{A.9}$$

To find the internal fields, one simply inserts (A.9) into (A.6), then (A.5), and finally (A.2).

APPENDIX B

CYLINDRICAL WAVE EXPANSION OF THE GREEN'S FUNCTION

Solving the relativistic electron energy loss by an infinite dielectric cylinder can be essentially thought of as a light scattering problem. A virtual light source, generated by an electron travelling at a relativistic speed, will scatter off the cylinder and back onto the electron resulting in its energy loss. The problem then boils down to finding the scattered, or induced field, due to the cylinder. This can be treated as any other scattering problem where the external electric field due to the fast electron is first expanded in terms of cylindrical harmonics. The scattered field can then be found by applying the appropriate boundary conditions.

One can start by considering the Green's function for the wave equation. This section employs a small modification to Jackson's discussion of the Green's function for Laplace's equation [12].

$$G(\vec{x}, \vec{x}') = \frac{e^{ik|\vec{x}-\vec{x}'|}}{|\vec{x}-\vec{x}'|} \tag{B.1}$$

which satisfies

$$(\nabla^2 + k^2)G(\vec{x}, \vec{x}') = -4\pi\delta(\vec{x}-\vec{x}').$$

One would want to expand this Green's function in terms of cylindrical waves. This starts by noting

$$(\nabla^2 + k^2)G(\vec{x}, \vec{x}') = -\frac{4\pi}{r}\delta(r-r')\delta(\phi-\phi')\delta(y-y') \tag{B.2}$$

where

$$\delta(y-y') = \frac{1}{2\pi}\int_{-\infty}^{\infty} dg\, e^{ig(y-y')}$$

$$\delta(\phi - \phi') = \frac{1}{2\pi} \sum_{m=-\infty}^{\infty} e^{im(\phi-\phi')}$$

One can expand the Green's function likewise

$$G(\vec{x}, \vec{x}') = \frac{1}{4\pi^2} \sum_m \int_{-\infty}^{\infty} dg\, e^{im(\phi-\phi')} e^{ig(y-y')} g_m(g, r, r'). \tag{B.3}$$

To find g_m one plugs Eq. B.3 into Eq. B.2. One then obtains

$$\frac{1}{r}\frac{d}{dr}\left(r\frac{dg_m}{dr}\right) + \left((k^2 - g^2) - \frac{m^2}{r^2}\right) g_m = -\frac{4\pi}{r}\delta(r - r') \tag{B.4}$$

Letting $u^2 = k^2 - g^2$, the functions that satisfy this for $r \neq r'$ are the Bessel functions.

$$g_m(g, r, r') = A\psi_1(ur_<)\psi_2(ur_>). \tag{B.5}$$

Since $g_m(g, r, r')$ must be finite at $r = 0$ and disappear at $r = \infty$ this leads to

$$\psi_1(ur_<) = J_m(ur)$$

$$\psi_2(ur_>) = H_m^{(1)}(ur')$$

for $r < r'$.

The normalization constant A is determined by the continuity at $r = r'$

$$\left.\frac{dg_m}{dr}\right|_+ - \left.\frac{dg_m}{dr}\right|_- = \frac{4\pi}{r'}$$

where the + and - means evaluated at $r = r' \pm \epsilon$ (The discussion follows from Jackson Section 3.11). This corresponds to

$$A(\psi_1(x)\psi_2'(x) - \psi_1'(x)\psi_2(x)) = -\frac{4\pi}{x}$$

or

$$A(J_m(x)H_m'^{(1)}(x) - J_m'(x)H_m^{(1)}(x)) = -\frac{4\pi}{x}$$

which is equivalent to

$$Ai(J_m(x)Y_m'^{(1)}(x) - J_m'(x)Y_m^{(1)}(x)) = -\frac{4\pi}{x}.$$

Evaluated at $x << 1$ using the asymptotic forms for the Bessel functions, this corresponds to

$$Ai\left(\frac{2}{\pi x}\right) = -\frac{4\pi}{x}.$$

One sees that $A = 2i\pi^2$.

So now from Eq. (B.3) one obtains

$$\frac{e^{ik|\vec{x}-\vec{x}'|}}{|\vec{x}-\vec{x}'|} = \frac{i}{2}\sum_m e^{im(\phi-\phi')}\int_{-\infty}^{\infty} dg\, e^{ig(y-y')}H_m^{(1)}(ur')J_m(ur) \tag{B.6}$$

where $u = \sqrt{k^2 - g^2}$ and $r < r'$. Thus the spherical wave has been expanded into a series of mth order cylindrical harmonics.

APPENDIX C

MATRIX ELEMENTS FOR THE CORE-SHELL CYLINDER

To solve the matrix elements for the core-shell cylinder, the boundary conditions must be satisfied. This requires the tangential components of the electric and magnetic fields at each interface to be continuous, or

$$\begin{aligned}
(\vec{E}^{\text{ext}} + \vec{E}^{\text{sct}} - \vec{E}^{\text{int}})_{r=c} \times \hat{r} = 0 \\
(\vec{H}^{\text{ext}} + \vec{H}^{\text{sct}} - \vec{H}^{\text{int}})_{r=c} \times \hat{r} = 0 \\
(\vec{E}^{\text{c}} - \vec{E}^{\text{a}})_{r=a} \times \hat{r} = 0 \\
(\vec{H}^{\text{c}} - \vec{H}^{\text{a}})_{r=a} \times \hat{r} = 0.
\end{aligned} \tag{C.1}$$

For simplicity, each polarization of the external field is considered one at a time. One first considers the case of an external field with parallel polarization ($\vec{E}^{\text{ext}} = -\frac{i}{k}(\nabla \times \vec{S})\Psi_{\parallel}^{\text{ext}}$ and $\vec{H}^{\text{ext}} = -\vec{S}\Psi_{\parallel}^{\text{ext}}$) . Eq. (C.1) is a set of linear equations, and can be expressed as

$$\vec{A} \cdot \vec{x_{\parallel}} = \vec{b_{\parallel}} \tag{C.2}$$

where $\vec{A}$ is an 8×8 matrix.

$$\vec{A} = \begin{pmatrix}
iuH_m'(uc)\Psi_{gm\perp} & \frac{mg}{kc}H_m(uc)\Psi_{gm\parallel} & -\frac{mg}{\sqrt{\epsilon_c}kc}J_m(u_c c)\Psi_{gm\parallel} & -\frac{mg}{\sqrt{\epsilon_c}kc}Y_m(u_c c)\Psi_{gm\parallel} \\
0 & u^2 H_m(uc) & -\frac{u_c^2}{\sqrt{\epsilon_c}}J_m(u_c c) & -\frac{u_c^2}{\sqrt{\epsilon_c}}Y_m(u_c c) \\
\frac{mg}{kc}H_m(uc)\Psi_{gm\perp} & -iuH_m'(uc)\Psi_{gm\parallel} & i\sqrt{\epsilon_c}u_c J_m'(u_c c)\Psi_{gm\parallel} & i\sqrt{\epsilon_c}u_c Y_m'(u_c c)\Psi_{gm\parallel} \\
u^2 H_m(uc) & 0 & 0 & 0 \\
0 & 0 & \frac{mg}{\sqrt{\epsilon_c}ka}J_m(u_c a)\Psi_{gm\parallel} & \frac{mg}{\sqrt{\epsilon_c}ka}Y_m(u_c a)\Psi_{gm\parallel} \\
0 & 0 & \frac{u_c^2}{\sqrt{\epsilon_c}}J_m(u_c a) & \frac{u_c^2}{\sqrt{\epsilon_c}}Y_m(u_c a) \\
0 & 0 & -i\sqrt{\epsilon_c}u_c J_m'(u_c a)\Psi_{gm\parallel} & -i\sqrt{\epsilon_c}u_c Y_m'(u_c a)\Psi_{gm\parallel} \\
0 & 0 & 0 & 0
\end{pmatrix}$$

$$\begin{pmatrix}
-iu_cJ'_m(u_cc)\Psi_{gm\perp} & -iu_cY'_m(u_cc)\Psi_{gm\perp} & 0 & 0 \\
0 & 0 & 0 & 0 \\
-\frac{mg}{kc}J_m(u_cc)\Psi_{gm\perp} & -\frac{mg}{kc}J_m(u_cc)\Psi_{gm\perp} & 0 & 0 \\
-u_c^2J_m(u_cc) & -u_c^2Y_m(u_cc) & 0 & 0 \\
iu_cJ'_m(u_ca)\Psi_{gm\perp} & iu_cY'_m(u_ca)\Psi_{gm\perp} & -iu_aJ'_m(u_aa)\Psi_{gm\perp} & -\frac{mg}{\sqrt{\epsilon_a}ka}J_m(u_aa)\Psi_{gm\|} \\
0 & 0 & 0 & -\frac{u_a^2}{\sqrt{\epsilon_a}}J_m(u_aa) \\
\frac{mg}{ka}J_m(u_ca)\Psi_{gm\perp} & \frac{mg}{ka}Y_m(u_ca)\Psi_{gm\perp} & -\frac{mg}{ka}J_m(u_aa)\Psi_{gm\perp} & i\sqrt{\epsilon_a}u_aJ'_m(u_aa)\Psi_{gm\|} \\
u_c^2J_m(u_ca) & u_c^2Y_m(u_ca) & -u_a^2J_m(u_aa) & 0
\end{pmatrix} \tag{C.3}$$

$$\vec{x_\|} = [a_{m\|} \quad b_{m\|} \quad c_{m\|} \quad d_{m\|} \quad e_{m\|} \quad f_{m\|}]^{\mathrm{T}} \tag{C.4}$$

and

$$\vec{b_\|} = [-\tfrac{mg}{kc}J_m(uc)\Psi_{gm\|} \quad -u^2J_m(uc) \quad iuJ'_m(uc)\Psi_{gm\|} \quad 0 \quad 0 \quad 0 \quad 0 \quad 0]^{\mathrm{T}}. \tag{C.5}$$

Here $u_a = \sqrt{\epsilon_a k^2 - g^2}$ and $u_c = \sqrt{\epsilon_c k^2 - g^2}$. The scattering matrix elements $a_{m\|}$ and $b_{m\|}$ are the matrix elements relevant to the energy loss probability. These can be found from $\vec{x_\|} = \vec{A}^{-1} \cdot \vec{b_\|}$. One can now consider the case of an external field with perpendicular polarization ($\vec{E}^{\mathrm{ext}} = \vec{S}\Psi_\perp^{\mathrm{ext}}$ and $\vec{H}^{\mathrm{ext}} = -\frac{i}{k}\nabla \times \vec{S}\Psi_\perp^{\mathrm{ext}}$). Again one can construct a set of linear equations that satisfies $\vec{A} \cdot \vec{x_\perp} = \vec{b_\perp}$. The matrix, $\vec{A}$ is found in Eq. (C.3). The vectors $\vec{x_\perp}$ and $\vec{b_\perp}$ are as follows:

$$\vec{x_\perp} = [a_{m\perp} \quad b_{m\perp} \quad c_{m\perp} \quad d_{m\perp} \quad e_{m\perp} \quad f_{m\perp}]^{\mathrm{T}} \tag{C.6}$$

$$\vec{b_\perp} = [-iuJ'_m(uc)\Psi_{gm\perp} \quad 0 \quad -\tfrac{mg}{kc}J_m(uc)\Psi_{gm\perp} \quad \tfrac{u^2}{k}J_m(uc)\Psi_{gm\perp} \quad 0 \quad 0 \quad 0 \quad 0]^{\mathrm{T}}. \tag{C.7}$$

The matrix elements $a_{m\perp}$ and $b_{m\perp}$ are found from solving $\vec{x_\perp} = \vec{A}^{-1} \cdot \vec{b_\perp}$. With some effort the coefficients can be solved analytically, but can also be computed numerically.

BIBLIOGRAPHY

[1] E. Prodan, C. Radloff, N. J. Halas, and P. Nordlander. *Science*, 302:419, 2003.

[2] P. B. Johnson and R. W. Christy. *Phys. Rev. B*, 6:4370, 1972.

[3] J. D. Joannopoulos, S.G. Johnson, J.N. Winn, and R.D. Meade. *Photonic crystals: modling the flow of light*. Princeton University Press, Princeton and Oxford, 2nd edition, 2008.

[4] F. Iacona, G. Franzo, and C. Spinella. *J. Appl. Phys.*, 87:1295, 2000.

[5] B. Tian1, X. Zheng, T. J. Kempa, Y. Fang, N. Yu, G. Yu, J. Huang, and C. M. Lieber. *Nature*, 449:885, 2007.

[6] M. D. Kelzenberg, D. B. Turner-Evans, B. M. Kayes, M. A. Filler, M. C. Putnam, N. S. Lewis, and H. A. Atwater. *Nano Lett.*, 8:710, 2008.

[7] Z. Fan, J. C. Ho, Z. A. Jacobson, H. Razavi, and A. Javey. *P. Natl. Acad. Sci. USA*, 105:11066, 2008.

[8] X. Duan, Y. Huang, R. Agarwal, and C. M. Lieber. *Nature*, 421:241, 2003.

[9] J. C. Johnson, H.-J. Choi, K. P. Knutsen, R. D. Schaller, P. Yang, and R. J. Saykally. *Nat. Mater.*, 1:106, 2002.

[10] F. Znhausern, Y. Martin, and H. K. Wickramasinghe. *Science*, 269:1083–1085, 1995.

[11] E. M. Purcell. *Electricity and Magnetism*. McGraw-Hill, 2nd edition, 1985.

[12] J. D. Jackson. *Classical Electrodynamics*. Wiley, New York, 3rd edition, 1998.

[13] N. Bohr. *Philos. Mag.*, 25:10, 1913.

[14] A. Yurtsever, M. Weyland, and D. A. Muller. *Appl. Phys. Lett.*, 89(15):151920, 2006.

[15] Z. L. Wang. *Micron*, 27(3–4):265–299, 1996.

[16] F. Ouyang, P. E. Batson, and M. Isaacson. Quantum size effects in the surface-plasmon excitation of small metallic particles by electron-energy-loss spectroscopy. *Phys. Rev. B*, 46(23):15421–15425, Dec 1992.

[17] P. E. Batson. *Phys. Rev. Lett.*, 49:936, 1982.

[18] R. H. Ritchie and H. B. Eldridge. *Bull. Am. Phys. Soc.*, 4:384, 1959.

[19] A. Otto. *Phys. Status Solidi*, 22:401, 1967.

[20] R. Vincent and J. Silcox. Dispersion of radiative surface plasmons in aluminum films by electron scattering. *Phys. Rev. Lett.*, 31(25):1487–1490, Dec 1973.

[21] C. H. Chen and J. Silcox. Detection of optical surface guided modes in thin graphite films by high-energy electron scattering. *Phys. Rev. Lett.*, 35(6):390–393, Aug 1975.

[22] E. Kroger. *Z. Phys.*, 216:115, 1968.

[23] R. Garcia-Molina, A. Gras-Martit, A. Howie, and R. H. Ritchie. *J. Phys. C Solid State*, 18:5335, 1985.

[24] A. Yurtsever, M. Couillard, and D. A. Muller. *Phy. Rev. Lett.*, 100:217402, 2008.

[25] F. J. García de Abajo, A. G. Pattantyus-Abraham, N. Zabala, A. Rivacoba, M. O. Wolf, and P. M. Echenique. Cherenkov effect as a probe of photonic nanostructures. *Phys. Rev. Lett.*, 91(14):143902, Sep 2003.

[26] F. J. García de Abajo and M. Kociak. Probing the photonic local density of states with electron energy loss spectroscopy. *Physical Review Letters*, 100(10):106804, 2008.

[27] M. Couillard, A. Yurtsever, and D. A. Muller. *Phys. Rev. B*, 77:085318, 2008.

[28] G. Mie. *Ann. Phys.*, 330:377, 1908.

[29] K. J. Vahala. *Nature*, 424:839, 2003.

[30] V. S. Ilchenko and A. B. Matsko. *IEEE J. Sel. Top. Quantum Electron*, 12:15, 2006.

[31] A. Libchaber M. Khoshsima I. Teraoka F. Vollmer, D. Braun and S. Arnold. *Appl. Phys. Lett.*, 80:4057, 2002.

[32] W. Zakowicz. *Phys. Rev. Lett.*, 95:114801, 2005.

[33] R. Fuchs and K. L. Kliewer. *J. Opt. Soc. Am.*, 58:319, 1968.

[34] H. Mabuchi E. W. Streed D. W. Vernooy, V. S. Ilchenko and H. J. Kimble. *Opt. Lett.*, 23:247–249, 1998.

[35] F. J. García de Abajo. Relativistic energy loss and induced photon emission in the interaction of a dielectric sphere with an external electron beam. *Phys. Rev. B*, 59(4):3095–3107, Jan 1999.

[36] K. Inoue and K. Ohtaka. *Photonic Crystals: Physics, Fabrication, and Applications*. 2004.

[37] E.D. Palik. *Handbook of Optical Constants*. Academic, Orlando, 1998.

[38] F. J. García de Abajo. Multiple scattering of radiation in clusters of dielectrics. *Phys. Rev. B*, 60(8):6086–6102, Aug 1999.

[39] T. L. Ferrell, R. J. Warmack, V. E. Anderson, and P. M. Echenique. Analytical calculation of stopping power for isolated small spheres. *Phys. Rev. B*, 35(14):7365–7371, May 1987.

[40] K. Ohtaka and M. Inoue. Light scattering from macroscopic spherical bodies. i. integrated density of states of transverse electromagnetic fields. *Phys. Rev. B*, 25(2):677–688, Jan 1982.

[41] R. Agarwal and C. M. Lieber. *Appl. Phys. A*, 85:209, 2006.

[42] R. Agarwal, C. J. Barrelet, and C. M. Lieber. *Nano. Lett.*, 5:917, 2005.

[43] J. Li and N. Engheta. *IEEE T. Antenn. Propag.*, 55:3018, 2007.

[44] G. F. Bertsch, H. Esbensen, and B. W. Reed. Electron energy-loss spectrum of nanowires. *Phys. Rev. B*, 58(20):14031–14035, Nov 1998.

[45] N. Zabala, E. Ogando, A. Rivacoba, and F. J. García de Abajo. Inelastic scattering of fast electrons in nanowires: A dielectric formalism approach. *Phys. Rev. B*, 64(20):205410, Oct 2001.

[46] D. Taverna, M. Kociak, V. Charbois, and L. Henrard. Electron energy-loss spectrum of an electron passing near a locally anisotropic nanotube. *Phys. Rev. B*, 66(23):235419, Dec 2002.

[47] J. P. R. Bolton and M. Chen. *J. Phys.: Condens. Matter*, 7:3389, 1995.

[48] C. A. Walsh. *Philos. Mag. A*, 59:227, 1989.

[49] N. Zabala, A. Rivacoba, and P.M. Echenique. *Surf. Sci.*, 209:465, 1989.

[50] J. K. Hyun, M. Couillard, P. Rajendran, C. M. Liddell, and D. A. Muller. Measuring far-ultraviolet whispering gallery modes with high energy electrons. *Applied Physics Letters*, 93(24):243106, 2008.

[51] F. J. García de Abajo and A. Howie. Relativistic electron energy loss and electron-induced photon emission in inhomogeneous dielectrics. *Phys. Rev. Lett.*, 80(23):5180–5183, Jun 1998.

[52] F. J. García de Abajo and A. Howie. Retarded field calculation of electron energy loss in inhomogeneous dielectrics. *Phys. Rev. B*, 65(11):115418, Mar 2002.

[53] Shuji Nakamura, Masayuki Senoh, and Takashi Mukai. High-power ingan/gan double-heterostructure violet light emitting diodes. *Applied Physics Letters*, 62(19):2390–2392, 1993.

[54] H. Morkoç, S. Strite, G. B. Gao, M. E. Lin, B. Sverdlov, and M. Burns. Large-band-gap sic, iii-v nitride, and ii-vi znse-based semiconductor device technologies. *Journal of Applied Physics*, 76(3):1363–1398, 1994.

[55] Silvija Gradečak, Fang Qian, Yat Li, Hong-Gyu Park, and Charles M. Lieber. Gan nanowire lasers with low lasing thresholds. *Applied Physics Letters*, 87(17):173111, 2005.

[56] Aleksandra B. Djurišić and E. Herbert Li. Dielectric function models for describing the optical properties of hexagonal gan. *Journal of Applied Physics*, 89(1):273–282, 2001.

[57] Stephen D. Hersee, Xinyu Sun, and Xin Wang. The controlled growth of gan nanowires. *Nano Letters*, 6(8):1808–1811, 2006.

[58] Steven Johnson and John Joannopoulos. Block-iterative frequency-domain methods for maxwell's equations in a planewave basis. *Opt. Express*, 8(3):173–190, 2001.

[59] Louis Bauer and Edward L. Reiss. Cutoff wavenumbers and modes of hexagonal waveguides. *SIAM Journal on Applied Mathematics*, 35(3):508–514, 1978.

[60] A. V. Maslov and C. Z. Ning. Reflection of guided modes in a semiconductor nanowire laser. *Applied Physics Letters*, 83(6):1237–1239, 2003.

[61] D. A. Muller and J. Silcox. Delocalization in inelastic-scattering. *Ultramicroscopy*, 59:195, 1995.

[62] J. H. Woodruff, J. B. Ratchford, I. A. Goldthorpe, P. C. McIntyre, and C. E. D. Chidsey. *Nano Lett.*, 7:1637, 2007.

[63] H. R. Philipp and E. A. Taft. *Phys. Rev.*, 113:1002, 1959.

[64] Brendan M. Kayes, Harry A. Atwater, and Nathan S. Lewis. Comparison of the device physics principles of planar and radial p-n junction nanorod solar cells. *Journal of Applied Physics*, 97(11):114302, 2005.

[65] C. Graf and A. van Blaaderen. *Langmuir*, 18:524, 2002.

[66] M. Brongersma. *Nat. Mater.*, 2:296, 2003.

[67] J. J. Penninkhof, L. A. Sweatlock, A. Moroz, H. A. Atwater, A. van Blaaderen, and A. Polman. *J. Appl. Phys.*, 103:123105, 2008.

[68] Eloïse Devaux, Alain Dereux, Eric Bourillot, Jean-Claude Weeber, Yvon Lacroute, Jean-Pierre Goudonnet, and Christian Girard. Local detection of the optical magnetic field in the near zone of dielectric samples. *Phys. Rev. B*, 62(15):10504–10514, Oct 2000.

[69] Ursula Schröter and Alain Dereux. Surface plasmon polaritons on metal cylinders with dielectric core. *Phys. Rev. B*, 64(12):125420, Sep 2001.

[70] S.A. Maier. Effective mode volume of nanoscale plasmon cavities. *Optical and Quantum Electronics*, 38:257–267, 2006.

[71] Hideki T. Miyazaki and Yoichi Kurokawa. Squeezing visible light waves into a 3-nm-thick and 55-nm-long plasmon cavity. *Physical Review Letters*, 96(9):097401, 2006.

[72] M. T. Hill, Y.-S. Oei, B. Smalbrugge, Y. Zhu, T. de Vries, P. J. van Veldhoven, F. W. M. van Otten, T. J. Eijkemans, J. P. Turkiewicz, H. de Waardt, E. J. Geluk, S.-H. Kwon, Y.-H. Lee, R. Notzel, and M. K. Smit. *Nat. Photon.*, 1:589, 2007.

[73] E. Prodan, A. Lee, and P. Nordlander. *Chem. Phys. Lett*, 360:325, 2002.

[74] S.J. Smith and E.M. Purcell. *Phys. Rev.*, 92:1069, 1953.

[75] F. J. García de Abajo and L. A. Blanco. Electron energy loss and induced photon emission in photonic crystals. *Phys. Rev. B*, 67(12):125108, Mar 2003.

[76] F. E. Low. *Classical Field Theory: Electromagnetism and Gravitation*. Wiley, New York, 1997.